A theoretical study of transition metal surfaces and interfaces using semi-quantitative models
by Chong In Hong

A thesis submitted in partial fulfillment of the requirements for the degree of Doctor of Philosophy in Chemistry
Montana State University

Abstract:
Electron emission due to deexcitation of metastable noble-gas atoms occurs at transition metal surfaces through resonance ionization of the metastable atom and subsequent Auger neutralization. The resulting electron energy distribution contains information on the local surface density of states and is approximated by a self-convolution function.

A semi-quantitative theoretical model was modified to compute the spectrum of ejected Auger electrons observed in ion neutralization spectroscopy (INS) from a magnetized, Ni (110) sample, which was bombarded by an excited noble gas ion. The rate of ion neutralization was calculated along a classical trajectory for a helium ion impinging on the metal surface. The Auger matrix elements for the neutralization process were calculated for a screened Coulomb potential between the atomic wavefunctions of the metal atoms and those of the incident ion.,A parametric model for the metal surface density of states (SDOS) was fitted to the experimentally observed electron emission spectra, allowing a semi-quantitative analysis of the surface electronic and magnetic properties, including the relative intensities of the 3- d and 4-sp bands, the minority and majority d-band splitting, the polarization asymmetry of the magnetized nickel (110), and the dilution effect for the asymmetry by the 4- sp electrons.

The semi-quantitative model was extended to calculate the spectrum of ejected electrons observed in INS from a bimetallic sample consisting of a thin Cu film on a Ru (0001) substrate. The metal SDOS was extracted by maximizing the fit of the computed to the experimentally observed electron emission spectra. Semi-quantitative analysis of the electronic properties (i.e, SDOS including relative intensities of the d-bands and sp-bands) of both the clean Ru and the Cu/Ru bimetallic interface was obtained. The change in the SDOS and hence the electronic properties of the bimetallic interface as a function of copper film thickness was revealed. The real Cu coverages on Ru were calculated by a non-linear method.

Precursor-mediated molecular chemisorption and thermal desorption of N2 on Ru(001) was modeled semi-quantitatively by using kinetic schemes. Thermal desorption with a variation of temperature and adsorption coefficient as a function of surface coverage for the N2/Ru(001) system were examined. A calculational method was proposed for the entropy change of an adlayer and the Arrhenius prefactor. A Physical interpretation of the binding energy, the entropy of the N2 adlayer and the Arrhenius prefactor as a function of surface coverage were given.

A THEORETICAL STUDY OF TRANSITION METAL SURFACES AND INTERFACES USING SEMI-QUANTITATIVE MODELS

By

Chong In Hong

A thesis submitted in partial fulfillment
of the requirements for the degree

of

Doctor of Philosophy

in

Chemistry

MONTANA STATE UNIVERSITY
Bozeman, Montana

November 1991

APPROVAL

of a thesis submitted by

Chong In Hong

This thesis has been read by each member of the thesis committee and has been found to be satisfactory regarding content, English usage, format, citations, bibliographic style, and consistency, and is ready for submission to the College of Graduate Studies.

11/25/1991
Date

Reed Howald
Chairperson, Graduate Committee

Approved for the Major Department

11/25/91
Date

John R Crusa
Head, Major Department

Approved for the College of Graduate Studies

11/27/91
Date

Henry L Parsons
Graduate Dean

STATEMENT OF PERMISSION TO USE

In presenting this thesis in partial fulfillment of the requirements for a doctoral degree at Montana State University, I agree that the Library shall make it available to borrowers under rules of the Library. I further agree that copying of this thesis is allowable only for scholarly purposes, consistent with "fair use" as prescribed in the U. S. Copyright Law. Requests for extensive copying or reproduction of this thesis should be referred to University Microfilms International, 300 North Zeeb Road, Ann Arbor, Michigan 48106, to whom I have granted "the exclusive right to reproduce and distribute copies of the dissertation in and from microfilm and the right to reproduce and distribute by abstract in any format."

Signature Nov. 25, 1991

Date

TABLE OF CONTENTS

TABLES OF CONTENTS -- Continued

LIST OF TABLES

LIST OF FIGURES

LIST OF FIGURES -- Continued

LIST OF FIGURES -- Continued

LIST OF FIGURES -- Continued

ABSTRACT

Electron emission due to deexcitation of metastable noble-gas atoms occurs at transition metal surfaces through resonance ionization of the metastable atom and subsequent Auger neutralization. The resulting electron energy distribution contains information on the local surface density of states and is approximated by a self-convolution function.

A semi-quantitative theoretical model was modified to compute the spectrum of ejected Auger electrons observed in ion neutralization spectroscopy (INS) from a magnetized, Ni(110) sample, which was bombarded by an excited noble gas ion. The rate of ion neutralization was calculated along a classical trajectory for a helium ion impinging on the metal surface. The Auger matrix elements for the neutralization process were calculated for a screened Coulomb potential between the atomic wavefunctions of the metal atoms and those of the incident ion. A parametric model for the metal surface density of states (SDOS) was fitted to the experimentally observed electron emission spectra, allowing a semi-quantitative analysis of the surface electronic and magnetic properties, including the relative intensities of the 3-d and 4-sp bands, the minority and majority d-band splitting, the polarization asymmetry of the magnetized nickel(110), and the dilution effect for the asymmetry by the 4-sp electrons.

The semi-quantitative model was extended to calculate the spectrum of ejected electrons observed in INS from a bimetallic sample consisting of a thin Cu film on a Ru(0001) substrate. The metal SDOS was extracted by maximizing the fit of the computed to the experimentally observed electron emission spectra. Semi-quantitative analysis of the electronic properties (i.e, SDOS including relative intensities of the d-bands and sp-bands) of both the clean Ru and the Cu/Ru bimetallic interface was obtained. The change in the SDOS and hence the electronic properties of the bimetallic interface as a function of copper film thickness was revealed. The real Cu coverages on Ru were calculated by a non-linear method.

Precursor-mediated molecular chemisorption and thermal desorption of N_2 on Ru(001) was modeled semi-quantitatively by using kinetic schemes. Thermal desorption with a variation of temperature and adsorption coefficient as a function of surface coverage for the N_2/Ru(001) system were examined. A calculational method was proposed for the entropy change of an adlayer and the Arrhenius prefactor. A Physical interpretation of the binding energy, the entropy of the N_2 adlayer and the Arrhenius prefactor as a function of surface coverage were given.

SPIN-POLARIZED ION NEUTRALIZATION SPECTROSCOPY (SPINS) ON THE MAGNETIC NI (110) SYSTEM

Background and Introduction

Interpretation of Ion Neutralization Spectra

Ion neutralization spectroscopy (INS) is one of the methods by which information on the electronic structure at a metal-vacuum interface can be obtained [1~3]. Traditionally the surface is bombarded by a beam of ions (usually He^+, Ne^+) in the energy range of 4~100 eV. When the ions are neutralized by an Auger process, electrons are ejected from the surface with an energy distribution characteristic of the system (ion/surface) under consideration. INS is the measurement and analysis of this energy distribution. More recently a variation of this spectroscopy, called metastable quenching spectroscopy (MQS) has been developed [3~5] which employs ions of very low energy (0.05eV). The very low energy ions are produced by resonance ionization of metastable atoms in a thermal beam of ground and excited states (2^1S and 2^3S He^*) incident on the surface.

The process of neutralization by an Auger transition, which follows the creation of the ion, is considered to be a resonant tunneling process [1].

An exact quantitative analysis of IN spectra involves the evaluation of initial and final electronic wavefunctions in a two-electron transition and the evaluation of the matrix

element between them with an appropriately screened Coulomb interaction [6]. The analysis is made easier if we assume constant matrix elements. In this case the energy distribution of the emitted Auger electrons is given by an integral fold (self-convolution) of the density of states over the occupied part of the conduction band of the metal. The difference between the calculated (bulk) density of states and the effective density of states, obtained by a deconvolution procedure from the IN spectrum is partly attributable to the difference in the local density of states at the surface and the bulk of the material, but other factors which enter into the determination of the matrix element may be significant [6].

It is generally known that at clean and atomic adsorbate-covered transition metal surfaces deexcitation occurs by resonance ionization (RI) followed by Auger neutralization (AN), whereas Auger deexcitation often dominates [1~3] at surfaces covered with molecular adsorbates. The non-radiative decay of electronically excited states at a metal surface may proceed through RI or AN or via Auger deexcitation (AD). The work function ϕ of transition and noble metal surfaces is generally in the 4~6 eV range, and between the Fermi and vacuum levels a continuous density of unoccupied electronic states exists. Since the ionization energy of the metastable noble-gas atoms (X^*) is in the 4 eV range, resonance ionization by transfers of the excited electrons

into unoccupied metal states is highly probable. Electron emission occurs by subsequent Auger neutralization of the ion X^+ formed at the surface. RI is a competing process to AD, which dominates (RI or AD) depends on the respective transition rates.

Magnetic Properties of Materials

If a substance is placed in a magnetic field H, the density of lines of force in the sample, known as the magnetic induction B, is $B = H + 4\pi I$, where I is the magnetic moment of the sample per unit volume. The permeability p is defined as

$$p = B/H = (H + 4\pi I)/H = 1 + 4\pi I/H = 1 + 4\pi k.$$

The susceptibility k of a magnetic substance is $k = I/H$ and the molar susceptibility x is kF/d, where F is the formula weight and d is the density of the sample. The different kinds of magnetic behavior may be distinguished by the values of p, k, x, and their temperature and field dependencies.

For example...

diamagnetic substances : $p<1$, k and x are small and slightly negative.

paramagnetic substances : $p>1$, k and x are positive.

ferromagnetic substances : $p>1$, large k and x values.

antiferromagnetic substances : $p>1$, k and x are positive. The values of k and x are comparable to those for paramagnetic substances, but have a different temperature dependence. Thus ferromagnetic substances are more strongly attracted by a magnetic field than paramagnetic substances, whereas

diamagnetic substances experience a slight repulsion.

The susceptibilities of the different kinds of magnetic materials are distinguished by their different temperature dependencies and by their absolute magnitudes [7]. The Curie law can be defined as molar susceptibility, x, given by $x = C/T$, where C is the Curie constant and T is the temperature. However, a better fit to the experimental data is provided by the Curie-Weiss law, as $x = C/T + \Theta$, where Θ is the Weiss constant. For ferro- and antiferromagnetic substances, the temperature dependence of x does not fit the simple Curie/Curie-Weiss laws. Ferromagnetic materials show a very large susceptibility at a low temperature that decreases rapidly as the temperature rises. Above a certain temperature (the ferromagnetic Curie temperature), the material is no longer ferromagnetic but reverts to paramagnetic behavior, where Curie-Weiss law behavior is usually observed.

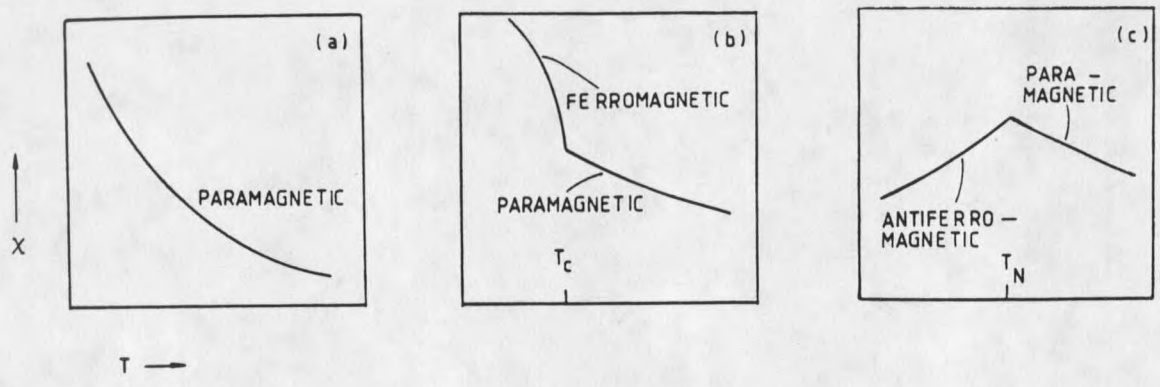

Figure 1. Temperature dependencies of the magnetic susceptibility [7] for (a) paramagnetic (b) ferromagnetic and (c) anti-ferromagnetic materials. T_N is the Neel point.

Introduction to Surface Magnetism

Many studies of the magnetism and related electronic properties of 3d magnetic transition metal surfaces and interfaces have been developed by means of surface methods over the past few years [8~26]. These properties are determined by the local band structure which is directly based on the surface spin density of states, since the carriers of magnetic moment are itinerant d electrons. Thus, one of the fundamental problems of surface magnetism is to determine the ground-state surface perturbation to the magnetization density. For this purpose several calculational schemes have been developed including the linearised augmented plane-wave method (LAPW) [15, 17], the self-consistent local orbital (SCLO) technique [23], and tight-binding calculations [24].

We demonstrate a simple, semi-quantitative method using ion neutralization spectroscopy (INS), for surveying the surface electronic properties including the spin density of states and the magnitude of exchange splitting, and the surface magnetic properties including the polarization asymmetry, A, and the dilution effect A_{dil} for the asymmetry of the Ni(110) surface. The INS technique is highly surface specific and is a versatile tool [1, 2, 6] for probing the surface vacuum interface. It has recently been improved by using incident thermal beams of He (2^3S) metastable atoms incident on a metal surface [3, 4, 25].

Recent experimental studies of surface magnetism have

analyzed the spin dependencies of Auger electron yields resulting from the de-excitation of electron-spin-polarized metastable helium [25, 26] Their initial investigations performed on a clean, but unmagnetized Ni(110) sample revealed a dependence of the secondary electron yield on the metastable atom polarization. G. K. Walters group [4] illustrated that if the metastable atom beam is polarized, the resultant spin dependencies in the secondary-electron yields contain information regarding the ferromagnetic properties of Ni(110) surfaces. As an electron-spin-polarized He(2^3S) atom proceeds to a Ni(110) surface, it will be resonantly ionized and deexcited at the magnetized surface. Because the electron spins are polarized, the neutralization to the ground state of the atom will be determined by the electron spin orientation of the helium ion, i.e., if the electron in the ion is spin-down, only a spin-up conduction electron can neutralize the ion, or vice versa. The energy released by Auger neutralization is transferred to the second conduction electron which may be excited and escape the substrate. The kinetic energy distribution of the ejected electrons represents the local surface density of occupied electronic states.

Since the electron spin which will neutralize the ion is not directly related with that of the ejected electron, either spin-up or spin-down electrons may escape the surface, and their escaping intensities will be monitored separately,

according to their spin orientation. A measure of the difference of the two spin intensities is known as experimental asymmetry parameter A [4, 12], which is given by the following equation:

$$A = \frac{1}{|P_z|} \frac{R_+ - R_-}{R_+ + R_-} \qquad \text{eq. 1-(1)}$$

where P_z is beam polarization, and R_+ and R_- are the Channeltron count rates for beam polarization of P_z and $-P_z$, respectively. For $He(2^3S)$, which is polarized in the z direction, it is necessary to specify two polarization parameters [12], which are components of the Cartesian polarization tensor and are described as

$$p_z = \frac{n_+ - n_-}{n_+ + n_o + n_-} \qquad \text{eq. 1-(2)}$$

$$p_{zz} = \frac{(n_+ + n_-) - 2n_o}{n_+ + n_o + n_-} \qquad \text{eq. 1-(3)}$$

where n_+, n_o, n_- are the numbers of atoms in the $m_j(m_s)=1$, 0, -1 sublevels, respectively, in the beam. The normalization condition for the sublevels, combined with the specified P_z and P_{zz} values is used to determine the relative populations in the three magnetic sublevels. For the Ni sample n_+ was 0.6, n_o was 0.12, and n_- was 0.28.

We developed a theoretical model to estimate the spectrum of the ejected Auger electrons observed in the INS from a magnetized Ni(110) sample. The rate of ion neutralization was

calculated along a classical trajectory for a helium metastable atom impinging on a metal surface. The Auger matrix elements for the neutralization process were calculated for a screened Coulomb potential between the atomic wavefunctions of the metal and those of the incident ion.

Computational Scheme

General Dynamics of the Auger System

The Auger transition system can be described by the schematic energy diagram in Figure 2. In the initial system, the helium atom is far enough from the metal surface so that there is no interaction between the two systems, which we reference as the zero energy state of the system. As a final state of the system, the noble gas ion is neutralized and the Auger electron is emitted from the surface.

As the thermal beam of $He(2^3S)$ metastable atoms approaches the Ni(110) surface from a relatively distant point (~ 8Å), the wave functions of the electron in the incident particle begin to overlap with those of the energy band of the Ni surface. In this process the excited electron in the metastable atom, which lies at a higher energy level than the Fermi level of the metal, may be transferred to the metal's unoccupied energy levels by resonant quantum tunneling. This places a positive charge on the helium atom, making it a positive ion. Because the impinging ion is now charged, an

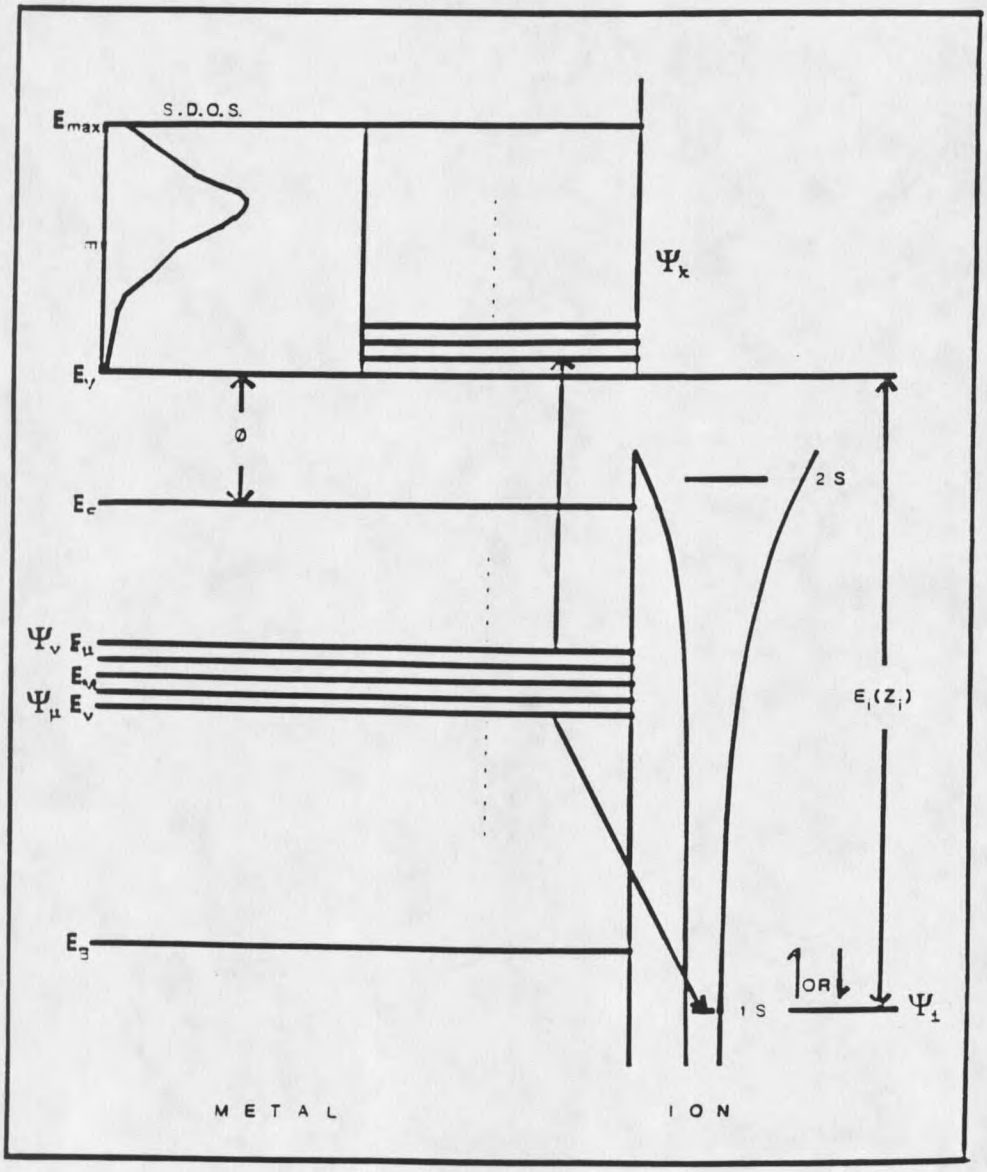

Figure 2. Schematic energy diagram for He^* with Ni(110) surface. ε_v denotes the vacuum level, ε_f the Fermi level, ε_B the bottom of conduction band, $\varepsilon_{\mu,M,\nu}$ any arbitrary occupied electron energy level, $E(k)_{max}$ the maximum kinetic energy of ejected electrons, and ϕ the metal's work function. The arrows indicate the electronic transition. Ψ_i represents the orbital for the ground state energy of the gas, and Ψ_μ and Ψ_ν mean the orbitals for the energy band of the metal, and Ψ_k is the metallic orbital extended into the vacuum. The inset represents the surface density of states, deconvoluted from the resultant kinetic energy distribution of Auger electrons.

image potential will be created on the metal side through the entire electronic screening process. The image force is given [27] by

$$F = \xi^2 \left(\frac{1 - \epsilon_r}{1 + \epsilon_r}\right) \frac{1.153 \cdot 10^{-35}}{z^2} \ (dynes) \qquad \text{eq. 1-(4)}$$

where ε_r is the dielectric constant of the metal, ξ is the charge of the ion and z is the ion distance in Å. The image potential will contribute to the ionization potential of the He atom in some degree (~4.0 eV), and will be the driving force for Auger electronic interaction.

As the incident particle comes closer to the surface, a conduction electron may start to neutralize the ion by filling the vacant ground state energy level of the ion (the 1S orbital). The amount of energy released by an electron which neutralized the ion will be eventually delivered to another electron in the band so that the second electron will be excited to the vacuum level. Some of those excited electrons which have enough energy to overcome the surface energy barrier may escape the surface.

The energy conservation condition is met in the form of the equation $\varepsilon_\mu + \varepsilon_v = E(k) + E_i(Z_i)$ because the energy of the incoming particle is usually adiabatic through the Auger electronic transition. Any electron in the band with suitable spin orientation for the helium ion's electron may neutralize the ion. Maintaining energy conservation, the amount of neutralization energy $\varepsilon_\mu - E_i(Z_i)$ will vary according to the

original level in the band for Auger neutralization. Energy of this magnitude will be given to the second electron, so that a relationship is set: $E(k) - \varepsilon_v = \varepsilon_\mu - E_i(z_i)$. There should be numerous energy levels available to reach a particular energy level in the vacuum from the levels of the conduction band. Rearranging the above equation shows that the kinetic energy of the free Auger electron depends on only the sum of ε_μ and ε_v (which is denoted as α). This means that now if the level ε_μ for the neutralization is specified, the energy level ε_v for the excitation to the vacuum will be readily determined at constant $E(k)$ in the vacuum.

If we denote the density of states of the electron at ε_μ as $\rho(\varepsilon_\mu)$ and of the electron at ε_v as $\rho(\varepsilon_v)$, the total number of energy states, corresponding to different ε_μ and ε_v and keeping the same α is given as

$$\rho_{tot,\alpha}(\epsilon) = \int_{\epsilon_{elbe}}^{\epsilon_F} \int_{\epsilon_{elbe}}^{\epsilon_F} \rho(\epsilon_\mu)\ \rho(E_v)\ \delta(\epsilon_\mu + \epsilon_v - \alpha)\ d\epsilon_\mu\, d\epsilon_v \qquad \text{eq.1-(5)}$$

Thus, the number of Auger electrons with the energy level $E(k)$ will be proportional to $\rho_{tot,\alpha}(\varepsilon)$ and the deconvolution of the measured IN spectra will give information about $\rho(\varepsilon_\mu)$ and $\rho(\varepsilon_v)$ in the band. The density of states will be represented as a set of Gaussian functions or other distribution functions.

Trajectory of the Incident Helium Ion

When the helium metastable proceeds to the metal surface, the potential energy of the helium ion with the surface

follows the Lennard-Jones potential. After the ion is neutralized the potential curve will not change appreciably with the distance of the gas/surface system, due to the fact that the neutralized system is energetically stable.

The helium ions are simulated to accelerate continuously normal to the metal surface from the initial speed 1.1×10^5 cm/sec and then are neutralized up to 95% at 1.1Å from the surface at a time lapse of 2.5×10^{-14} to 6.0×10^{-13} sec. The neutralization process is maximized about 3.0~3.5Å from the surface, as shown in Figure 3 and depends upon the speed of the helium atom. For example, if the speed of helium is increased to 4.1x10e5 cm/sec, the rate will be maximized around 1.0~1.5Å.

Probability of Auger Electron Generation

The total probability for a transition from the state | i> to any one of the group | s> may be written as, according to first order time dependent perturbation theory [28],

$$P_{all|s>}(t) = \sum_s P_{s_i}(t) = \sum_s |C_s(t)>^2 \qquad \text{eq. 1-(6)}$$

where

$$C_s(t) = c_s(t)\, e^{-(i/\hbar)E_s^{(0)}t} \qquad \text{eq. 1-(7)}$$

where $c_s(t)$ is a slowly varying function of time. If the states |s> are continuously distributed we must replace the sum by an integral, taking into account how many states | s>

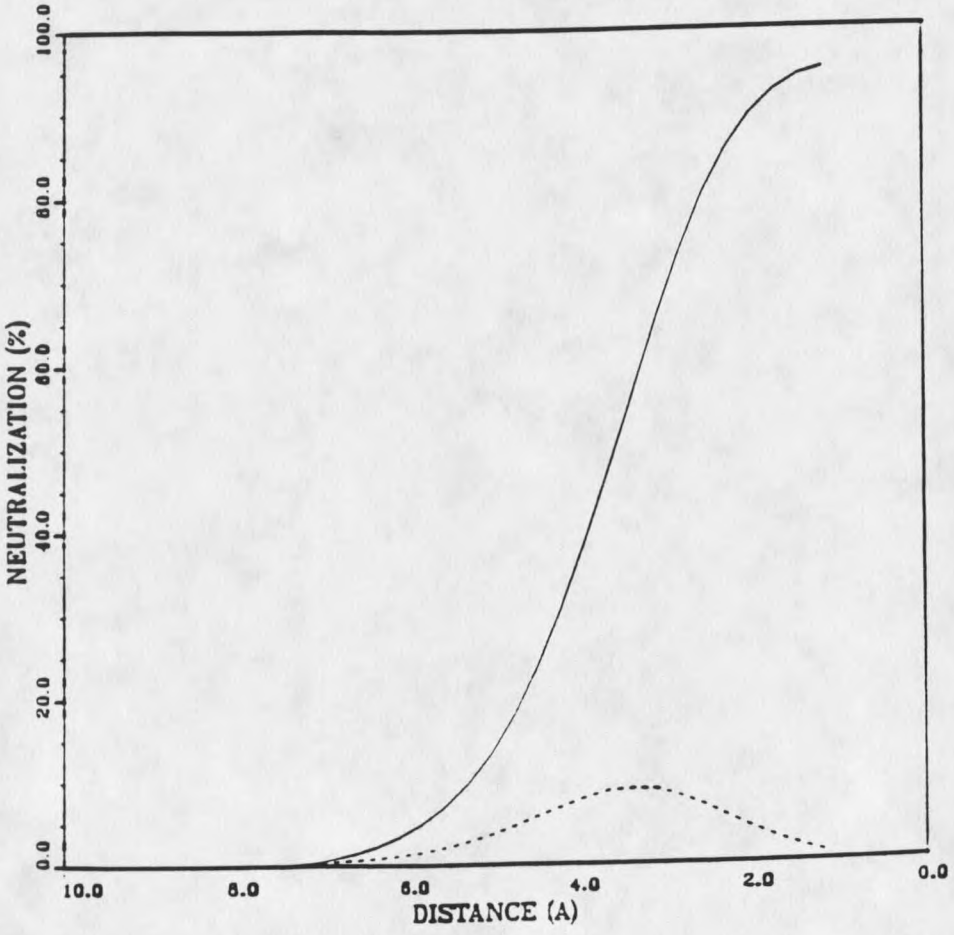

Figure 3. Percentage of neutralized helium as a function of ion-solid distance. The percentage is represented as the solid line and the rate of neutralization as a dotted line.

are found per unit energy interval in the vicinity of the energy $E_s^{(0)}$. Thus the total transition probability can be expressed as

$$P_{all|s>} = \int |c_s(t)| \rho(E_s)\, dE \qquad \text{eq. 1-(8)}$$

Therefore the probability for a transition per unit time is given as

$$R_{s_i}(t) = P_{all|s>}(t) = \frac{2\pi}{h} \overline{|(H_1)_{s_i}|^2}\, \rho(E_s) \qquad \text{eq. 1-(9)}$$

where H_1 is a time-independent perturbation and the conversion factor $\rho(E_s)$ is the density of final states.

By replacing the density of final states $\rho(E_s)$ in eq. 1-(9) as $\rho(\varepsilon_\mu)\rho(\varepsilon_v)\rho(E(k))$, holding energy conservation in the system, and integrating eq. 1-(9) over the entire range of ε_μ and ε_v, the rate of production of Auger electrons with the energy corresponding to a particular energy E(k) can be written as

$$W_k(\alpha) = \frac{2\pi}{h} \int\int |H(\epsilon_k, \epsilon_\mu, \epsilon_v; z(\alpha)|^2 \rho(\epsilon_\mu)$$

$$\rho(\epsilon_v)\, \rho(E(k))\, \delta(I_\alpha - \epsilon_\mu - \epsilon_v - \epsilon_k)\, \delta(\alpha - \epsilon_\mu - \epsilon_v)\, d\epsilon_\mu\, d\epsilon_v \qquad \text{eq. 1-(10)}$$

where $Z(\alpha)$ is the position where the ion is neutralized, and $H(\varepsilon_k, \varepsilon_\mu, \varepsilon_v; Z(\alpha))$ is the matrix element of any two electrons involved in Auger neutralization and excitation, respectively. For the rate of production of electrons for all possible energies E(k), we need to integrate eq. 1-(10) over the range of E(k) as

$$W(\alpha) = \int W_k(\alpha)\, d\varepsilon_k \qquad \text{eq. 1-(11)}$$

As the helium ion approaches the metal along the classical trajectory z=z(t), it might pass through many crossing points Z(α), corresponding to other possible values of α. If we define the survival probability p(Z(t)) as the probability function that the incident particles starting from an infinite distance toward the metal will reach the distance Z(t) without undergoing transition, the probability $P_k(t)$ that an electron with kinetic energy E(k) is produced at the position Z(α) = Z(t) is given [1, 6] by $P_o(z, v_o)$ multiplied by the survival probability as,

$$P_k(t) = p(Z(t))\, P_0(z,v_0)\, W_k(\alpha(t)) \qquad \text{eq. 1-(12)}$$

where $P_o(z, v_o)$, the probability that the excited electron escapes into the vacuum, is given by the semi-empirical formula [1, 6]. Because the derivative of the survival probability with respect to time is proportional to the survival probability function and proportional to the decrease of the rate of excited electron generation, the survival probability is defined by the following rate equation.

$$\frac{dp\ (Z(t))}{dt} = -\ W(\alpha(t))\ p(Z(t)) \qquad \text{eq. 1-(13)}$$

If we can provide a model for the matrix element $H(\varepsilon_k, \varepsilon_\mu, \varepsilon_\nu ; Z(\alpha))$, we should be able to calculate W(α), which will be used to compute the survival probability and we can evaluate the probability function $P_k(t)$ with the known

$P_o(z, v_o)$. By integrating the probability over time for the ion trajectory which is a function of time and distance, we derive the following expression.

$$S_k(t) = \sum_i P_k(t_i) \qquad \text{eq. 1-(14)}$$

Thus we obtain another probability function $S_k(t)$ which represents the IN spectrum which is produced by computation. This computed spectrum is compared to the experimental one and the difference between these two spectra will be iteratively minimized to produce the best density of states possible from the selected number of normal Gaussian distribution functions.

Matrix Element of the Auger Process

In the transition elements the d-bands are only partly filled, and have a high density of states and a short spatial extent. These bands overlap with the next higher s-bands, which have relatively low density of states and extend further into the vacuum. To abide by the facts that the shape of the IN spectra is dependent upon both the density of states and the size of the orbitals forming the energy bands, we may envision two distances, Z_d and Z_{sp} ($Z_{sp} > Z_d$), correspondingly to the distances at which the electrons in the band d or sp, respectively neutralize the vacant site in the incident ion most efficiently.

As the ion approaches the surface it will first reach Z_{sp} and Auger neutralization occurs by electron transfer from the sp-band to the ion and electron ejection from either the sp or

the d-band. We denote these processes as sp-sp and d-sp, respectively. If the ion survives to reach Z_d, it can be Auger neutralized by electron transfer from the d-band to the ion, and electron ejection from either the d or sp bands (denoted as processes d-d and sp-d). We estimate the Auger matrix elements for these 4 different situations, because a quantitative evaluation of the Auger matrix elements is very complicated, due to the fact that the electronic wave functions of the surface coexist with those of helium neutral or ion.

The matrix element describing the Auger process is

$$H(\epsilon_k , \epsilon_\mu : z(d)) = \int\int \psi_i^*(r_2)\ \psi_k^*(r_1)\ W(|r_2 - r_1|)\ \psi_\nu(r_1)\ \psi_\mu(r_2)\ dr_1 dr_2 \qquad \text{eq.1-(15)}$$

where $W(|r_1 - r_2|)$ is a screened Coulomb interaction between two surface electrons, taken to be in the Yugawa form [29] as,

$$W(|r_2 - r_1|) = \exp\left(\frac{-\lambda |r_2 - r_1|}{|r_2 - r_1|}\right) \qquad \text{eq. 1-(16)}$$

The calculation of the matrix elements has been derived elsewhere [6] and the result is as

$$-H(\epsilon_k , \epsilon_\mu , \epsilon_\nu : z) = \frac{(2\pi)^2\ C_i\ C_k\ C_\nu\ C_\mu}{\lambda(\alpha_\nu - \lambda)\ \beta(\beta - \alpha_\mu - \lambda)} *$$

$$\exp[-\beta(z - \delta) - (\alpha_\mu + \lambda)] * [(z + \delta) + (\beta - \alpha_\mu - \lambda)^{-1} + \beta^{-1}]$$

$$- \exp[-(\alpha_\mu + \lambda)z] * [(\beta - \alpha_\mu - \lambda)^{-1} + \beta^{-1}]] \qquad \text{eq. 1-(17)}$$

where C_i is the normalization factor for the atomic

wavefunctions of the ion, and C_ν and C_μ are those of the conduction electrons and C_k is that of emitted electrons, and β is the exponential decay parameter of the ion, and α_μ and α_ν are the exponential decay parameters of metallic wavefunctions, and δ is the distance cut-off parameter required to keep the Coulomb interaction finite. As shown in Figure 4, the matrix elements are mainly influenced by the sp-sp and the d-d Auger processes.

Probability of Escape of an Excited Electron

The probability $P(\varepsilon_k)$ for an excited electron of energy ε_k to escape from a metal surface is given [1, 2] as

$$P(\varepsilon_k) = \int_0^{2\pi} \int_0^{\Theta_c} P(\Theta, \varepsilon_k) \sin\Theta \, d\Theta \, d\phi \qquad \text{eq. 1-(18)}$$

where $\Theta_c(\varepsilon_k)$ is the maximum value of Θ for which escape over the surface barrier possible. $P(\Theta, \varepsilon_k)\, d\Omega$ is the probability that the excited electron of energy ε_k has its velocity vector lying in $d\Omega$ ($= \sin\Theta \, d\Theta \, d\phi$) at the polar angles Θ and ϕ. Here ε_k measures the energy of the ejected Auger electron relative to the vacuum. If we assume that the angular distribution of electrons is isotropic, then $P(\Theta, \varepsilon_k)$ is constant as

$$P(\Theta, \varepsilon) = \frac{1}{4\pi} \qquad \text{eq. 1-(19)}$$

Substitution of eq. 1-(19) into eq. 1-(18) gives the following.

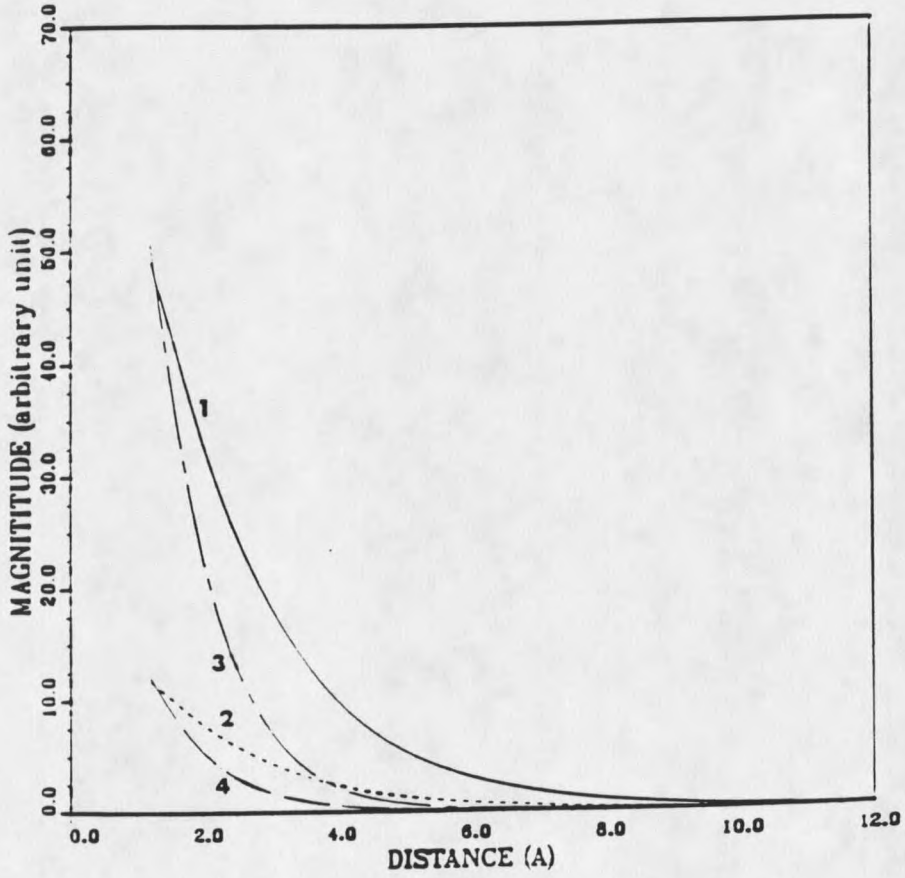

Figure 4. Magnitude of the matrix elements of the 4 different types of normalized processes. The magnitude of the sp-sp process is 52.1 (line 1), that of sp-d is 12.4 (line 2), that of d-d is 28.6 (line 3), and that of d-sp process is 6.9 (line 4).

$$P(\epsilon_k) = (1 - \frac{\epsilon_0}{\epsilon_k - \epsilon_0})\ (1/2) \qquad if > 0$$

$$= 0 \qquad if < 0 \qquad \text{eq. 1-(20)}$$

where ϵ_o is the energy of the bottom of the conduction band with respect to the vacuum. Calculations of the total electron yield using eq. 1-(20) for $P(\epsilon_k)$ give results significantly below those experimentally determined. This discrepancy between the calculated and experimentally determined yield suggests that $P(\Theta, \epsilon_k)$ is not an isotropic function. To model the anisotropy in the Auger ejection pattern, the following semi-empirical expression for the electronic escape probability was developed by Hagstom[1] as

$$P(\epsilon_k) = \frac{1}{2} \frac{1 - [\frac{\epsilon_o}{\epsilon_o + \epsilon_k}]^{1/2}}{\{1 - [1 - (\frac{1}{f^2})][\frac{\epsilon_o}{\epsilon_o + \epsilon_k}]^{1/2}\}} > 0.0 \qquad \text{eq. 1-(21)}$$

$$= 0 \qquad < 0.0$$

The numerical value of the parameter f can be determined by fitting the calculated total Auger electron yield to experimental measurements.

Numerical Studies of He^* on Ni(110)

Screening by Conduction Electron

The symmetric solution of Poisson's equation [30], corresponding to a charge at the origin, and combined with the

Thomas-Fermi equation is of the form,

$$\Phi(r) = \frac{e^2}{r} \exp(-\frac{r}{\lambda}) \qquad \text{eq: 1-(22)}$$

where the potential function Φ (r) is an additional electric potential generated within the crystal by the charge deviation. Eq. 1-(22) is for a screened Coulomb potential, which falls off exponentially with distance with a certain screening length λ. The main consequence of screening is to transform a long range Coulomb potential into a screened Coulomb function. The fact that the crystal is a metal subject to screening results in a sharply decaying potential rather than a gradually decaying Coulomb potential. Then, if the screening length is short, the electrons cannot respond ideally because of their finite wavelength even at the top of the Fermi distribution. For normal metal crystals, the screening length is quite short, like only a few angstroms or less. The decay parameter λ in the Thomas-Fermi potential was 0.25(1/Å) in our calculations.

Gaussian Distribution and its Usage for Density of States

Because one of the disadvantages of the "simple, forward" model [1] was the foreknowledge of the general form of the metallic surface density of states (which is not easy to obtain), the metallic density of states is modelled parametrically, in our computation, by a linear combination of displaced, multiple Gaussian functions of variable position, amplitude, and half-width. We can show that the normal

approximation satisfies the requirement for a probability function, which is that its integral from $-\infty$ to ∞ must be 1. Also if a random variable x has the normal approximation as its probability density function, then the standard deviation of x is given by

$$f(x) = C(n,x)\, P^x\, Q^{n-x} \quad \frac{1}{\sqrt{2\pi npq}}\, e(-\frac{(x-np)^2}{2npq}) \qquad \text{eq. 1-(23)}$$

Combining eq. 1-(23) with Stirling's formula, we get

$$\frac{1}{\sigma\sqrt{2\pi}} \exp(-\frac{(x-\mu)^2}{2\sigma^2}) \qquad \text{eq. 1-(24)}$$

as a normal density function for a random variable. This is the Gaussian form used in our calculations.

Decay Parameters of the Atomic Wavefunctions of the Metal and Helium

The metallic wavefunctions of 3d electrons, which decay exponentially into the continuum states are taken to be

$$\Phi_{3d}(r) = A \exp^{(-\xi_{3d}r)} \qquad \text{eq. 1-(25)}$$

The decay parameter ξ_{3d} can be calculated from the information on the 3d radial distribution function [31]. The same consideration is given to the decay parameters of the 4sp orbitals of nickel and the helium atom orbital. The values computed are 0.93 1/Å for the 3d electron decay parameter, 0.35 1/Å for that of the 4sp electrons as shown in Figure 5, and 3.78 1/Å for the helium orbitals.

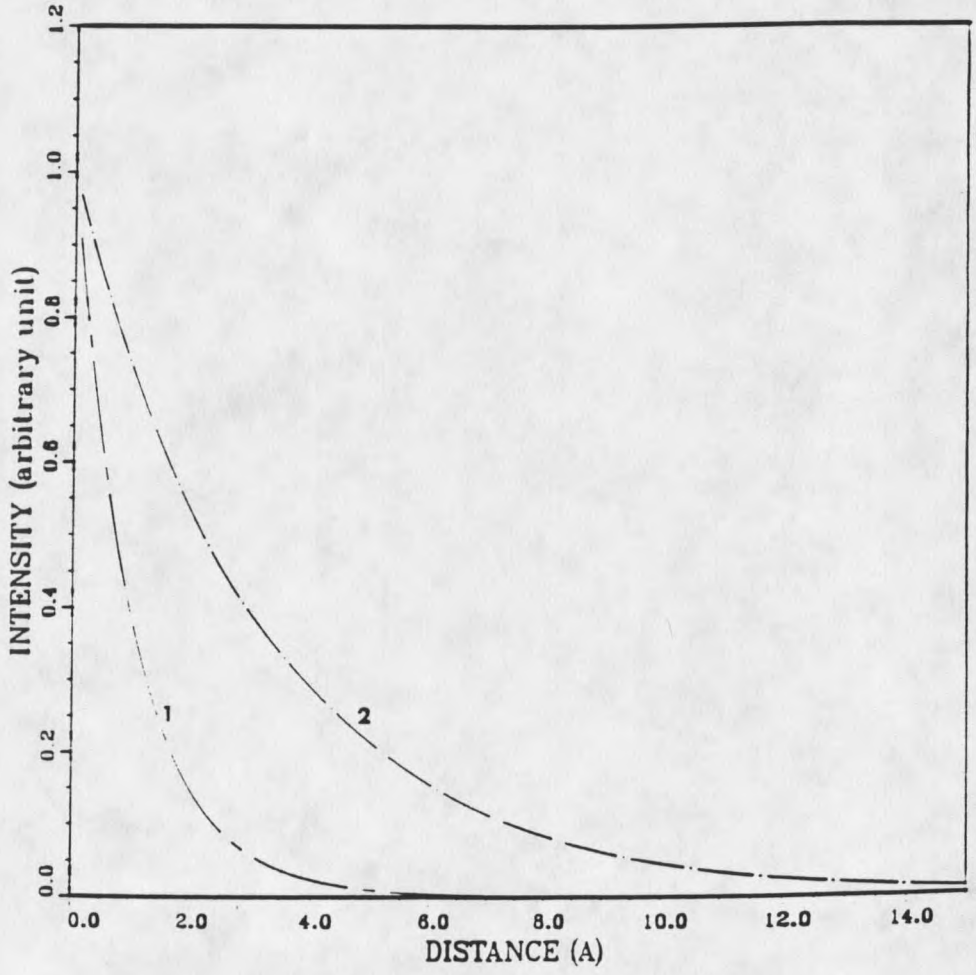

Figure 5. Plot of the metallic wavefunction decay parameters. The 3-d band decay with distance is represented as line 1 and the 4-sp band decay with distance is represented as line 2.

Results and Discussion

Comparison of IN Spectrum with One D-band DOS Parameter Versus That with Two D-band DOS Parameters

Whether or not a nickel sample is magnetized, a lowering of the energy occurs for those electrons with spin orientation parallel to the magnetic field (if the sample is placed under the influence of external fields) as compared with those with spin orientation antiparallel to the field. Thus a 4-d energy band will be split into two different bands. This energy difference results in a transfer of some electrons from unfavorable to favorable states so that the Fermi level of the two bands is equalized. This process gives a net magnetic moment from the resultant electron-spin distribution. A transfer of electrons from one half band to the other must involve a net increase in the kinetic energy of the valence electrons, and a corresponding decrease in spin alignment energy must emerge when the transfer occurs spontaneously. The source of this energy decrease will be a form of the exchange interaction between neighboring 3d shells.

From the viewpoint of the energy balance, we need to look into the nature of the metal's 3d-band. The 3d electrons are more localized than those of the s and p bands [32], and the relative narrowness of the 3d-band will influence the fact that the Fermi kinetic energy is small and the density of states at the Fermi level is relatively large. Thus a large number of electrons can be transferred from one to the other band with a small overall increase in kinetic energy.

A calculation with one d-band DOS (density of states) parameter and two sp-band DOS parameters was made, according to the previous computational scheme, by iteratively fitting the computer-generated spectra to the experimental one, which is shown in Figure 6. As a consequence of this computed spectrum, the surface density of states of Ni appears in Table 1 and Figure 7. The d-band DOS is highly localized, and most of the 3d-band is occupied states, and the 3d-band width is 4.5 eV. However, the 4sp-band is delocalized over a wider range of energy. The ratio of magnitude of 3d-band versus 4sp-band is 7 to 1. Note that there is a low population of SDOS at the Fermi level.

Another calculation was made by using two 3d-band DOS parameters (one of the 3d-band represents the majority d-band and the other represents the minority band) and two sp-band DOS parameters. The IN spectrum is shown in Figure 8 and the surface density of states of the magnetized Ni appears in Table 1 and Figure 9. The relative magnitude of d and sp-bands with one d and two sp-band DOS turns out to be same as that with two d and two sp DOS. In Figure 9, the two 3d-bands are highly localized and part of the minority band is shifted above the Fermi level, and the majority band is almost fully occupied. The exchange splitting between the majority and minority band is 1.3 eV, which is slightly larger than that of Zhu and et. al.'s report [23]. The ratio of the magnitude of

Table 1. The surface density of states of unmagnetized and magnetized Ni(110) sample.

(a) Characteristic parameters of the Gaussian functions optimized in surface density of states of unmagnetized Ni surface.

Gaussian function Label: i	Amplitude A	Width (in eV)	Mean position** (in eV)
1	33.16	0.72	-1.74
2	2.99	0.13	-2.32
3	4.31	10.11	-11.50

(b) Characteristic parameters of the Gaussian functions optimized in surface density of states of magnetized Ni surface

Gaussian function Label: i	Amplitude A	Width (in eV)	Mean position (in eV)
1	20.22	0.83	-0.85
2	20.22	0.83	-2.15
3	6.21	0.13	-2.07
4	4.60	6.95	-12.00

* The surface density of states $\rho(\varepsilon)$ is described by a linear combination of multiple Gaussians

$$\rho(\varepsilon) = \Sigma \frac{A_i}{\sigma_i (2\pi)^{1/2}} \exp\left[\frac{-(\varepsilon - \mu_i)}{2\sigma_i^2}\right]$$

** The mean position is measured relative to the Fermi level.

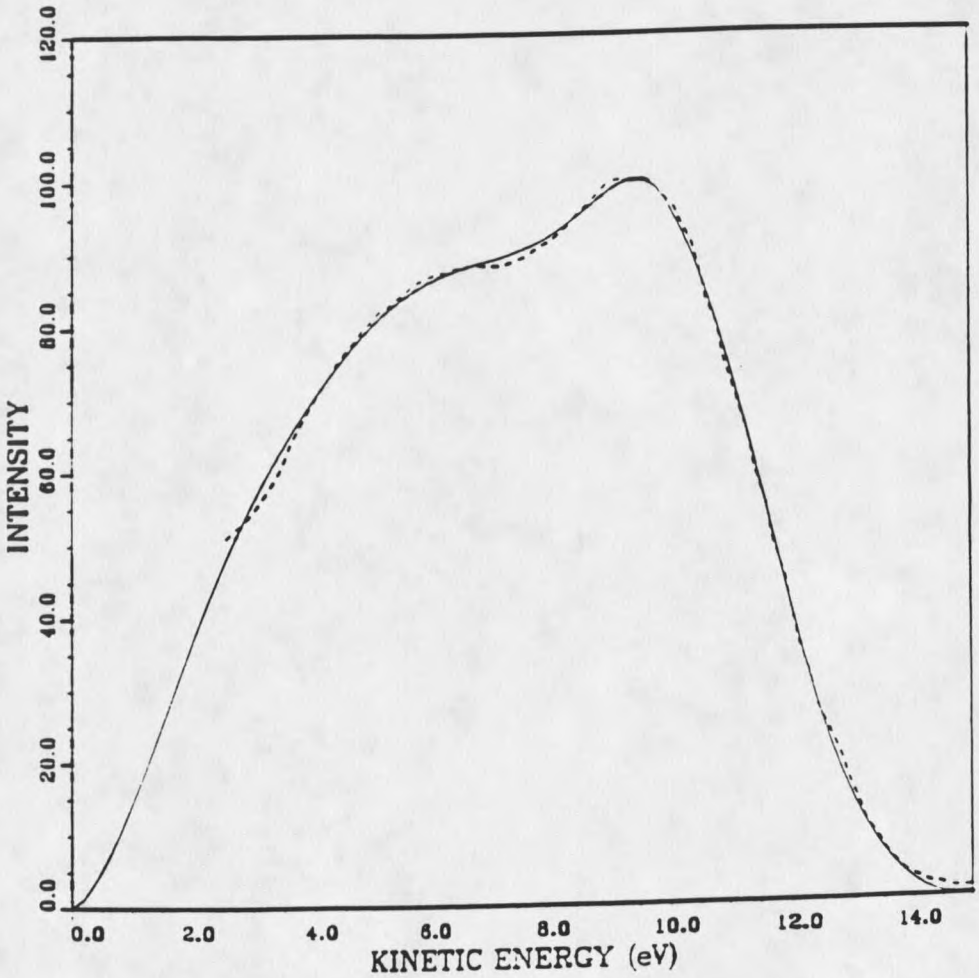

Figure 6. Computer-generated spectrum (solid line) with the experimental one (dotted line). One d-band DOS parameter and two sp-band parameters are used.

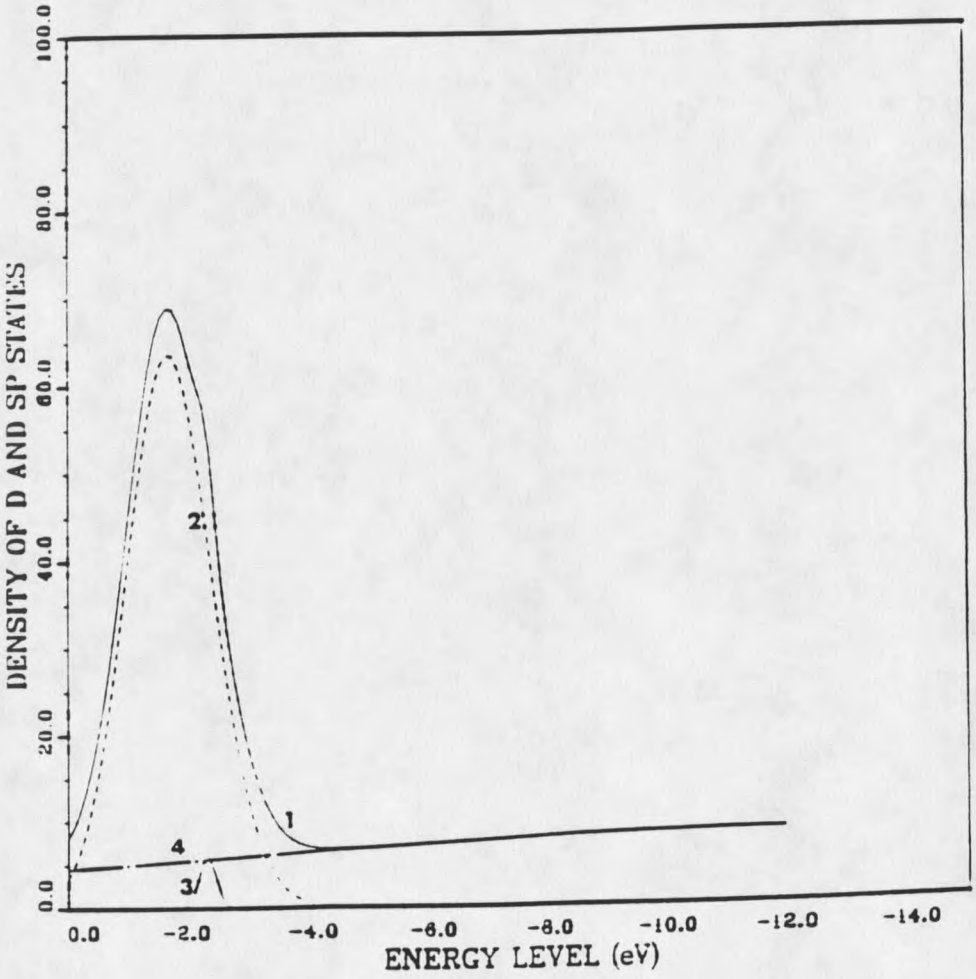

Figure 7. Surface density of states based on the calculated, kinetic energy distribution of ejected Auger electrons. The magnitude of the normalized surface density of states of the d-band is 57.22 (line 2) and that of first sp-band is 0.98 (line 3), and that of second sp-band is 41.79 (line 4). The total DOS is shown along line 1.

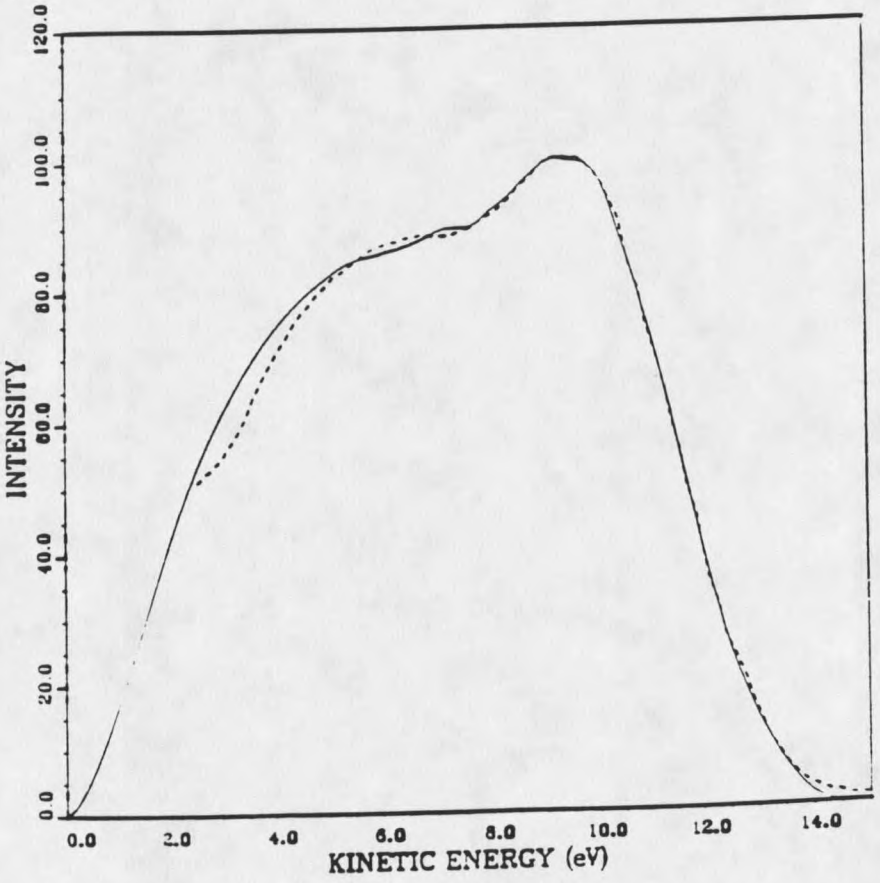

Figure 8. Computer-generated spectrum (solid line) with the experimental one (dotted line) for a magnetized Ni(110) sample. Two d-band DOS parameters are used.

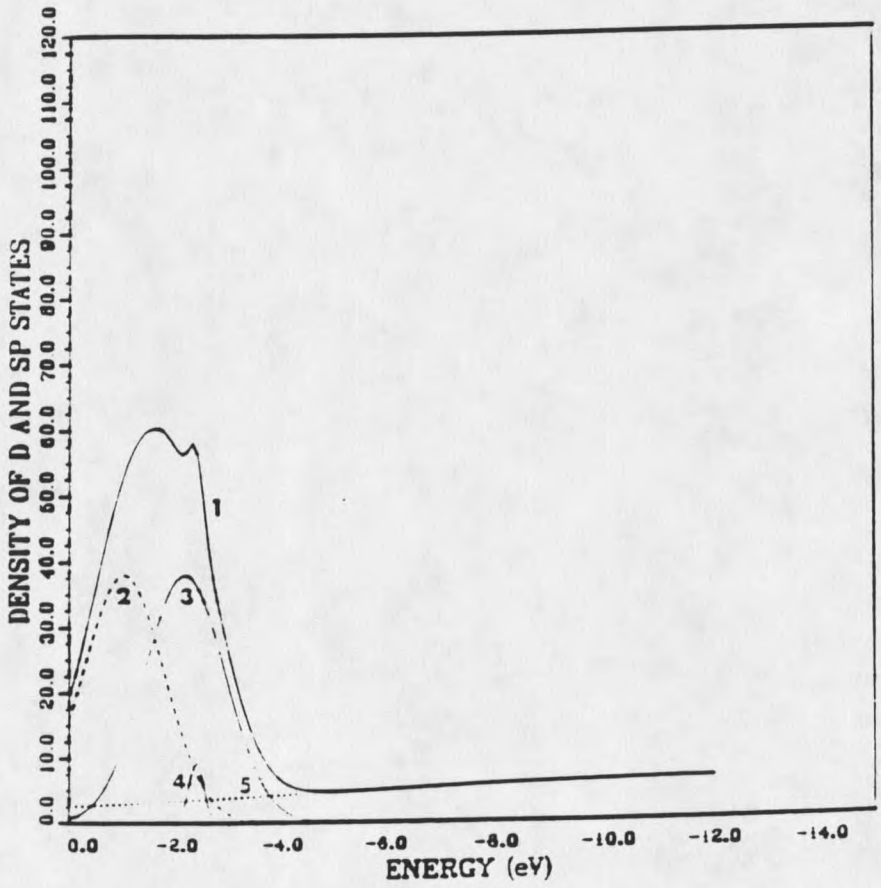

Figure 9. Surface density of states based on the calculated, kinetic energy distribution of Auger electrons of the magnetized Ni(110) sample. The magnitude of the normalized surface density of states (sdos) of the d-minor band is 32.90 (line 2), that of the d-major band is 36.16 (line 3), that of first sp-band is 1.62 (line 4), and that of second sp-band is 29.32 (line 5). The total normalized sdos is shown along line 1.

the unoccupied minority to the occupied minority band is 18%. This result is in good agreement with that of Zhu and et al.'s work, and is larger than the value for bulk, which is calculated from the experimentally determined value of saturation magnetization (μ = 0.604) [7(b)].

Polarization Asymmetry

Polarization asymmetry is experimentally known [33,34] and represented by eq. 1-(1). From Figure 10, we have calculated the asymmetry parameter, based on the computer-generated IN spectra which is the best fit to the experimental one. For the emitted spin-up electron in the majority band, we have to consider two different situations of Auger neutralization. Because the spin state of electrons which neutralize the incoming ions does not influence the spin state of electrons which will be excited, but affects only the spin state of the electron of the incident ion, we can construct a calculational scheme which is demonstrated in Figure 10. Because sp electrons are less atomic in character than d electrons, they are more spin-insensitive. There is a spin-matching requirement in both part of the IN process. For example, in Figure 10-(a), the number 1 refers to the minority d band which is spin-down. Thus an emitted electron with spin up cannot come from this band, and we put a number of x's in this column of part (a) in Figure 10. Similarly the number 2 refers to the majority d band (spin up) and the Pauli exclusion principle prevents one of these electrons

neutralizing the incident ion if it has a spin up electron in the ground state orbital. Part (a) in Figure 10 is for the ion with a spin up electron, so we have a number of x's in the second row in part (a) in Figure 10. The numbers 3 and 4 are for sp bands which are spin-insensitive, so there are no x's in the bottom right part of each diagram.

We continue to apply the same reasoning for $e_j(e)(\uparrow)$ and neut($\downarrow$) system, and build another scheme as in Figure 10-(b). Part (b) is for the ion with a spin down electron. For the minority d-band DOS, we again apply the same method and obtain the other two arrays which are parts (c) and (d) in Figure 10. They correspond to the ion with the spin up electron and spin down electron, respectively.

For an example for calculating the intensities of the ejected spin-up electrons in the majority d-band, we need to modify eq. 1-(12) by facilitating only terms which have two circles in each compartment in Figures 10-(a) and (b) and by ruling out any terms which have any cross mark, because they are not pertinent for considering the spin-up electron intensities.

To estimate the intensities of the ejected spin-down electrons from the minority d-band, we exclude, by using the same reasoning, any terms which have a cross mark. The intensities of the ejected spin-up electrons correspond to the value of R_+ and those of the ejected spin-down electrons correspond to the value of the R_- in eq. 1-(1). The result of

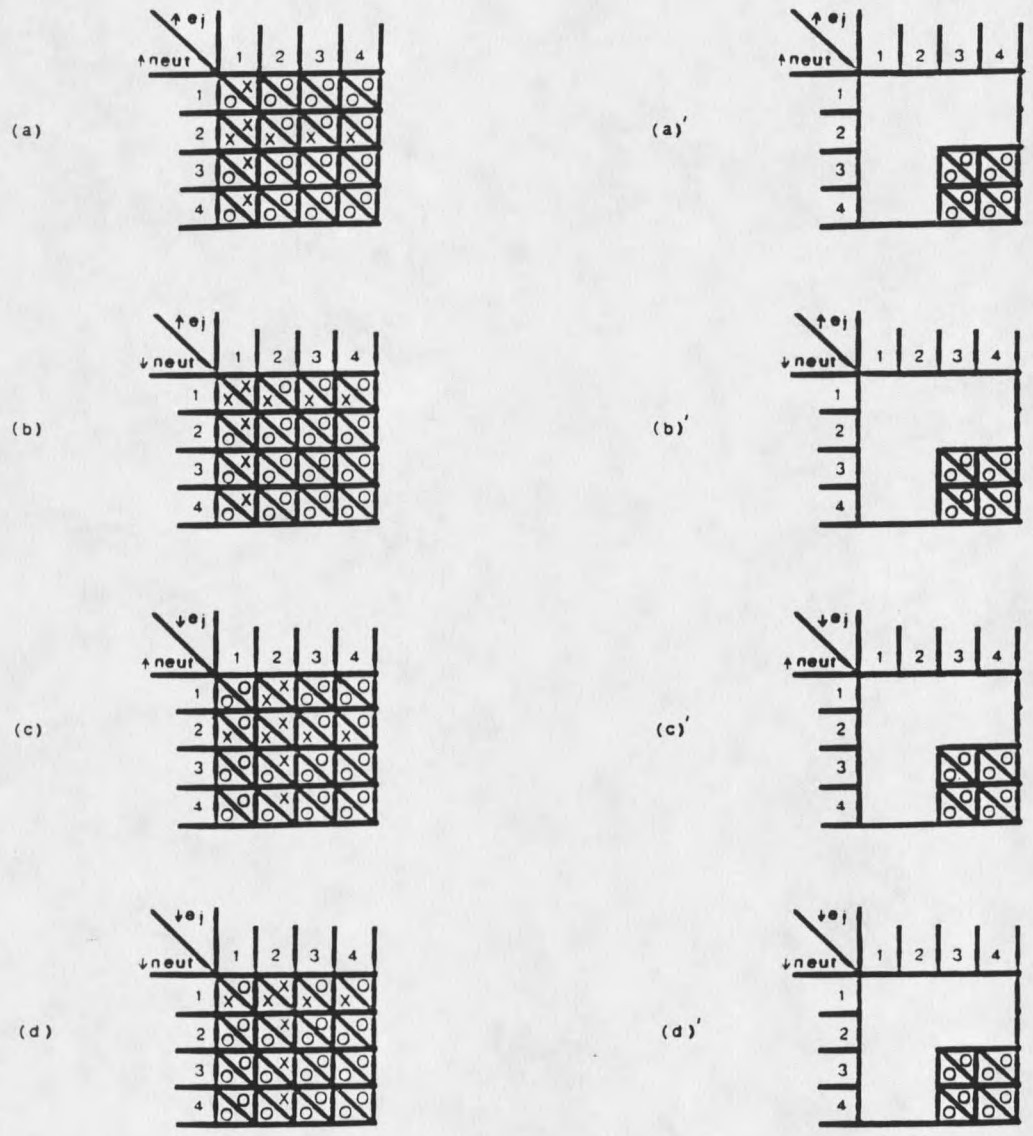

Figure 10. Calculational schemes ((a), (b), (c) and (d)) for the estimation of polarization asymmetry A, and the calculational schemes ((a)', (b)', (c)' and (d)') for the estimation of the dilution effect A_{dil} for the polarization asymmestry. To compute the asymmetry parameter, we may sum up the intensities from the process (a) with that of (b), and subtract the sum of (c) plus (d), which will be divided by the total intensities (a) + (b) + (c) + (d).

the asymmetry calculation is given in Figure 11. The calculated polarization asymmetry is slightly higher than the experimental asymmetry, but they are in reasonably good agreement with each other.

From the consideration of the Auger neutralization mechanism, the polarization asymmetry A should be higher for the higher kinetic energy (around 13 eV) because the electrons with higher energy result from Auger neutralization and ejection processes in which the two electrons both originate near the Fermi level, where there is a very low population of majority spin electrons. As shown in Figures 6~9, the 3d electrons dominate the 4-sp electrons in the Auger electron emission, especially at higher energies for which the polarization asymmetry is largest. However the non-magnetic 4-sp electrons may contribute to the observed spectrum and dilute the spin asymmetry.

Dilution Effect of the Spin Asymmetry

As shown in Figure 10-(a),(b),(c) and (d), the spin-insensitive 4-sp electrons obviously contribute the observed polarization asymmetry parameters. Separating the contribution of the 3-d electrons for the spin-polarization asymmetry with that of 4-sp electrons, we can rewrite the equation 1-(1) as

$$A = \frac{1}{|P_z|} \frac{R_+(A_{3d}+A_{4sp}) - R_-(A_{3d}+A_{4sp})}{R_+(A_{3d}+A_{4sp}) + R_-(A_{3d}+A_{4sp})} \qquad \text{eq. 1-(26)}$$

where A_{3d} is the contribution of 3-d electrons for the

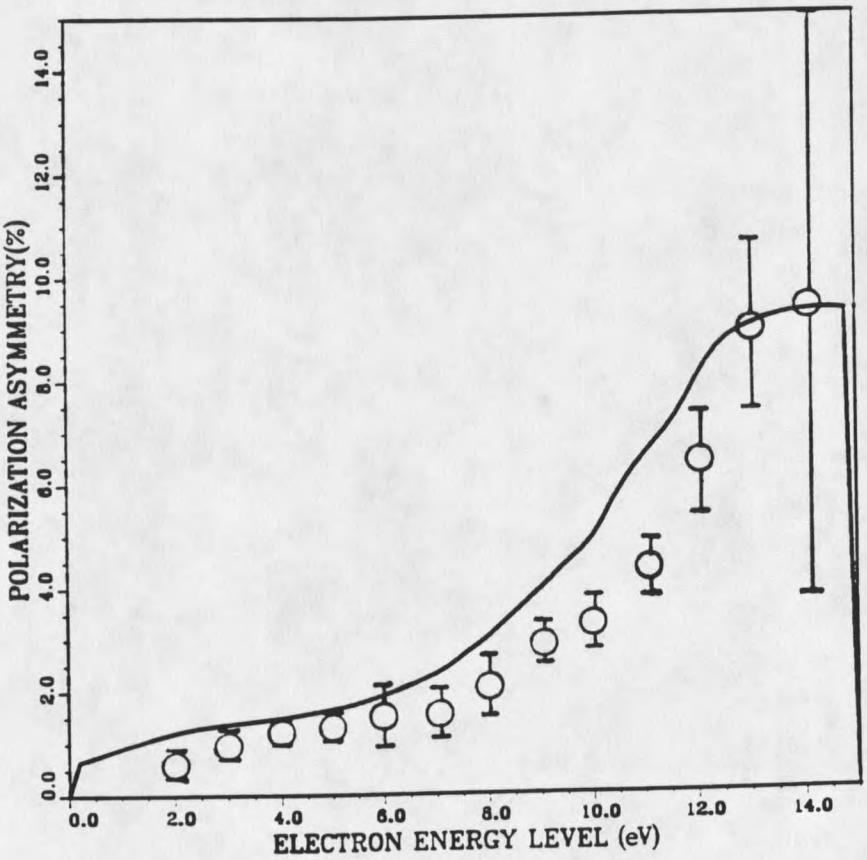

Figure 11. Calculated polarization asymmetry based on the schemes ((a), (b), (c) and (d)) in figure 10. The circles and vertical lines are the experimentally determined polarization asymetry and error bars, respectively.

asymmetry and A_{4sp} is the contribution of 4-sp electrons for the asymmetry. We define the net spin-polarization asymmetry, A_{net} as the following.

$$A_{net} = \frac{1}{|P_z|} \frac{R_+(A_{3d}) - R_-(A_{3d})}{R_+(A_{3d}) + R_-(A_{3d})} \qquad \text{eq. 1-(27)}$$

From the viewpoint of the Figure 10, we may rewrite A_{net} by

$$A_{net} = \frac{1}{|P_z|} \frac{[R_+(A_{3d}+A_{4sp}) - R_+(A_{4sp})] - [R_-(A_{3d}+A_{4sp}) - R_-(A_{4sp})]}{[R_+(A_{3d}+A_{4sp}) - R_+(A_{4sp})] + [R_-(A_{3d}+A_{4sp}) - R_-(A_{4sp})]} \qquad \text{eq. 1-(28)}$$

Note that we cannot merely expand $R_+(A_{3d}) + R_-(A_{4sp})$ to simplify equation 1-(28). Practically, we can estimate the term in eq. 1-(28) by utilizing Figure 10. To calculate $R_+(A_{3d} + A_{4sp})$ and $R_+(A_{4sp})$, we implement (a) + (b) and (a)′ + (b)′, respectively, in Figure 10. With the same logic we implement (c) + (d) and (c)′ + (d)′ for $R_-(A_{3d} + A_{4sp})$ and $R_-(A_{4sp})$, respectively. Therefore the dilution effect A_{dil}, which is shown in Figure 12, will be as

$$A_{dil} = A - A_{net} \qquad \text{eq. 1-(29)}$$

As expected, the parameters of A_{net} are generally bigger than those of A. Moreover the dilution effect is larger in the lower electron kinetic energy region, because this system has more populated d-electron SDOS near the Fermi level as we examine Figure 9. Without probing the dilution effect by the 4-sp electrons, the polarization asymmetry parameter A is almost meaningless at low electron energy.

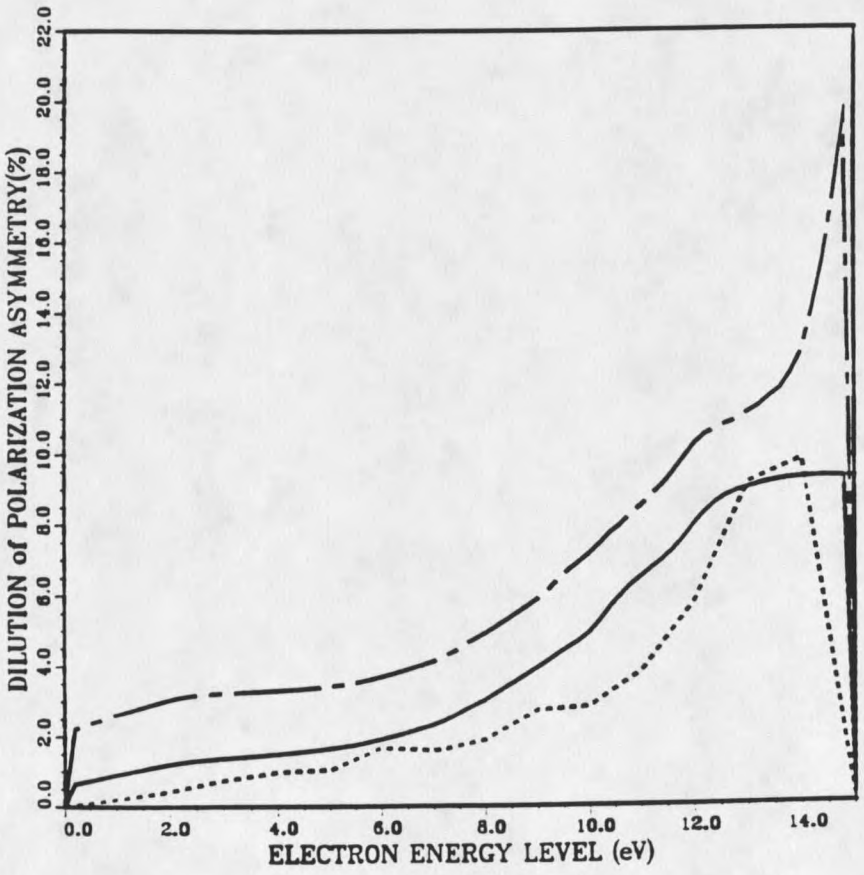

Figure 12. Net asymmetry polarization, A_{net} is represented as the chained line and the calculated polarization asymmetry is represented as the solid line. The dilution effect can be expressed by the difference between the chained line and the solid line. The dotted line represents the experimentally measured asymmetry (reproduced from [4(a)]).

Summary of the Results

1. We provided a theoretical model which enabled us to interpret the experimental data to probe the surface electronic and ferromagnetic properties of the transition metals.

2. The width of the minority and majority band in the Ni(110) sample was 4.5 eV and the exchange splitting between the majority and minority band was 1.3 eV.

3. The ratio of the magnitude of the unoccupied minority band to the occupied minority 3-d band was 0.6 out of 5.0. The ratio of the magnitude of the occupied sp band versus the occupied d band was 1.0 out of 6.0.

4. The calculated polarization asymmetry is almost the same as the experimentally observed asymmetry over a wide range of energies.

5. The magnitude of the dilution effect by the spin-insensitive 4-sp electrons in the Ni(110) system was elucidated.

THIN METALLIC FILMS OF COPPER ON RUTHENIUM: ELECTRONIC PROPERTIES OF INTERFACES

Background and Introduction

Introduction to a Bimetallic System

A bimetallic system, copper deposited on a ruthenium surface is used as a catalyst in several industrial processes [35], and will be a good model for studying the properties of more useful bimetallic catalysts.

The system prepared by vapor deposition of Cu on the Ru(0001) surface has been studied by using various surface science techniques [36~42]. This system has several interesting properties; (a) under certain conditions [36, 43] Cu vapor condenses on the Ru surface to form a two-dimensional submonolayer (rather than three-dimensional clusters), (b) the first Cu monolayer is pseudomorphic with respect to the Ru(0001) substrate, whereas successive layers grow epitaxially with a (111) orientation [41, 42], (c) since Cu and Ru are immiscible, no alloying takes place between the Cu layer and the Ru surface, (d) the Cu atoms desorb upon heating like an ordinary atomic adsorbate. These properties permit a degree of control, both of structure and composition, which is not possible for the industrially used bimetallic catalysts [35] whose components have a tendency to form solutions. Usually this makes it very difficult to prepare a desired surface composition and structure.

H. Tochihara and et. al. [36] studied the copper/ruthenium (0001) system by means of thermal desorption, work function measurement, and metastable quenching spectroscopy. They concluded that if the Ru(0001) surface was kept at room temperature and Cu vapors were condensed on it, the growth of a second Cu layer starts only after the first layer is completed and that the electronic properties of the first Cu layer differ from those of the second layer which, in turn, has similar properties to the outermost layer of the Cu(111) surface.

Several important questions are common to these studies and not yet answered. We would like to know (1) where and how the electronic and the chemical properties of a Cu monolayer on Ru are different from those of a clean surface, (2) know how many Cu layers are needed to make the influence of Ru on the outermost Cu layer disappear, (3) how the electronic properties of a Cu submonolayer will be changed, according to the changing surface coverage of Cu, etc. In terms of the energy band theory of electrons in metals, transition metals such as those of group VIII [44] possess d-bands whose states are not completely occupied by electrons. By contrast, the d-bands of non-transition metals such as those of group IB are completely filled.

In the case of the nickel-copper system, which can form solid solutions over the whole range of compositions, the substitution of copper atoms for nickel atoms in the metal

lattice adds electrons to the system. According to Mott and Jones [45], nickel-copper alloys would possess a single d-band rather than separate bands for the two components, and the additional electrons introduced with the copper would lead to an alloy with a more completely filled d-band. In this model of the electronic structure of a Ni/Cu alloy, no distinction was made between the chemical properties of nickel and copper atoms in the alloy. This behavior is in distinct contrast to that of the ruthenium-copper alloy.

To test the hypothesis that the catalytic activity of a group VIII metal [35] is associated with an unfilled d-band, various workers [46] determined reaction rates on alloys such as nickel-copper and palladium-gold as a function of composition. It was reasoned that the extent of filling of the d-band would be determined by the composition of the alloy, hence it should be possible to relate catalytic activity to d-band vacancies. Although many studies of this type were conducted, the approach was not very fruitful in elucidating the electronic factor in catalysis by metals. The work was based on the premise that the catalytic activity of a metal is determined by the electronic structure of the crystal. Today, this premise appears questionable [35]. It has been largely supplanted by the view that catalysis is determined by localized properties of surface sites. Experimental data [47, 48] on chemisorption and catalysis indicate that different types of atoms in the surface of an alloy such as Ni/Cu

largely retain their chemical identities, although their bonding properties may be modified.

We developed a semi-quantitative model for analyzing metastable quenching spectra, since this provides information on the electronic properties, including the surface density of energy states, for the various copper submonolayers while the surface coverage of Cu deposited on the Ru is shifting. In this way we know how the electronic properties of a Cu monolayer on Ru are different from those of pure copper, and may be able to predict how many Cu layers are required to make the electronic influence of Ru on the outermost Cu layer disappear.

The metastable quenching spectroscopy experiments expose the surface to a beam coming from a nozzle and containing a mixture of He atoms in the ground state and He atoms excited in the metastable 2^1S state. The excited He metastable atoms which come in contact with the surface are quenched to the ground state, and this process causes electron emission from the surface. The MQ spectrum is the plot of the kinetic energy distribution (i.e., the number of electrons having kinetic energy E, as a function of E) of the ejected electrons from the surface. Thus, The MQ spectra will be similar to ion neutralization spectroscopy (INS) [49~52], which is very surface specific.

Bimetallic Cluster Catalyst

For a bimetallic catalyst to be of practical interest, a

high surface area is necessary. An effective approach toward creating high surface area is the dispersal of the bimetallic entity on a carrier. The highly dispersed bimetallic species obtained are called bimetallic clusters. Information on the structures of bimetallic clusters has been obtained with chemical probes, such as chemisorption and reaction rate measurements [53~55], and physical probes, such as X-ray diffraction [56], extended X-ray absorption fine structure (EXAFS) [57] and angle-resolved ultraviolet photoemission spectroscopy (ARUPS) [41].

Supported bimetallic clusters can be prepared simply by contacting a suitable carrier such as silica or alumina with an aqueous solution of salts of the two metals. The material is then dried and contacted with a stream of hydrogen at a temperature high enough to accomplish reduction of the metal precursors to the metallic state. This procedure results in the formation of very small metal clusters dispersed on the surface of the carrier.

Study of Properties of Monolayer Ni/Cu Films on the Ru(0001)

Bimetallic systems have been the focus of considerable attention recently due to the superiority of such combinations over the individual metal components in catalytic activity [37], selectivity, and resistance to poisoning. Bimetallic catalysts are useful for comparing electronic (or ligand) effects with geometric (or structural) effects. Cu dosed up to 1 monolayer (ML) forms a dispersed and ordered film. Upon

annealing to 300K well ordered 2D islands pseudomorphic to the Ru(0001) substrate are formed. The electronic properties of the first Cu ML are dramatically altered from those of the bulk Cu(111) surface. A set of Cu/Ru interface and Cu surface sites, resulting from the strong Cu_{3d}-Ru_{4d} interaction, have been identified by angle-resolved photoemission [41]. The second ML also grows in ordered 2D islands but the structure is periodically strained and contains periodic misfit dislocations.

Ni/Ru(0001) differs from Cu/Ru(0001) in that the Ni layer is stable against high temperature annealing while the Cu layer is unstable after the second full overlayer is formed. For Cu/Ru(0001), charge transfer from Cu to the more electronegative Ru pulls out electrons from the Cu_{4s} orbitals.

Study on Ni-Cu Alloys

Ni-Cu alloys provide a good example of a bimetallic catalyst system [55] in which the variation of catalytic activity with composition depends markedly on the type of reaction, thus leading to substantial selectivity effects.

Evidence [54] that the surface compositions of the Ni-Cu catalysts are different from the bulk compositions is provided by information on the chemisorption of hydrogen on the catalysts at room temperature. This evidence is based on the observation that strong chemisorption of hydrogen does not occur on copper. If accumulation of one of the components in the surface serves to lower the surface energy of the system,

the surface will be enriched in this particular component. It is found that the addition of only a few percent of copper to Ni decreases the amount of strongly chemisorbed hydrogen several-fold, which suggests that the concentration of copper in the surface is much greater than in the bulk.

It was discovered [35] that the activity of the group VIII metals for hydrogenolysis reaction of hydrocarbons was decreased markedly by the presence of a group IB metal. It was shown that the inhibition of hydrogenolysis leads to improved selectivity for alkane isomerization reactions. Also, it was discovered that bimetallic systems of interest were not limited to combinations of metallic elements that are highly miscible in the bulk. For example, the Ru-Cu system exhibits selective inhibition of hydrogenolysis similar to that observed with the Ni/Cu system. Results of studies with catalyst combinations consisting of two metallic elements from group VIII of the periodic table were also interesting.

Characteristics of the MQ Spectra of Ru and Cu

The MQ spectrum of clean Ru in Figure 13 shows a sharp peak at 10.2 eV below the Fermi level. This ruthenium peak is shifted gradually to 9.4 eV, corresponding to increasing surface coverage toward a Cu monolayer on Ru, and this peak seems unchanged as more Cu deposited on Ru to a 3.4 Cu multi-monolayer. This may suggest that Ru still influences the surface of the Cu monolayers. On the other hand, a shoulder

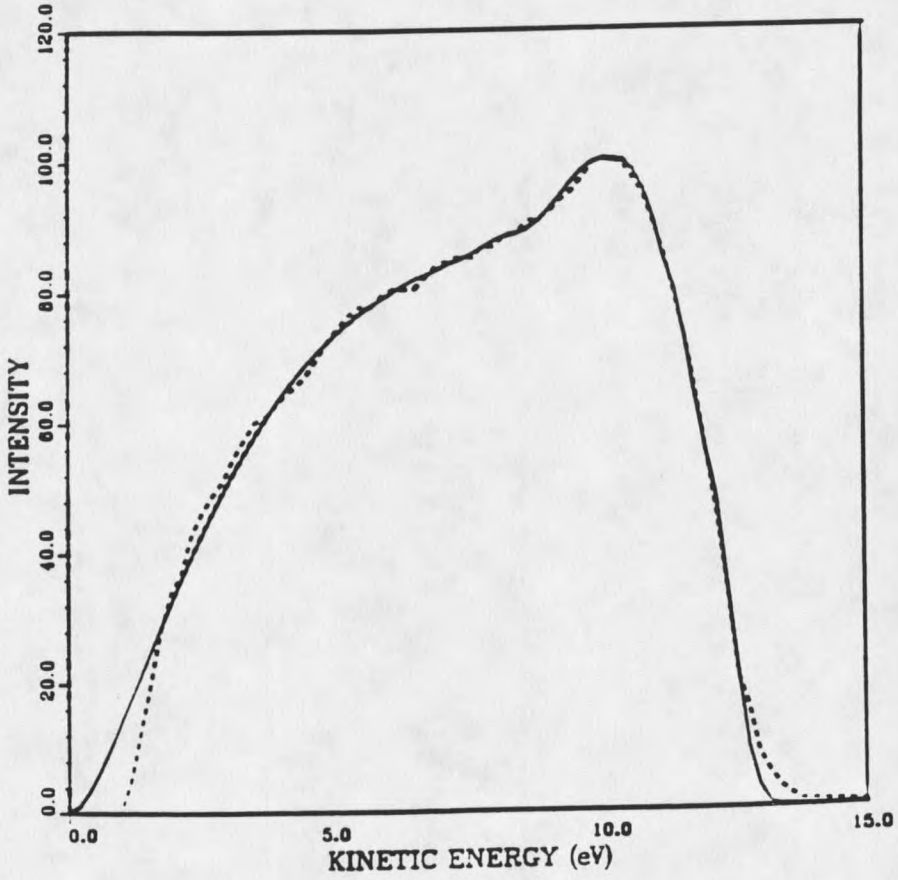

Figure 13. Computer-generated IN spectrum of a clean Ru surface (the solid line). The experimental data is shown along the dotted line.

peak comes out around 12.0 eV energy level for the Cu submonolayer and turns to be a characteristic Cu peak in multi-monolayers of Cu.

Method to Interpret the Experimentally Observed Spectra

We generated a computer-simulated IN spectra based on the equations derived in the previous part of this dissertation [43, 51], whose output is a set of parameters for the surface density of states. The computer-simulated spectra was compared with the experimental spectra for the calculation of the difference in shape between them. This information was fed back to the computer program to produce another IN spectrum for a better fit to the experimental one, and a new set of SDOS parameters. This iterative computation was continued until the difference in shape between the computer-generated spectra and the experimental one was minimized. Thus, we can obtain the variables of the surface density of states of the clean Ru and Cu, and the submonolayers of Cu on Ru.

Numerical Values of the Input Data for Computer-generated Spectra

We selected 5.3 eV and 5.0 eV for the work function of ruthenium and copper [42], respectively, and calculated 0.94 1/Å for the 4-d band exponential decay parameter and 0.31 1/Å for that of 5-sp band for ruthenium. We also calculated 0.80 1/Å for the 3-d band and 0.23 1/Å for 4-sp band parameter for copper. The decay parameter λ in the Thomas-Fermi potential

was chosen as 0.25 1/Å for our calculation.

Results and Discussion

Electronic Properties of Pure Thin Metal Films

Our computer-produced IN spectra of a clean Ru surface appears in Figure 13 and the density of states (dos) with three (3) 4-d band dos parameters and four (4) 5-sp band dos parameters appears in Figure 14. There is a huge, localized 4-d electron population (95 %) of surface density of states at and near the Fermi due to the fact that Ru has a predominant 4-d band structure, coming from its electronic configuration, [Kr] $5s^1$ and $4d^7$. This is also evidenced from the shape of the Ru spectra, which show a large peak at the high energy level. The proportion of 5-sp band dos is 5% and this fact explains that there is large energy gap between its 4-d and 5-sp band and the 4-d electrons of Ru contribute little to the 5-sp energy states. The highly localized dos ranges from the Fermi level to 4 eV below the Fermi level. This is in good agreement with the report of other workers [49].

The best fit IN spectrum to the experimental spectrum of Cu multi-monolayer is shown in Figure 15, and the sdos is shown in Figure 16. There is a large and sharp peak around 2.5 eV below the Fermi level and this unique dos peak is recognized from the large peak in the Cu IN spectrum. The 3-d band dos is still localized and occupies a large proportion (85%).

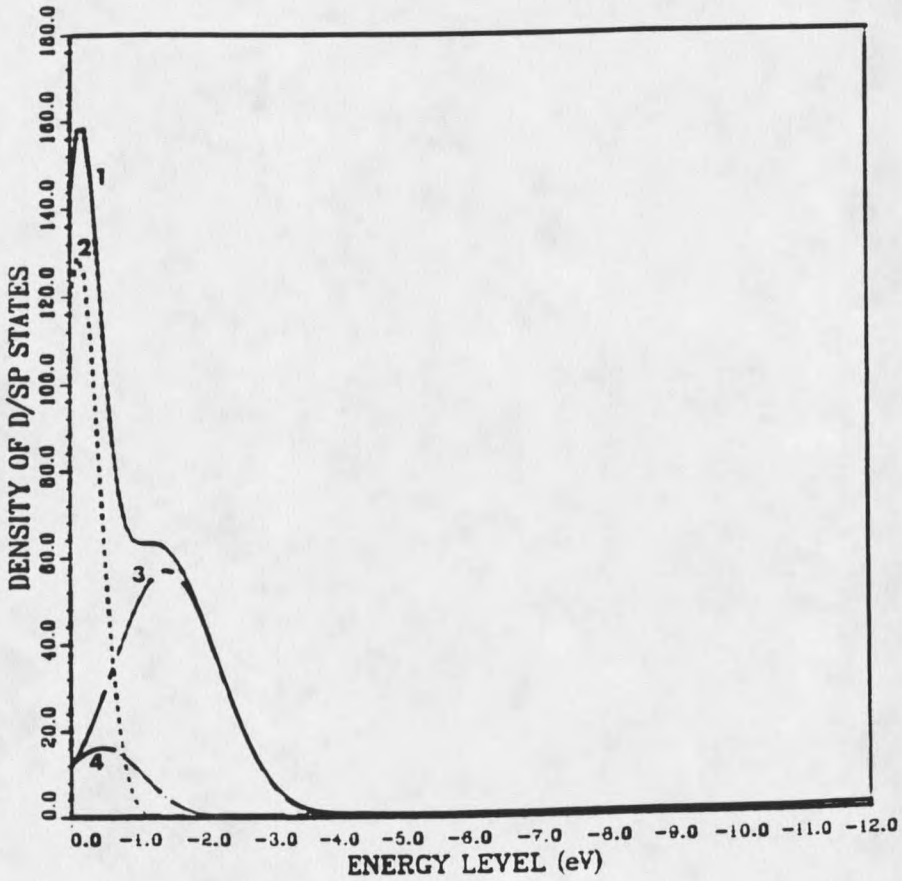

Figure 14. Density of state of clean Ru with three d-band DOS parameters (lines 2, 3, 4) and four sp-band DOS parameters (lines 5, 6, 7 and 8). They are negligibly small and not shown. The total DOS is shown along the line 1.

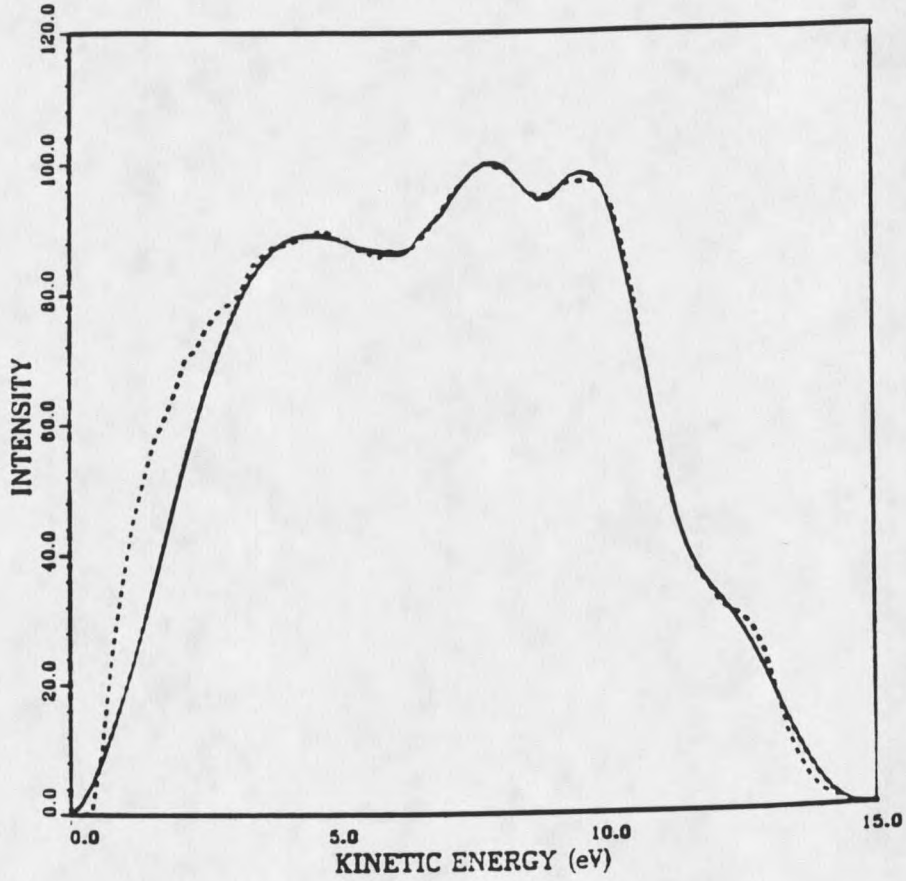

Figure 15. IN spectrum of 3.41 monolayer of Cu (the solid line). The experimental data is shown along the dotted line.

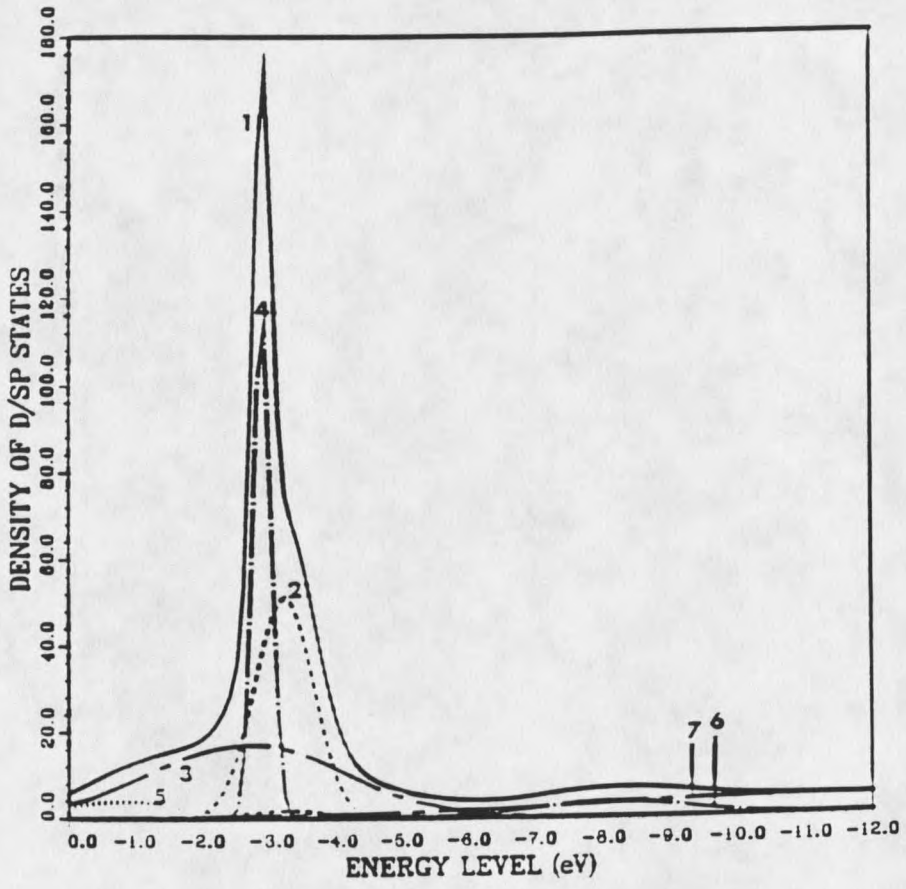

Figure 16. Density of states of 3.41 Cu monolayer. The d-band DOS consists of the lines 2, 3 and 4, and the sp-band DOS is small (lines 5, 6 and 7). The total DOS is shown along the line 1.

The 4-sp band dos is broad and dispersed over the entire energy range. The normalized proportion of sp-band density is 15%, although the electronic configuration of Cu is [Ar] $4s^1$ $3d^{10}$. This indicates that the energy gap between 3-d and 4-sp is narrower than that of Ru (4-d and 5-sp) and the 3-d electrons contribute significantly to its 4-sp band states. Our calculation for the sdos matches well with the report of other researchers [45].

Electronic Properties of Interfacial Cu/Ru(0001) System

The computer-simulated spectrum of a 0.21 submonolayer of Cu on Ru(0001) is featured in Figure 17, which is a best fit to the experimental spectrum. Based upon this computed spectrum, the sdos is featured in Figure 18. The huge and sharp dos peak in Figure 14 is shifted down to near 1.0 eV below the Fermi level. The second d-band dos positioned between the Fermi and 4.0 below the Fermi is not changed at all. The third d-band dos appears for the first time, and is the characteristic d-band dos of Cu. Note that the total sp-band dos is slightly increased over that of pure Ru.

The IN spectrum of 0.52 monolayer of Cu is shown in Figure 19 and the sdos is shown in Figure 20. The first d-band dos localized near the Fermi in Figure 14, is considerably broadened. The band width of the second d-band dos is not changed, however the intensity is decreased. The third d-band dos is very localized between 2.5 eV and 3.5 eV below the Fermi level and its intensity is moderately

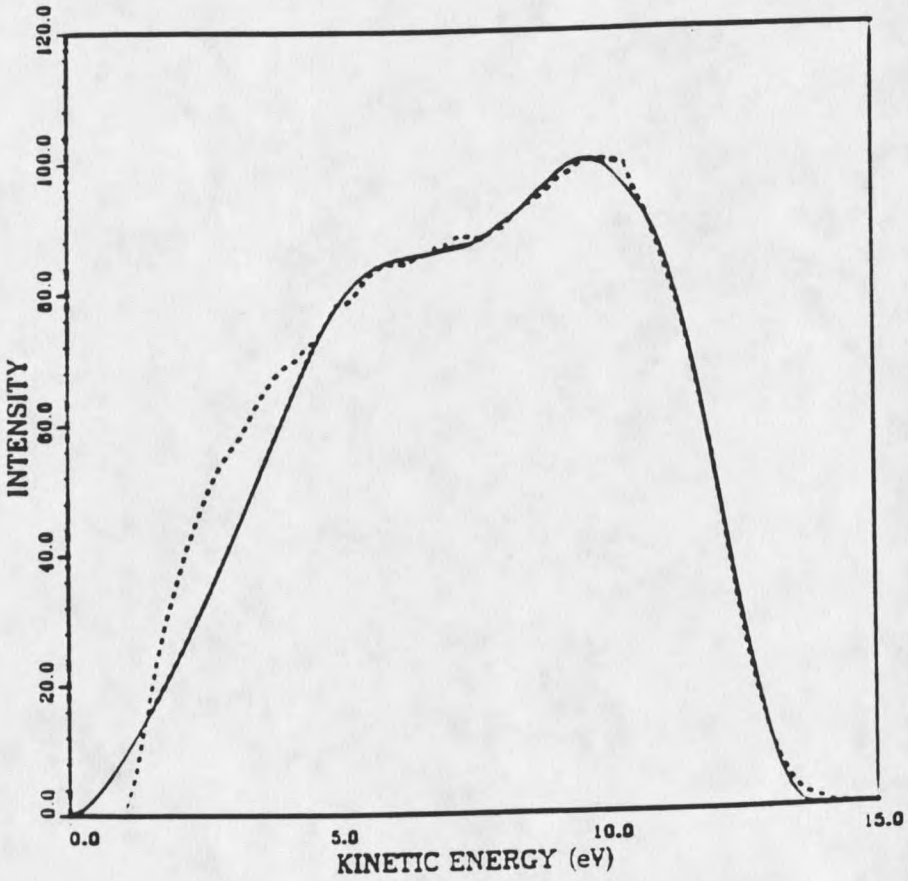

Figure 17. IN spectrum of 0.21 monolayer of Cu (the solid line). The experimental data is shown along the dotted line.

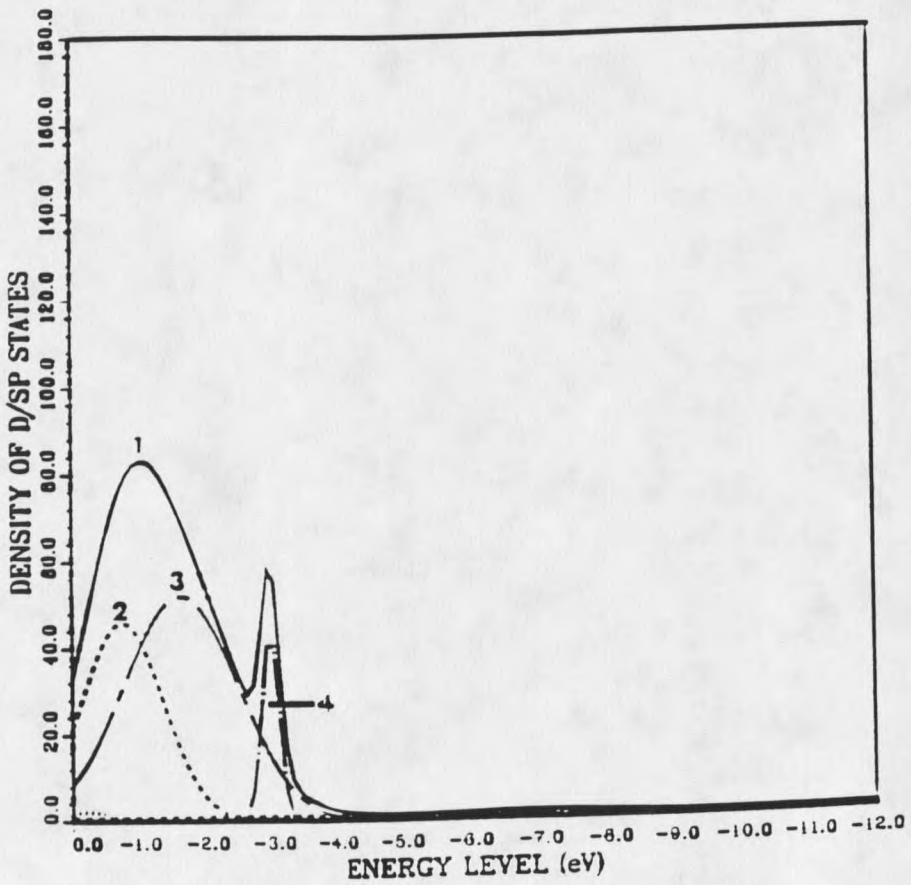

Figure 18. Density of states of 0.21 Cu monolayer. The d-band DOS consists of the lines 2, 3 and 4, and the sp-band DOS is negligibly small.

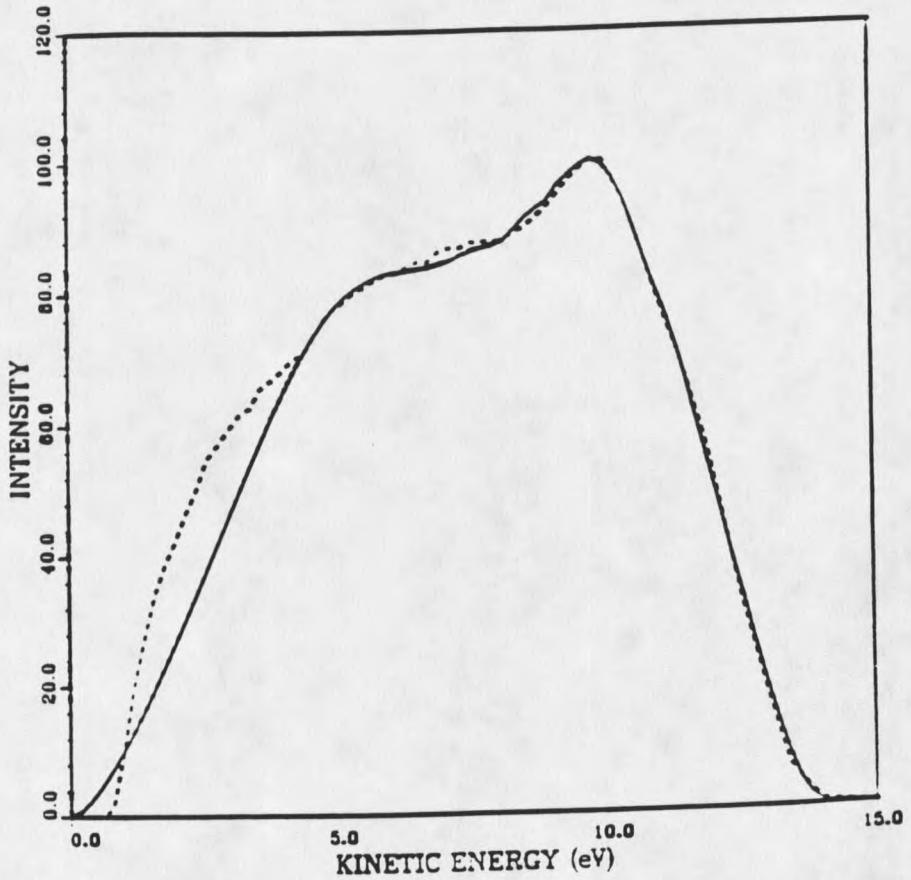

Figure 19. IN spectrum of 0.52 monolayer of Cu (the solid line). The experimental data is shown along the dotted line.

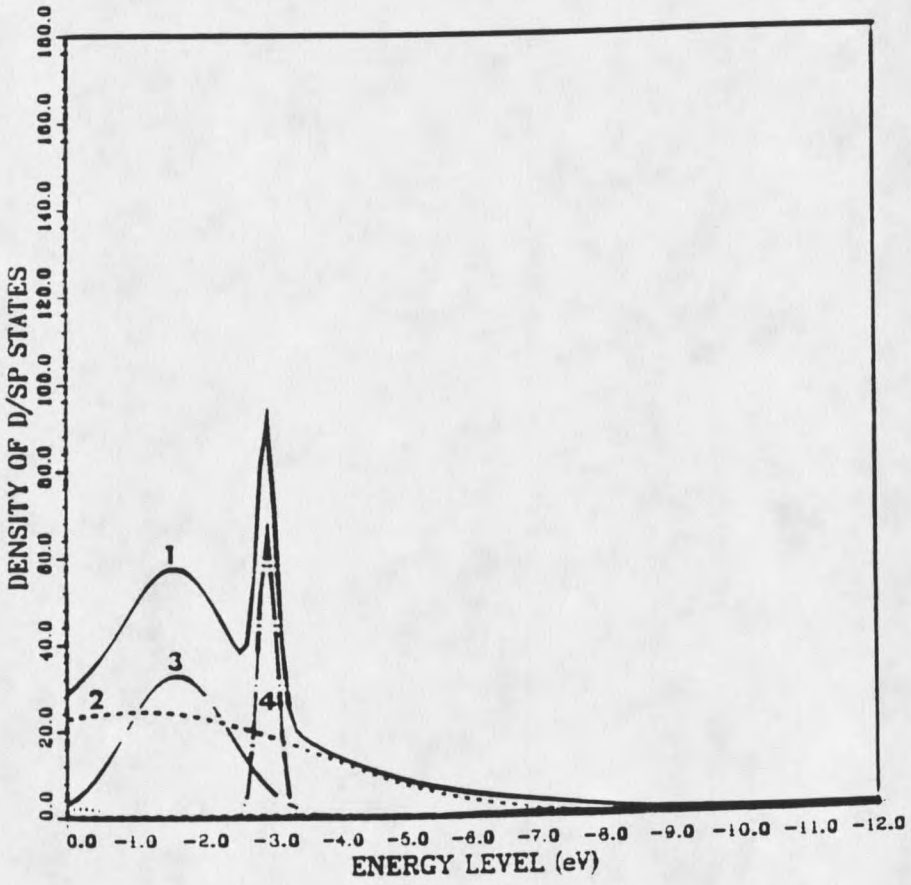

Figure 20. Density of states of 0.52 Cu monolayer. The d-band DOS consists of the lines 2, 3 and 4, and the sp-band DOS is small. The total DOS is shown along the line 1.

increased as the Cu coverage is increased. The total population of sp-band dos is still small, about 6%.

The IN spectrum of the 0.83 monolayer is featured in Figure 21. The surface density of states is featured in Figure 22. The first d-band dos is decreased and little bit localized. The proportion of the second d-band dos is not changed, but the shape is widened. The third d-band dos is sharpened remarkably and increased, reflecting that the Cu coverage is increased. The total population of the sp-band is not altered. The IN spectrum of 1.01 Cu coverage is shown in Figure 23 and the sdos is in Figure 24. The first d-band dos is decreased moderately and the shape and size of the second d-band dos are not changed. The third d-band dos is raised as the Cu coverage is increased. The IN spectrum of the 3.41 multi-monolayer is shown in Figure 15 and the sdos is in Figure 16. As the surface coverage is changing from 0.21 monolayer to 1.01 Cu overlayer, the position of first d-band dos is shifted from 1.5 to 2.8 eV below the Fermi, and its band width is widened. The second d-band dos is gradually decreased and also the band width increased, but the midpoint of the band is not shifted. The intensity of the third d-band dos is increased steadily as the Cu coverage is increased, but its position is shifted down from the Fermi level to 3.0 eV below the Fermi. For the total sdos of d-band, the population of the d-electrons at the Fermi level is large, however it is

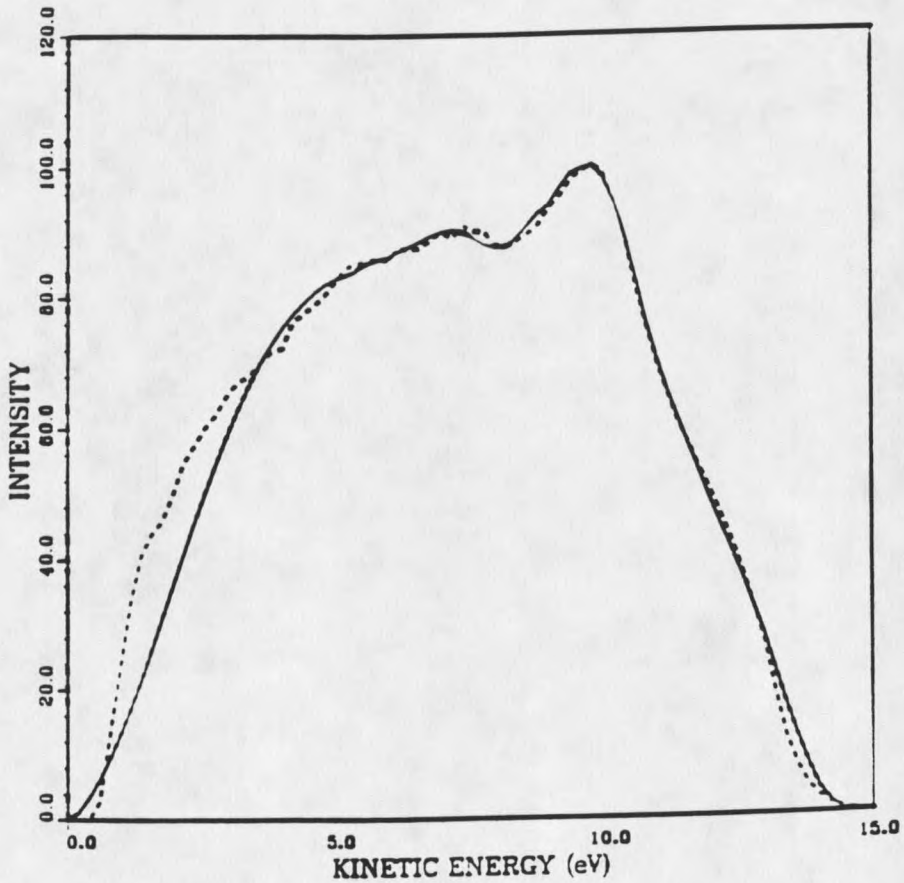

Figure 21. IN spectrum of 0.83 monolayer of Cu (the solid line). The experimental data is shown along the dotted line.

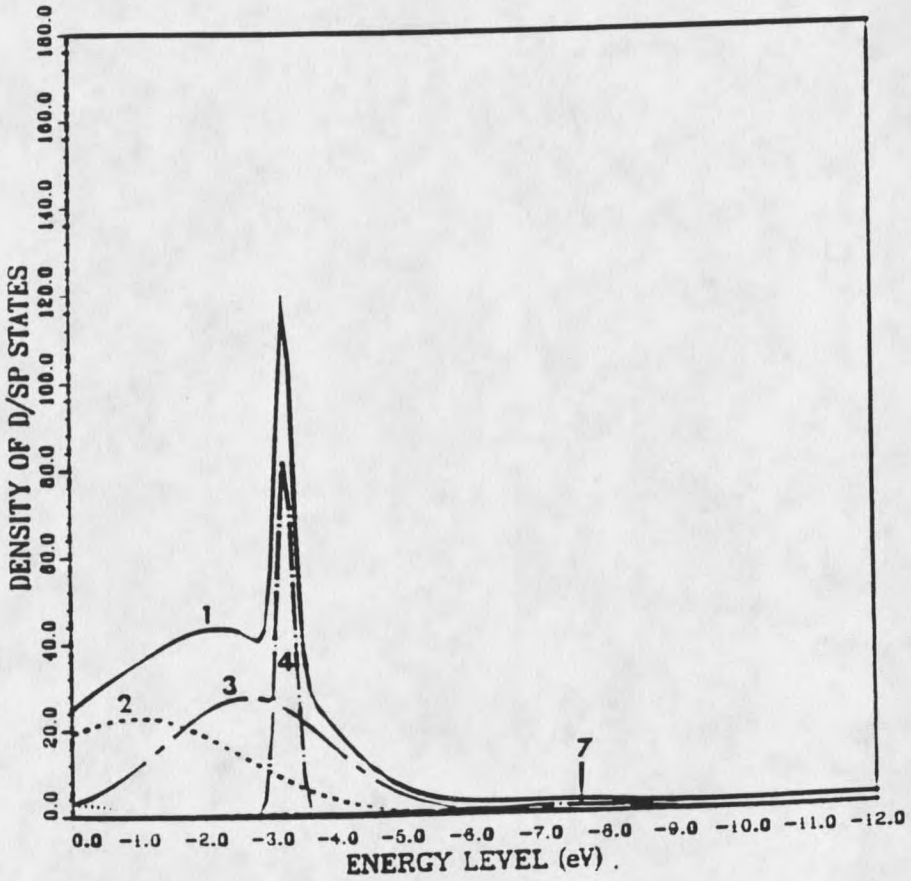

Figure 22. Density of states of 0.83 Cu monolayer. The d-band DOS consists of the lines 2, 3 and 4, and the sp-band DOS is still small compared to that of d-band (the line 7 is included). The total DOS is shown along the line 1.

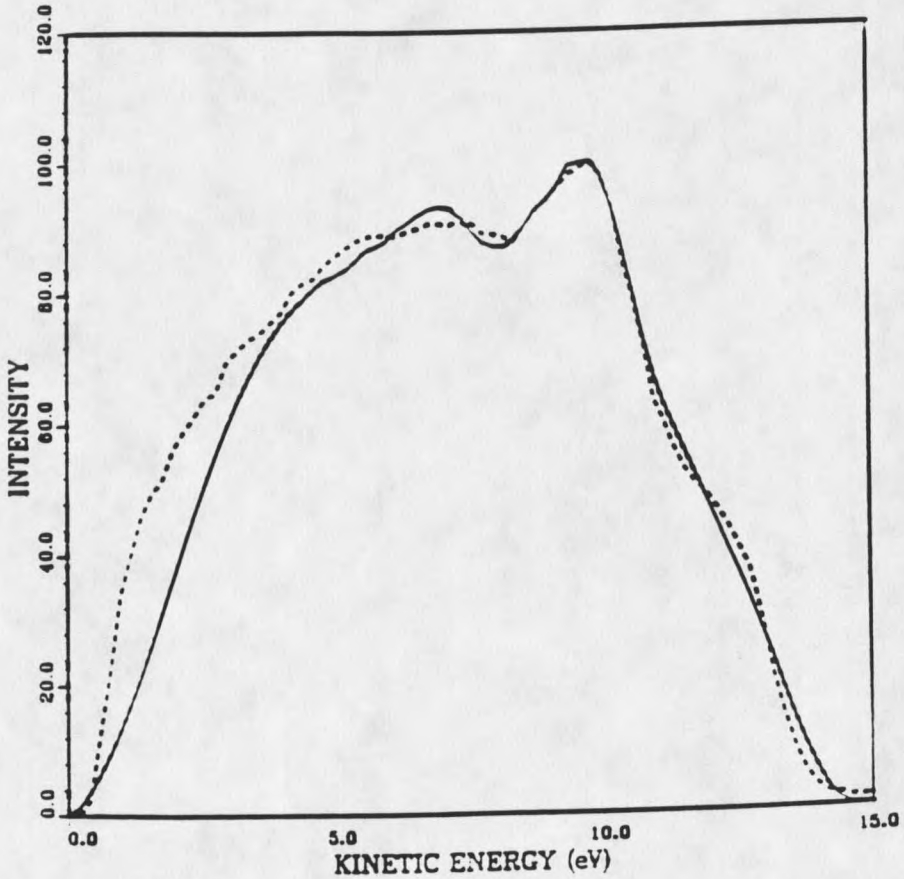

Figure 23. IN spectrum of 1.01 monolayer of Cu (the solid line). The experimental data is shown along the dotted line.

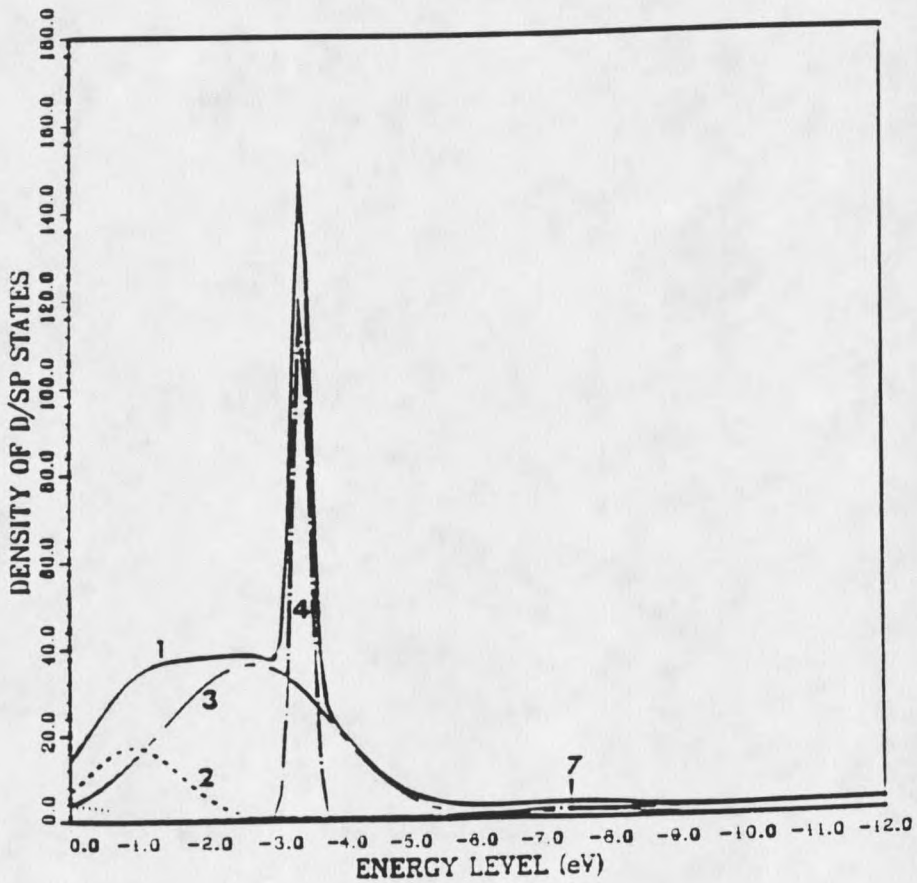

Figure 24. Density of states of 1.01 Cu monolayer. The d-band DOS consists of the lines 2, 3 and 4, and the sp-band DOS is small (the line 7 is included). The total DOS is shown along the line 1.

lowered as Cu coverage increases. Note that the increase of intensity of the third d-band dos is directly proportional to the increase of Cu coverage. The relative population of electrons in the sp-band to that of d-band increases very slightly as the Cu coverage changes. Examining the overall change of the sdos from 0.21 to 1.01 Cu monolayer, we observed that the large population of sdos near the Fermi level is spread and shifted down by 2~4 eV, except the third d-band dos.

Analysis of Surface Density of States to Predict the Actual Surface Coverage of Cu on Ru

With the consideration of the atomic size of Ru and Cu, the exponential decay parameters of Cu and Ru, and their immiscibility, the surface electrons of Cu located above Ru atoms will preferentially neutralize the incoming helium metastable ion with a certain possibility for Ru to neutralize the helium metastable. This may affect the electron kinetic energy distribution, which means that the He^+-neutralizing effect of Cu on Ru by the above-mentioned environment is manifestly affected in the distribution which is the basis for calculation of surface density of states of the metal surfaces and interfaces.

To properly predict the real surface coverage of Cu on Ru, we need to compute the difference between the values of the optimized surface density of states (sdos) and the computer-generated composite sdos which are composed from the

values of sdos set of clean Ru and the multi-monolayer of Cu on Ru. Then we need to find the minimum of the differences of the two sets of sdos, at which we can find the real surface coverage. The values of the optimized surface density of states of several Cu sub-monolayers are shown in Table 2.

In order to provide the composite SDOS, we constructed the composite SDOS by two means... linear and non-linear. The linear method means that if the actual Ru coverage is x_1 ($0.0 \le x_1 \le 1.0$), the coverage of Cu must be $1.0-x_1$. Non-linear method implies that if the real Ru coverage is x_{nl} ($0.0 \le x_{nl} \le$), the coverage of Cu could be any variable y_{nl}, satisfying its boundary condition ($0.0 \le y_{nl} \le 1.0$). We may describe the linear method first. We denote x, y and z as the surface density of states (SDOS) of 4-d band and a, b, c and d as the SDOS of 5-sp band of clean Ru surface. Again we denote x′, y′and z′ as the SDOS of 3-d band, and a′, b′, c′ and d′ as the SDOS of 4-sp band of clean Cu (or Cu multi-monolayers on Ru). Then we may construct the d- and sp-band composite SDOS of the sub-monolayers in terms of linear combination of the coefficients (Θ_{fi} and $1.0-\Theta_{fi}$) of the SDOS of the d- and sp-band of clean Ru with those of multi-monolayer Cu on Ru (or clean Cu) as

$$x'' = \theta_{fi}x + (1.0 - \theta_{fi})x' \qquad a'' = \theta_{fi}a + (1.0 - \theta_{fi})a'$$

$$y'' = \theta_{fi}y + (1.0 - \theta_{fi})y' \qquad b'' = \theta_{fi}b + (1.0 - \theta_{fi})b' \qquad \text{eq. 2-(1)}$$

$$z'' = \theta_{fi}z + (1.0 - \theta_{fi})z' \qquad c'' = \theta_{fi}c + (1.0 - \theta_{fi})c'$$

$$d'' = \theta_{fi}d + (1.0 - \theta_{fi})d'$$

Table 2. The surface density of states of various Cu submonolayers and monolayers on Ru, including that of clean Ru.

(a) Characteristic parameters of the Gaussian functions optimized in surface density of states of clean ruthenium

Gaussian function Label: i	Amplitude A	Width (in eV)	Mean position (in eV)
x	529.39	0.30	-0.12
y	233.19	0.78	-1.39
z	66.41	0.59	-0.45
a	1.06	0.13	-4.33
b	1.54	0.07	-0.00
c	0.62	0.06	-0.10
d	4.81	7.33	-12.00

(b) Characteristic parameters of the Gaussian functions optimized in surface density of states of 3.41 Cu multi-monolayer on Ru

Gaussian function Label: i	Amplitude A	Width (in eV)	Mean position (in eV)
x′	100.50	0.43	-3.16
y′	34.06	1.48	-2.67
z′	222.36	0.13	-2.87
a′	7.90	0.83	-0.79
b′	3.66	0.57	-3.20
c′	7.02	1.15	-7.99
d′	8.42	4.05	-11.17

(c) Characteristic parameters of the Gaussian functions optimized in surface density of states of 0.21 Cu submonolayer on Ru

Gaussian function Label: i	Amplitude A	Width (in eV)	Mean position (in eV)
x′′ (0.21)	176.12	0.60	-0.74
y′′ "	195.89	0.85	-1.61
z′′ "	165.90	0.13	-2.95
a′′ "	8.48	0.39	-0.17
b′′ "	4.27	2.56	-2.78
c′′ "	3.79	1.09	-6.86
d′′ "	4.22	4.14	-11.25

Table 2. -- Continued

(d) Characteristic parameters of the Gaussian functions optimized in surface density of states of 0.52 Cu submonolayer on Ru

Gaussian function Label: i	Amplitude A	Width (in eV)	Mean position (in eV)
x''(0.52)	102.36	2.58	-1.01
y'' "	136.99	0.74	-1.60
z'' "	271.93	0.13	-2.89
a'' "	9.94	0.38	-0.15
b'' "	3.06	2.28	-2.78
c'' "	4.36	0.98	-6.86
d'' "	4.67	4.05	-11.20

(e) Characteristic parameters of the Gaussian functions optimized in surface density of states of 0.83 Cu monolayer on Ru

Gaussian function Label: i	Amplitude A	Width (in eV)	Mean position (in eV)
x''(0.83)	62.14	1.58	-0.99
y'' "	74.41	1.25	-2.63
z'' "	234.54	0.13	-3.17
a'' "	7.28	0.60	-0.12
b'' "	1.48	0.88	-3.04
c'' "	4.54	1.06	-7.08
d'' "	5.43	4.05	-11.28

(f) Characteristic parameters of the Gaussian functions optimized in surface density of states of 1.01 Cu monolayer on Ru

Gaussian function Label: i	Amplitude A	Width (in eV)	Mean position (in eV)
x''(1.01)	89.00	0.25	-0.83
y'' "	82.81	1.09	-2.90
z'' "	263.38	0.13	-3.14
a'' "	6.71	0.84	-0.21
b'' "	1.53	1.81	-3.46
c'' "	4.56	1.06	-7.43
d'' "	6.72	3.89	-11.42

where x'', y'' and z'' are the composite SDOS of the d-band and a'', b'', c'' and d'' are the composite SDOS of sp-band of the sub-monolayers. Those 7 variables indicated as double prime consist of a set of the composite SDOS. As we vary the coefficients θ_{fi}, we can produce the computer-generated sets of the composite SDOS of concerned surface coverage of Cu on Ru surface, according to eq. 2-(1). We may compare the set of variables of composite SDOS with that of optimized SDOS and calculate the difference between the two sets. We repeat the same calculations successively for the changing Θ_{fi} from 0.0 to 1.0 and subsequently estimate the minimum of the differences between the two sets and identify the coverage at the minimum.

We report that for 0.21 monolayer of Cu, the minimum of the differences is found at 0.37 Cu coverage and that for each of 0.52, 0.83 and 1.01 monolayer of Cu, the minimum is found at 0.60, 0.68 and 0.81 coverage of Cu, respectively.

We performed the non-linear method to provide the composite SDOS of d- and sp-band of the sub-monolayers in terms of non-linear combinations of the coefficients (Θ_{gi} and Θ_{gj}) of the SDOS of d- and sp-band of clean Ru and with those of multi-monolayer Cu as

$$\begin{aligned} \overline{x} &= \theta_{gi}\, x + \theta_{gj}\, x' & \overline{a} &= \theta_{gi}\, a + \theta_{gj}\, a' \\ \overline{y} &= \theta_{gi}\, y + \theta_{gj}\, y' & \overline{b} &= \theta_{gi}\, b + \theta_{gj}\, b' \\ \overline{z} &= \theta_{gi}\, z + \theta_{gj}\, z' & \overline{c} &= \theta_{gi}\, c + \theta_{gj}\, c' \\ & & \overline{d} &= \theta_{gi}\, d + \theta_{gj}\, d' \end{aligned} \qquad \text{eq. 2-(2)}$$

where $\bar{x}$, $\bar{y}$ and $\bar{z}$ are the composite SDOS of d-band and $\bar{a}$, $\bar{b}$, $\bar{c}$ and $\bar{d}$ are the composite SDOS of sp-band of the sub-monolayers. We define the boundary condition of Θ_{gi} and Θ_{gj} as $0.0 \leq \Theta_{gi} \leq 1.0$ and $0.0 \leq \Theta_{gj} \leq 1.0$. As we change the coefficients Θ_{gi} and Θ_{gj}, we may produce a great number of sets of 7 composite SDOS which satisfy the eq. 2-(2). Every time we compared it with the optimized SDOS and repeatedly calculate the difference of the two sets. Then we obtain a number of calculations of differences between the two sets of SDOS as the sets produced and estimate the minimum to identify best Ru and Cu coverages (we denote these as Θ_{hi} and Θ_{hj}, respectively). To examine how good Θ_{hi} and Θ_{hj} are for the other electron energy (level), we should provide another composite SDOS of d- and sp-band as

$$\hat{x} = \theta_{hi}\, x + \theta_{hj}\, x' \qquad \hat{a} = \theta_{hi}\, a + \theta_{hj}\, a'$$
$$\hat{b} = \theta_{hi}\, y + \theta_{hj}\, y' \qquad \hat{b} = \theta_{hi}\, b + \theta_{hj}\, b' \qquad \text{eq. 2-(3)}$$
$$\hat{z} = \theta_{hi}\, z + \theta_{hj}\, z' \qquad \hat{c} = \theta_{hi}\, c + \theta_{hj}\, c'$$
$$\hat{d} = \theta_{hi}\, d + \theta_{hj}\, d'$$

where $\hat{x}$, $\hat{y}$ and $\hat{z}$ are the composite SDOS of d-band and $\hat{a}$, $\hat{b}$, $\hat{c}$ and $\hat{d}$ are that of sp-band, by using the best selected Ru and Cu coverage. We then compare a set of these 7 composite SDOS (which satisfy the eq. 2-(3)) with the set of 7 optimized SDOS in the full range of electron energy (practically from 0.0 eV to 12.0 eV below the Fermi level) and calculate the differences and sum up the differences at a particular energy level. We iterate the same calculations for each electron

energy level for every Θ_{gi} and Θ_{gj}, to look for the best set of Θ_{hi} and Θ_{hj} to obtain the minimum of the summed-up differences. We finally identify the Ru and Cu coverages (we again denote these as Θ_{ii} and Θ_{ij}) of the sub-monolayer concerned. We report the results of this non-linear method compared with the linear method in Table 3.

Table 3. Cu coverages in Cu sub-monolayers on Ru, determined by an experiment[a], a linearly calculated method[b] and a non-linear calculated method[c]. The numbers in parenthesis are Ru coverages

Experimentally[a] calculated determined	Linearly[b] calculated Cu coverage	non-linearly[c] calculated Cu coverage
0.21	0.37 (0.63)	0.31 (0.59)
0.52	0.60 (0.40)	0.50 (0.38)
0.83	0.68 (0.32)	0.60 (0.29)
1.01	0.81 (0.19)	0.71 (0.14)

The result of this non-linear calculation indirectly suggests the structure of Cu submonolayers on Ru (the pattern of Cu deposition on Ru). At lower Cu coverage, the Cu vapor may deposit the Ru surface sites in completely disordered manner, forming two dimensional (2-D) clusters. However at relatively higher Cu coverage, Cu may deposit on the surface sites in an ordered manner so that 2-D and/or 3-D islands may develop before completion of the first monolayer. Our data in Table 2 may suggest that the 2-D and/or 3-D Cu island become shaped around 0.5 Cu monolayer.

Conclusions

1. The surface density of states of clean Ru is mainly distributed between the Fermi level and 3.0 eV below the Fermi level with a huge and sharp peak at the Fermi. The sdos of the 4d-band of Ru is predominant over that of the 5-sp band (95% vs. 5%).

2. In the copper overlayer on Ru, the sdos of the multimonolayer is spread over a wide range of energy level with a large and sharp peak between 2.5 and 4.0 eV below Fermi, which is characteristic of copper. The ratio of sdos of 3 d-band versus that of 4 sp-band is 3.5 to 1.0.

3. As the Cu film coverage on Ru is increased, the prominent peak of sdos of Cu grows steadily, while the sdos of Ru around the Fermi is shifted gradually down to 3.0 eV below the Fermi level, corresponding to the decrease in the influence of Ru.

4. The comparison of the calculated sdos of the Cu submonolayers with those of the computer-generated, composite sdos of the various surface coverage reveals in non-linear calculation that the sdos of the 0.21 Cu monolayer is best fit to the sdos of the 0.31 Cu coverage, 0.52 to that of 0.50, 0.84 to that of 0.60, and 1.01 to that of 0.71.

5. The results of non-linear calculation indirectly implies the pattern of Cu deposition on Ru as the Cu coverage increases to form a complete monolayer.

A SIMPLE MODEL FOR PRECURSOR-MEDIATED ADSORPTION AND THERMAL DESORPTION: N_2 ON RU(001)

Introduction

Adsorption Process

The process of adsorption is a bimolecular reaction between surface sites and gas molecules. Events which lead to the formation of a stable chemisorbed adlayer when a gas molecule is incident on a solid surface can be briefly summarized as follows [59(a), 60]: (1) the gas molecule may be elastically scattered back into the gas phase without energy loss, (2) the molecule may lose sufficient translational energy to the crystal lattice to become trapped in a physisorbed state, (3) if an adsorbed state can be formed in the vicinity of the incident site, the molecule may pass directly through the physisorption potential energy well into a chemisorbed state, (4) if it is trapped in the physisorption well at the incident site, the molecule may (4a) become chemisorbed, (4b) be inelastically scattered back into the gas phase, or (4c) hop to a neighboring site, (5) during formation of the chemisorbed species, chemical energy is available as the transfer from a physisorbed state to a chemisorbed state is exothermic. In this process, the molecule may (a) lose sufficient chemical energy to the crystal lattice to be localized at the original state, (b) lose insufficient energy and hence make a limited number of diffusive hops until the

excess energy is dissipated, or (c) undergo continuous migration, depending on the following ratio: activation energy for migration versus absolute temperature.

At equilibrium the number of bare sites N_s may be written as the number of adsorbed molecules N_a and the total number of molecules in the gas phase N_g. Let the volume of the gas be V cm^3 and the area of the surface be S cm^2. Then the concentration in gas phase is $C_g=N_g/V$ molecules per cm^3, the concentration of bare sites is $C_s=N_s/S$ sites per cm^2, and the concentration of adsorbed molecules is $C_a=N_a/S$ molecules per cm^2.

The equilibrium constant for the adsorption process is defined [59(b), (c)] as

$$K_c = \frac{C_a}{C_g C_s} = \frac{N_a}{(N_g/V)N_s} = \frac{F_a}{F_g F_s}\exp(\epsilon/kT) \qquad \text{eq. 3-(1)}$$

where the F's are the partition functions per unit volume and ε is the energy released per molecule, at 0 K. This can be rewritten as

$$\frac{C_a}{C_g C_s} = \frac{f_a}{F_g f_s}\exp(\epsilon/kT) \qquad \text{eq. 3-(2)}$$

where f_a and f_s are the total partition functions. If θ is the fraction of the sites covered,

$$\frac{C_a}{C_s} = \frac{\theta}{1-\theta} = C_g\frac{f_a}{F_g f_s}\exp(\epsilon/kT) \qquad \text{eq 3.-(3)}$$

The concentration C_g is equal to P/kT and F_g may be written [59(b)] as

$$F_g = \frac{(2\pi mkT)^{3/2}}{h^3} b_g \qquad \text{eq. 3-(4)}$$

where b_g represents the rotational and vibrational factors in the partition function. The partition function f_s may be taken as unity because the adsorption sites have little freedom of motion. The partition function f_a for the adsorbed molecules principally involves internal factors, which may be written as b_a. Therefore, the adsorption isotherm becomes as

$$\frac{\theta}{1-\theta} = p\frac{h^3}{(2\pi m)^{3/2}(kT)^{5/2}}\frac{b_a}{b_g}\exp(\epsilon/kT) \qquad \text{eq. 3-(5)}$$

With the application of absolute rate theory [60,61], the equilibrium between the activated complex and the reactants can be expressed in a form like eq. 3-(1) as

$$\frac{C}{C_g C_s} = \frac{f^*}{F_g f_s}\exp(-\epsilon_1/kT) \qquad \text{eq. 3-(6)}$$

The partition functions $f^{\ddagger}$ and f_s relate to unit surface area, and F_g relates to unit volume. The energy ε_1 is the energy of the activated complexes with reference to the reactants at absolute zero. The partition function F_g can be factored into translational, rotational, and vibrational parts. One of the vibrational factors corresponds to a loose vibration, and may be expressed as kT/hν. For the localized activated complexes, eq. 3-(6) may be expressed as

$$\frac{C_{\neq}}{C_g C_s} = \frac{f_{\neq}(kT/h\nu)}{F_g f_s}\exp(-\epsilon_1/kT) \qquad \text{eq. 3-(7)}$$

where the partition function $f_{\ddagger}$ lacks the contribution for the one degree of freedom. $f_{\ddagger}$ differs from $f^{\ddagger}$ in lacking $kT/h\nu$. By rearrangement, we obtain the following.

$$\nu C_{\neq} = C_g C_s \frac{kT}{h}\frac{f_{\neq}}{F_g f_s}\exp(-\epsilon_1/kT) \qquad \text{eq. 3-(8)}$$

The frequency ν is the frequency of vibration of the activated complexes in the degree of freedom corresponding to their transformation into adsorbed molecules. The expression on the left-hand side of eq. 3-(8) represents the rate of the adsorption process. There are no translational and rotational factors in $f_{\ddagger}$ and the remainder, due to vibration, will be represented by $b_{\ddagger}$. As mentioned above the function f_s is taken as unity. Then the rate of adsorption V_1 is as

$$V_1 = \nu C_{\neq} = C_g C_s \frac{kT}{h}\frac{b_{\neq}}{\left(\frac{(2\pi mkT)^{3/2}}{h^3}\right)b_g}\exp(-\epsilon/kT) \qquad \text{eq. 3-(9)}$$

If the gas is diatomic, the factor b_g contains the rotational factor $8\pi^2 IkT/\sigma h^2$ [62, 63], where σ is the symmetry number. Similarly $b_{\ddagger}$ is very close to unity, apart from a symmetry factor $1/\sigma_{\ddagger}$. Therefore the rate of adsorption can be written as follows.

$$V_1 = C_g C_s \frac{kT}{h} \frac{1/\sigma_*}{\frac{(2\pi mkT)^{3/2}}{h^3} \frac{(8\pi^2 IkT)}{h^2}} \exp(-\epsilon_1/kT) \qquad \text{eq. 3-(10)}$$

and

$$V_1 = C_g C_s \frac{\sigma}{\sigma_*} \frac{h^4}{8\pi^2 I(2\pi mkT)^{3/2}} \exp(-\epsilon_1/kT) \qquad \text{eq. 3-(11)}$$

In many cases two adjacent sites (dual sites) are necessary for adsorption [59(b)]. If the surface is bare, the number of dual sites is related to the number of single sites as follows: s is known as the coordination number and depends upon the particular type of surface lattice. If the number of dual sites were evaluated by counting s for each single site, the result would be sC_s, but in this procedure each pair is counted twice. Therefore, we could rewrite eq. 3-(11) as

$$V_1 = \frac{1}{2} s C_g C_s \frac{\sigma}{\sigma_*} \frac{h^4}{8\pi^2 I(2\pi mkT)^{3/2}} \exp(-\epsilon_1/kT) \qquad \text{eq. 3-(12)}$$

This expression is only valid for the initial rates of adsorption on dual sites. If the fraction of surface sites already covered is θ, the average number of bare sites adjacent to any given site is $s(1-\theta)$. The total number of bare dual sites is $1/2\ \{C_s s(1-\theta)\}$. If the concentration of covered single sites is C_a, Θ is as

$$\theta = \frac{C_a}{C_a + C_s} \qquad \text{eq. 3-(13)}$$

The concentration of bare dual sites is as

$$C_{s_2} = \frac{1/2(C_s^2 s)}{C_a + C_s} \qquad \text{eq. 3-(14)}$$

Then we get

$$V_1 = \frac{sC_gC_s^2}{2(C_a+C_s)} \frac{\sigma}{\sigma_*} \frac{h^4}{8\pi^2 I(2\pi mkT)^{3/2}} \exp(-\epsilon_1/kT) \qquad \text{eq. 3-(15)}$$

The rate equations are quite different if the molecules are not localized in the adsorbed state. The equilibrium between initial and activated states may be represented [60] by

$$K_c = \frac{C_*}{C_g} = \frac{N_*/s}{N_g/V} = \frac{F^*}{F_g} \qquad \text{eq: 3-(16)}$$

where F_g and $F^{\ddagger}$ are the partition functions of gas in unit volume and of activated complex per cm^2, respectively. By the same methods we have used previously, the rate of adsorption is given [64] as

$$V_1 = C_g \frac{kT}{h} \frac{F_*}{F_g} \exp(-\epsilon_1/KT) \qquad \text{eq: 3-(17)}$$

The activated complexes now differ from the reactants by having translational freedom in only two dimensions, and the ratio $F_{\ddagger}/F_g$ is simply $h/(2\pi mkt)^{1/2}$. Then

$$V_1 = C_g \frac{kT}{h} \frac{h}{(2\pi mkT)^{1/2}} \exp(-\epsilon_1/kT) \qquad \text{eq. 3-(18)}$$

By the same method, the process of desorption of undissociated molecules held in a localized layer was considered [59(b)]. If N_a and $N_{\ddagger}$ are the numbers of adsorbed molecules and activated

complexes, and C_a and $C_{\ddagger}$ are the corresponding concentrations, the concentration of activated complexes is given [59(b), 63] by

$$C_{\neq} = C_a \frac{f^{\neq}}{f_a} \exp\left(-\frac{\epsilon_{-1}}{kT}\right) \qquad \text{eq. 3-(19)}$$

The equilibrium between the initial and activated states may be written as,

$$K_c = \frac{C_{\neq}}{C_a} = \frac{N_{\neq}/s}{N_a/s} = \frac{f_{\neq}}{f_a}\exp(-\epsilon_{-1}/kT) \qquad \text{eq. 3-(20)}$$

where ε_{-1} is the activation energy for desorption at the absolute zero. Application of the methods used earlier gives rise to the rate expression of desorption as

$$V_{-1} = C_a \frac{kT f_{\neq}}{h f_a}\exp(-\epsilon_{-1}/kT) \qquad \text{eq. 3-(21)}$$

where $f_{\ddagger}$ differ from $f^{\ddagger}$ in no inclusion of the partition function ($kT/h\nu$) for passage across the potential energy barrier.

Thermal Desorption Process

By desorption is meant the cleavage of the adsorption bond and the resulting removal of adsorbed particles from the surface. The basic equation which describes the desorption of atoms or molecules from a surface is the rate equation of Frenkel [59(a), 65], as

$$\tau = \tau_0 \exp(E_d/kT) \qquad \text{eq. 3-(22)}$$

in which τ is the residence time on the surface, E_a is the adsorption energy, T is the surface temperature, and τ_0 is a preexponential factor. Experimental data are frequently fitted to the Frenkel equation for obtaining the values for the parameters and E_a, thus describing the given desorption process from the surface. As in the case of chemical reaction, a careful application of statistical mechanics [66] shows that the reaction rate depend upon entropy changes during the reaction. The effect can be substantial, altering the preexponential factor by orders of magnitude; however, the activation energy does not change. A similar entropy contribution could alter the desorption rate if there were surface relaxation or a change in molecular configuration during desorption.

The general dependence of the desorption rates R_d (desorbing particles per unit time and surface area) on the concentration of adsorbed particles per unit surface area N, and the temperature T can be written [67(a)] as

$$R_d = -\frac{dN}{dt} = f(T,N) \qquad \text{eq. 3-(23)}$$

and is analyzed in terms of an Arrhenius equation as

$$R_d = k_m N^m = N^m k_0^m \exp(-E_m/RT) \qquad \text{eq. 3-(24)}$$

where k_m is the rate constant, m is the formal order, and k_m^0 is the prefactor. The coverage dependence is usually assumed to be contained totally in the N^m term, and the temperature

dependence is in the exponential term. The rationale for the assumption of such a simple Arrhenius or Polanyi-Wigner equation [59(a), 62] is the basic concept that (1) the coverage term is produced by the number of particles taking part in the critical step, (2) the preexponential is equal to the frequency of attempts of the system to move in the direction of reaction, and (3) the exponential term represents the relative number of these attempts having the necessary minimum energy. For equation 3-(24), m is usually set equal to 1 or 2, corresponding to the true molecularity, and additional coverage dependence is expressed in term of changes of E_m and/or k^0. The value of E_m would be sum of the adsorption energy plus the activation energy of adsorption.

The basic problem of kinetics concerns the values of k^0, the prefactor. From the equation 3-(20), the dimensionless equilibrium constant for desorption can be written [67] as

$$K^* = \frac{f^*}{f^m}\exp(-E_o/RT) = \frac{N^*/N_s}{\frac{N^m}{N_s^m}} = \frac{N^* N_s^{m-1}}{N^m} \qquad \text{eq. 3-(25)}$$

The f's are the complete partition functions of the transition state and adsorbate, respectively, after extraction of the zero-point energy difference E_0. If one extracts the critical degree of freedom from $f^{\ddagger}$, which leaves $f_{\ddagger}$, and replaces it by a translation along the reaction coordinate, comparison with eq 3-(24) leads to the following equation.

$$k_m^0 = \kappa(\frac{kT}{h})(\frac{f_{\neq}}{f^m})N_s^{1-m} \qquad \text{eq. 3-(26)}$$

From the transition state theory [68], we obtain

$$K^* = \exp\left(-\frac{\Delta G_0^*}{RT}\right) = \exp\left(-\frac{(\Delta H_0^* - T\Delta S_0^*)}{RT}\right) \qquad \text{eq. 3-(27)}$$

Then eq. 3-(26) is equivalent to

$$k_m^0 = \kappa\left(\frac{kT}{h}\right)N_s^{1-m}\exp\left(\frac{\Delta S_0^*}{R}\right) \qquad \text{eq. 3-(28)}$$

The range of typical k^0 -values can be determined as follows: for the temperature range between 100~1000K, $k^0_{m=1} = kT/h = 10^{13}$ sec^{-1} and $k^0_{m=2} = (kT/h)N_s = 10^{-2}cm\ sec^{-1}$, if $\kappa = 1$ and $(f_{\ddagger}/f^m) = 1$ (or $\Delta S^{\ddagger} = 0$). The latter implies identical localization or configuration complexity for reactants and transition state. If the transition state is much more mobile than the reactants, k^0 will be larger than normal. The k^0 values below the normal ones must have the opposite meaning, for example, a transition state which is less mobile or more complex than the reactants.

Precursor-mediated Adsorption and Desorption

If the precursor state does not exist and chemisorption is a direct reaction, then one would expect the probability of chemisorption to be a stronger function of the gas temperature than of the surface temperature. On the other hand if the chemisorption reaction is mediated by a precursor state that has accommodated to the temperature of the surface, then one

would expect the surface temperature to be of primary importance in dictating the measured probability of chemisorption. There is a variety of experimental techniques that can be used to observe precursors on a surface directly [69]. At surface temperatures sufficiently low to stabilize the precursor, its existence can be verified with photoelectron spectroscopy and virtually inelastic electron scattering. At higher surface temperatures, where the fractional surface coverage of the precursor is negligible, its existence can be verified by the angular distribution of scattered molecular beams [70].

Precursors are often imagined to be physically adsorbed species with both a short life-time and a low concentration. The extrinsic precursor is the state which may be formed where the molecule lands on an occupied site. An extrinsic precursor may hop to another site or desorb since the site is already occupied. By definition a direct adsorption does not occur from this site. The intrinsic precursor is the state formed when the molecule lands on an empty site, giving it the possibility to either adsorb, hop to another site, or desorb.

A one-dimensional potential diagram for precursor states is presented in Figure 25. The intrinsic precursors are denoted by asterisks, whereas the extrinsic precursor are designated by primes. The activation energies of migration (hopping) of the precursors on the surface cannot be shown on this one-D diagram. The activation energy for migration of the

intrinsic precursor is defined as E_m^*, while that for migration from the extrinsic precursor is defined as E_m'. All the rate coefficients of adsorption, desorption, and migration are assumed to be of the form $k_i = k_i^{(0)} \exp(-E_i/kT)$, where i=a, d, and m.

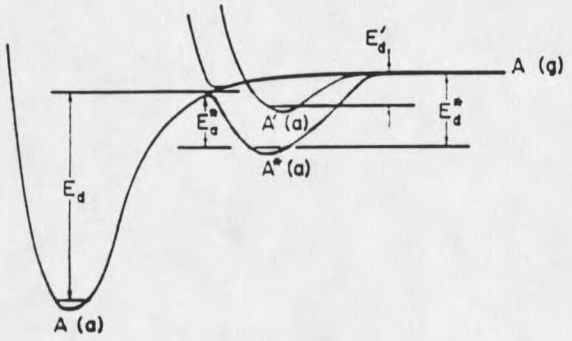

Figure 25. Schematic potential energy diagram describing precursor-mediated chemisorption and desorption.

Thus in the general case each precursor state is associated with two or three activation energies. For a general intrinsic precursor state these are E_a^* , E_d^* and E_m^* for adsorption, desorption and migration, respectively. One of the possible cases which we consider is the possibility that isolated chemisorbed species constitute an intrinsic precursor state. In this case E_a^* is zero as there is no distinction to be made between the precursor and the adsorbed species.

In the precursor-mediated molecular chemisorption process, molecules are placed sequentially onto surface sites to stimulate trapping from the gas phase into either a physically adsorbed intrinsic or extrinsic precursor state. Each precursor can either chemisorb, desorb, or migrate across

the surface in single hops to nearest neighbor sites. The precursor lives until it either chemisorbs or desorbs. The physically adsorbed intrinsic precursors experience lateral nearest neighbor (nn) and next-nearest neighbor(nnn) interactions with chemisorbed molecules such that the binding energy of the intrinsic precursor is given [69, 71] by

$$\epsilon_p = \epsilon_p^0 - \sum_j n_j \epsilon_r + \sum_k n_k \epsilon_a \qquad \text{eq. 3-(29)}$$

where ε_p^0 is the binding energy of an isolated intrinsic precursor, n_j is the occupation number of nn sites by chemisorbed molecules, n_k is the occupation number of nnn sites, ε_r is the pairwise additive (repulsive) nn interaction energy, and ε_a is the pairwise additive (attractive) nnn interaction energy. It is reasonably assumed that the precursors are bound to the surface by a periodic potential that can be represented by adjacent, interacting harmonic wells of which the minima are dictated by eq.3-(29).

The activation barrier (E_m) to precursor-state migration is defined as the difference of the energy at the interaction point between adjacent harmonic potentials. The ground state minimum at the occupation site may be written as

$$\epsilon_m = \epsilon_m^0 + \frac{\delta\epsilon_p(i,j)}{2} + \frac{[\delta\epsilon_p(i,j)]^2}{16\epsilon_m^0} \qquad \text{eq. 3-(30)}$$

where ε_m^0 is the activation barrier to migration for an isolated intrinsic precursor state molecule in the absence of lateral interactions with chemisorbed molecules, and $\delta\varepsilon_p(i, j)$

is the difference in precursor state binding energies or harmonic potential well depths between the i^{th} and j^{th} sites given by $[\varepsilon_p(i, j) = \varepsilon_p(j) - \varepsilon_p(i)]$. Thus the probability for precursor migration $P_m(i, j)$ is given by

$$P_m(i,j) = N\exp(-\epsilon_m/k_bT) \qquad \text{eq. 3-(31)}$$

where ε_m is the activation barrier to migration.

The probability for adsorption from the precursor state is given [69,71] by

$$P_d = NX\exp(-\epsilon_p/k_bT) \qquad \text{eq. 3-(32)}$$

where X is a dynamic factor representing the ratio between desorption and migration prefactors. The probability for precursor-mediated chemisorption (P_c) is determined from the initial, zero coverage, adsorption coefficient (s_o) and the binding energy of an isolated intrinsic precursor state molecule and is given by

$$P_c = NXs_0\exp\left(-\frac{\epsilon_0/k_bT}{1-s_0}\right) \qquad \text{eq. 3-(33)}$$

The relative probabilities for adsorption from the intrinsic precursor state, migration to adjacent sites, and molecular chemisorption are all functions of the extrinsic precursor binding energy.

To evaluate desorption rates, we need to calculate the rate of excitation from the chemisorbed state into the precursor state, and the rate of desorption from the precursor. The rate of desorption from the i^{th} chemisorption

site of which the occupation number is $\sigma(i)$, may be written as

$$\frac{d\sigma(i)}{dt} = A(\theta)\,\sigma(i)\exp(-\epsilon_b(i)/kT) \qquad \text{eq. 3-(34)}$$

where $\varepsilon_b(i)$ is the binding energy of the i^{th} particle with $A(\theta)$ being a coverage dependent prefactor as follows:

$$A(\theta) = A_0\exp(\alpha\theta) \qquad \text{eq. 3-(35)}$$

where α is the desorption preexponential coverage dependence. The coupled differential equations (eqs. 3-(34) and (35)) describing desorption from all chemisorption states can be solved numerically. The change in population of each chemisorption state may be calculated over a finite temperature interval. The desorption calculation can be repeated until all chemisorbed molecules are removed from the substrate surface, then a thermal desorption spectrum can be constructed.

Method and Calculation

Generalized Rate Expressions for Adsorption and Desorption

The rate expressions of both precursor-mediated adsorption and desorption based on either steady-state [72] or statistical models [73] can be derived for a variety of approximations concerning the nature of the precursor state [74]. Under equilibrium condition, a general kinetic scheme in which the intrinsic and extrinsic precursor states coexist is shown in Figure 26.

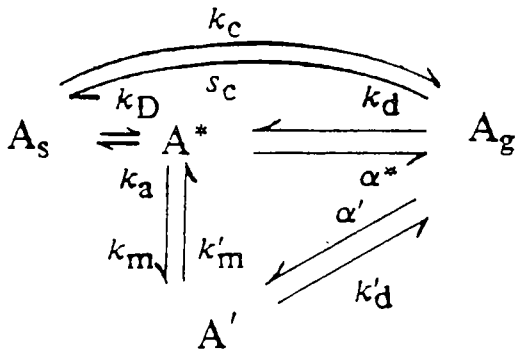

Figure 26. A kinetic scheme for precursor-mediated adsorption and desorption

In the above figure, chemisorbed species are represented as A_s, the intrinsic precursor as A^*, the extrinsic precursor as A' and the gas phase species as A_g. Here k_a, k_d, and k_m are the rate constants for adsorption, desorption and migration, respectively, from the intrinsic precursor state; k'_m and k^*_d are the rate constants for migration and desorption from the extrinsic precursor state and k_D is the rate constant for transfer from the chemisorbed state to the intrinsic precursor state; α^* and α' are trapping probabilities for molecules incident at intrinsic and extrinsic precursor sites, respectively. Direct transfer from the gas phase to chemisorbed state or vice versa is included through the probability S_c for adsorption and the rate constant k_c for desorption [74, 75].

A group of terms $F(\theta)$ can be introduced [74], in order to generalize the rate expressions as follows; F_d is the occupation probability that a site exists in a configuration which can lead to desorption. F_m is the probability that an

intrinsic precursor moves to a site configuration where an intrinsic precursor state can exist. F'_m is the probability that an extrinsic precursor moves to a site configuration where an intrinsic precursor state may exist. F_a is the probability that an intrinsic precursor state is at a site configuration where chemisorption can occur. F^* is the probability that a collision takes place at an intrinsic precursor site. F' is the probability that a collision takes place at an extrinsic precursor site. In general each of these F values will be a function of the surface coverage, θ.

We can apply the stationary state approximation for both desorption and adsorption to the kinetic schemes (in figure 25) with the assumption that the A^* and A' concentrations are negligibly small [59(a), 74] because the lifetime of the precursor state is very small compared to the chemisorption residence time. As a result, this leads to

$$k_D F_D - (k_d + k_a F_a + k_m F_m)[A^*] + k'_m F'[A'] = 0$$

$$k_m F_m [A^*] - (k'_d + k'_m F'_m)[A'] = 0$$

The rate of desorption, V_d and the rate of adsorption, V_a can be expressed as

$$V_d = k_d[A^*] + k'_d[A^*] + K_c F_D$$

$$V_a = k_a F_a [A^*] + S_c g F^* F_a$$

where $g = P/[(2\pi mkT)^{1/2}]$ is the collision rate per unit area. Therefore the general rate equations are obtained as

$$V_d = \frac{k_D F_D}{k_a F_a + k_d + \left(\frac{k_m F_m k_d'}{k_d' + k_m' F_m'}\right)} \left(k_d + \frac{k_d' k_m F_m}{k_d' + k_m' F_m}\right) + K_c F_d \qquad \text{eq. 3-(36)}$$

$$V_a = \frac{g K_a F_a \left(F^* + \frac{F' F_m' k_m'}{k' + k_m' F_m'}\right)}{k_a F_a + k_d + \frac{k_m F_m k_d'}{k_d' + k_m' F_m'}} + S_c g F^* F_a \qquad \text{eq. 3-(37)}$$

$F_m' = F^*$, and $F_m = F'$, equations 3-(36) and (37) are simplified to

$$V_d = \frac{k_D F_D \left(k_d + \frac{k_d' k_m F_m}{k_d' + k_m'(1 - F_m)}\right)}{k_a F_a + k_d + \frac{k_d' k_m F_m}{k_d' + k_m'(1 - F_m)}} + k_c F \qquad \text{eq. 3-(38)}$$

$$V_a = \frac{g k_a F_a F^* \left(\alpha^* + \frac{F_m' k_m'}{k_d' + k_m'(1 - F_m)}\right)}{k_a F_a + k_d + \frac{k_m F_m k_d'}{k_d' + k_m'(1 - F_m)}} + S_c g F^* F_a \qquad \text{eq. 3-(39)}$$

Application of the Rate Scheme to N_2/Ru(001) System

The precursor-mediated adsorption and desorption schemes were applied to the N_2/Ru(001) system, and produced a theoretical/computational yield for the desorption rate versus temperature and adsorption coefficient versus fractional coverage.

We first consider the temperature dependence of the rate equation. In the rate equations the temperature appears in the

equation. In the rate equations the temperature appears in the factor kT/h and also in the partition functions which involve the temperature to a simple power. Thus rate constants can be expressed in the form

$$k = A\ T^x \exp(-E_0/RT) \qquad \text{eq. 3-(40)}$$

Here x can be a variable to be determined by experiment. The values of x for each rate are determined to fit the experimental thermal desorption data. When the rate equation is written as a form of eq. 3-(40), the apparent energy of activation is temperature dependent. The experimental energy of activation E_{exp} is defined by

$$\frac{d\ln k}{dT} = \frac{E_{exp}}{RT^2} \qquad \text{eq. 3-(41)}$$

Differentiation of eq. 3-(40) gives as

$$\frac{d\ln k}{dT} = \frac{E_0 + xRT}{RT^2} \qquad \text{eq. 3-(42)}$$

and comparison of these two equations leads to the relationship,

$$E_{exp} = E_0 + xRT \qquad \text{eq. 3-(43)}$$

Unless x is very large or E_0 is very small, it may be difficult to detect this temperature dependence of the energy of activation.

To derive the rate of desorption, the rate constants in eq. 3-(38) are determined by implementing eq. 3-(40) for each

of the rate constants with the activation energies and prefactors, respectively. The values for the activation energies and prefactors in the table 4 are initially obtained from Redhead analysis [76], and adjusted to fit the proposed energy diagram in figure 25 with the kinetic and energetic parameters selected by Hood, et al. [71].

Table 4. Initial values for the activation energies and prefactors of the rate constants.

Rate constants	Activation energies (kj/mol)	Prefactors (1/sec)
k_D	20.9	1×10^{13}
k_a	13.5	5×10^{12}
k_d	6.7	5×10^{12}
k_d'	5.9	1×10^{10}
k_m	1.3	5×10^{12}
k_m'	1.3	1×10^{10}
k_c	26.3	1×10^{14}

However, the rate constants in equations 3-(38) should be calculated in a explicit form with coverage-dependent variables such as the activation energies and prefactors. Note that the coverage dependent activation energies and preexponentials from the experimental data [76~78] are shown in tables 5 and 6, respectively.

Table 5. Activation energies as a function of coverage.

Activation energies	Fractional coverage
42.2 - 27.5 θ	$0 < \theta < 0.08$
40.6 - 0.07 θ	$0.08 < \theta < 0.17$
41.5 - 8.90 θ	$0.17 < \theta < 0.22$
75.8 - 166.6 θ	$0.22 < \theta < 0.28$
29.2 - 4.62 θ	$0.28 < \theta < 0.52$

Table 6. Pre-exponentials as a function of coverage.

Preexponentials	Fractional coverage
$7.2\times10^{(16-21.0\theta)}$	$0 < \theta < 0.08$
$1.5\times10^{(15+10.2\theta)}$	$0.08 < \theta < 0.17$
$9.5\times10^{(16-4.6\theta)}$	$0.17 < \theta < 0.22$
$1.0\times10^{(31-75.3\theta)}$	$0.22 < \theta < 0.27$
$1.7\times10^{(11+4.0\theta)}$	$0.27 < \theta < 0.52$

Therefore we need to reform the rate equation 3-(38) into another equation containing coverage dependent variables. Because first order desorption is usually observed for weakly chemisorbed gases [67], like N_2 on Ru(001) system, we can represent the above as

$$V_d(\theta) = -\frac{d\theta}{dt} = k\theta = A_d \exp(-E_d/RT) \qquad \text{eq. 3-(44)}$$

By a rearrangement,

$$-\frac{d\theta}{dT} = -\frac{A_d}{\beta}\theta \exp(-E_d/RT) \qquad \text{eq. 3-(45)}$$

where A_d is the pre-exponential frequency factor. Note that $1/dt = \beta/dT$, where dt is the time increment, and β is a heating rate and is of the order of 10 K/s. Solving successively eq. 3-(44) for the surface coverages, we obtain

$$\theta_{n+1} = \theta_n \exp(-k\Delta t) = \theta_n \exp(-\frac{k\Delta T}{\beta}) \qquad \text{eq. 3-(46)}$$

or

$$\theta_{n+1} - \theta_n = \theta_n \, (\exp -[\frac{k\Delta T}{\beta} + 1]) \qquad \text{eq. 3-(47)}$$

As we determine the V_d in eq. 3-(38) for any particular

parameter k in the eq. 3-(46). Then the intensity of desorption as a function of surface coverage can be represented as the successive difference (for example, $\theta_{n+1} - \theta_n$) of the particular surface coverage. The entire calculation we described was repeated for the temperature increments from 78K to 155K. Our result of this computation is shown in Figure 27 and is in good agreement with the experimental spectrum [78]. The temperature at the maximum intensity peak can be derived by solving eq. 3-(45) as

$$\frac{d}{dT}\left(\frac{d\theta}{dT}\right)_{T=T_p} = 0 \qquad \text{eq. 3-(48)}$$

Then,

$$\frac{d}{dT}(\exp(-E_d/RT_p)) = \frac{E_d}{RT_p^2} \qquad \text{eq. 3-(49)}$$

Using eq. 3-(45), the eq. 3-(49) can lead to

$$\frac{E_d}{RT^2} = \frac{A_d}{\beta}\exp(-E_d/RT_p) \qquad \text{eq. 3-(50)}$$

It shows that the desorption intensity peak is at 115K at low surface coverage and the intensity is split into two as the surface coverage is increased. Thus for high coverage we have two peaks, the former at 120K (the inherent binding energy of this state is 9.0 kcal/mol) and the latter at 85K. Note that the temperature at the desorption peak is independent of initial surface coverage.

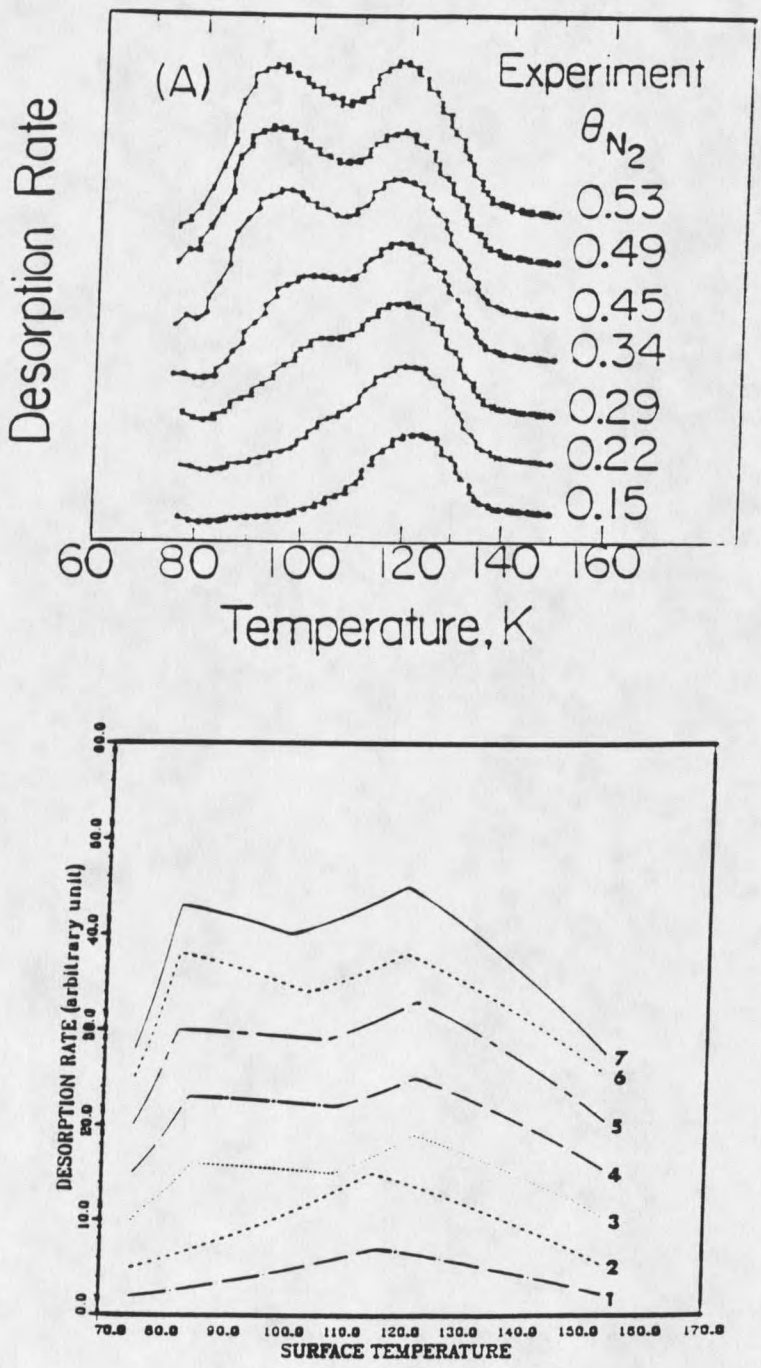

Figure 27. (A) Experimentally observed thermal desorption spectra. (B) Computer-generated thermal desorption spectrum for N_2/Ru(001). The line numbers 1, 2 , 3, 4, 5, 6 and 7 correspond to the N_2 surface coverages of 0.15, 0.22, 0.29, 0.34, 0.45, 0.49 and 0.53, respectively.

We consider an adsorption process. Chemisorption proceeds through a sequence in which the precursor state A^* or A' may be considered as a mobile species.

$$A_s \xleftarrow[k_{ad}]{} A^* \text{ or } A' \underset{k_{de}}{\overset{k_{tp}}{\rightleftharpoons}} A_g$$

Then the sticking coefficient should be considered for the following three successive processes [79]; (1) trapping of a molecule A into a precursor state with trapping rate constant k_{tp}, (2) desorption of A^* or A with a rate constant k_{de}, and (3) transition of the precursor state to the chemisorbed state with a rate constant k_{ad}.

Applying the steady state approximation for the precursor state, we have

$$[A^* \text{ or } A'] = \frac{k_{tp}\,[A]}{k_{ad} + k_{de}} \qquad \text{eq. 3-(51)}$$

Thus the interim rate of adsorption $v_{a,0}$ for the clean surface is as

$$v_{a,0} = \frac{k_{ad}\,k_{tp}\,[A]}{k_{ad} + k_{de}} \qquad \text{eq. 3-(52)}$$

From the kinetic theory of gases [80], we obtain k_{tp} as

$$k_{tp} = \alpha\,(\bar{v} / 4) \qquad \text{eq. 3-(53)}$$

where $\bar{v}$ is the mean molecular velocity and α is the trapping coefficient on the clean surface. From the definition [59(a), 79] the initial sticking coefficient s_0 will be as

$$S_0 = \nu_{a,0} / \nu_c = (\nu_{a,0}) / ((\nu/4)[A]) \qquad \text{eq. 3-(54)}$$

where ν_c is the rate of collision of A with the surface. Here s_0 and α are the initial sticking and trapping coefficient, respectively, on the clean surface. By combining eq. 3-(53) with eq. 3-(54), the initial sticking coefficient can be rearranged as

$$S_0 = \frac{\alpha}{1+\left(\frac{k_{de}}{k_{ad}}\right)} \qquad \text{eq. 3-(55)}$$

Typically, the initial sticking coefficient for adsorption of reactive gases such as N_2 and CO lies in the range 0.1 to unity [59(a)]. For a fractionally covered surface, the rate constant of adsorption k_{ad} should be modified in terms of a certain function of coverage $f(\theta)$, which may be of the form of $(1-\theta)^n$, then the sticking probability s can lead to

$$s = \frac{\alpha}{1+\frac{k_{de}}{k_{ad} f(\theta)}} \qquad \text{eq. 3-(56)}$$

Note that if $k_{de}/k_{ad} \ll 1$, which is observed on low-covered surfaces at low temperature, s stays almost equal to s_0 until relatively high values of θ are reached. This means the sticking probability shows a tendency to be independent of N_2 at low coverage. Because the adsorption coefficient is the flux of the molecules incident on the surface (given by g in the following equation, where p is the order of 10^{-6} torr),

$$g = \frac{P}{(2\pi mkT)^{1/2}}$$

multiplied by the rate of adsorption, the explicit functional form for our molecular adsorption may be identified in a form of eq. 3-(39) and is given as

$$V_a = \frac{k_a F_a F^* \left(\alpha^* + \dfrac{F_m' k_m'}{k_d' + k_m'(1-F_m)} \right)}{k_a F_a + k_d + \dfrac{k_m F_m k_d'}{k_d' + k_m'(1-F_m)}} + S_c F^* F_a \qquad \text{eq. 3-(57)}$$

By the same method for calculating the thermal desorption spectra, the rate constants in eq. 3-(57) were determined by using eq. 3-(40) with the coverage dependent parameters in Tables 5 and 6. The adsorption coefficients as a function of surface of coverage at the surface temperature of 90K were obtained and appear in figure 28. Our calculated adsorption coefficients are in good agreement with experimentally determined adsorption coefficients [71, 78].

We have few references for the studies of the coverage dependence of the adsorption coefficient $s(\theta)$ for well defined surface layers [77, 78, 81]. In most cases, s did not change significantly with increasing coverage or dropped gradually. In our case, s did not decrease at low coverages ($\theta < 0.2$). However at the coverages greater than 0.2, s decreased gradually.

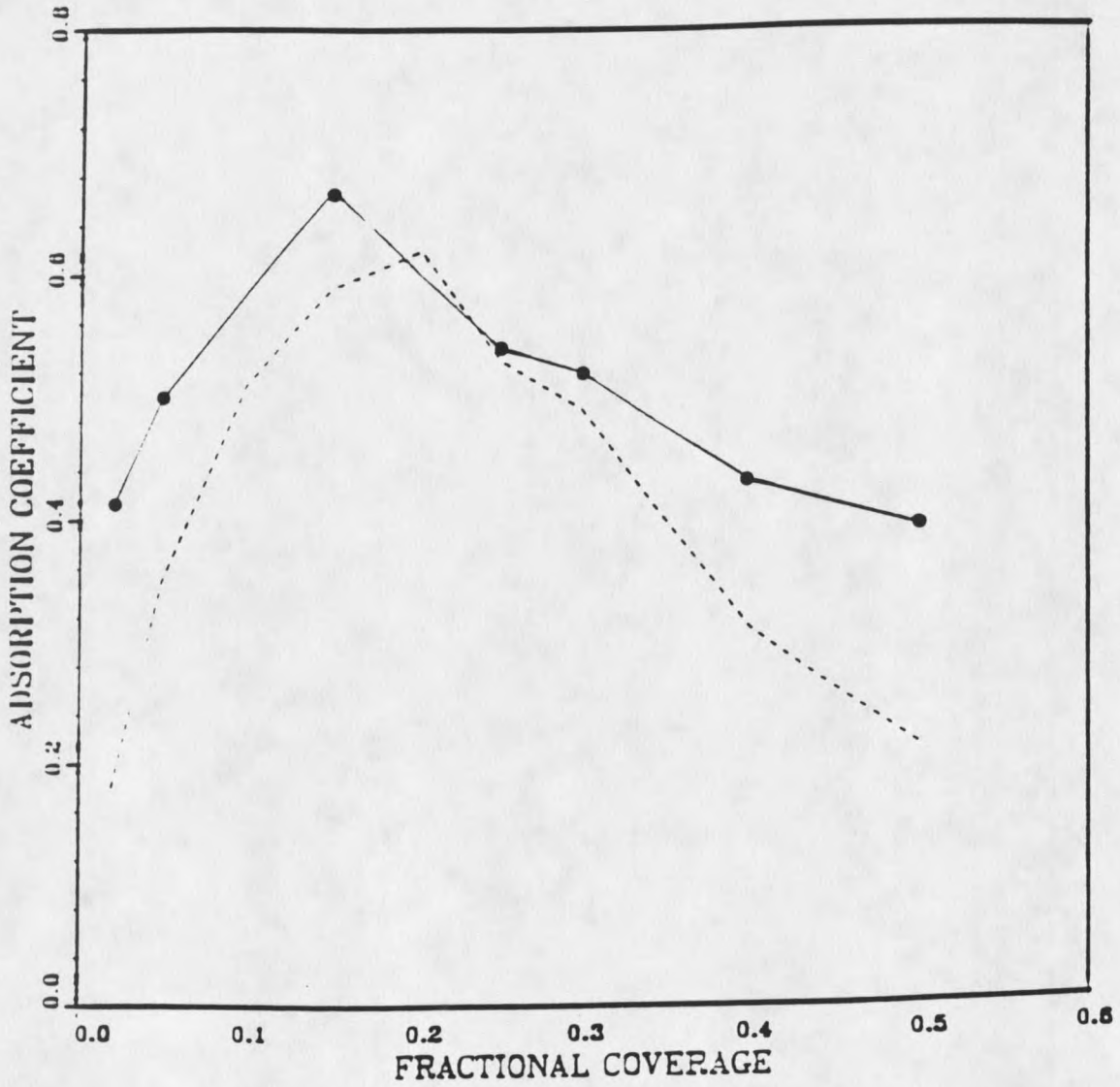

Figure 28. Computer-generated adsorption coefficients as a function of coverage of N_2 on Ru(001). The experimental data is shown along the dotted line.

Results and Discussion

Thermodynamic Properties of the N_2 Adlayer on Ru(001) Surface

When a molecule impinges on the surface to adsorb, it will move toward the most energetically favored site to be found on the lattice. A favored site is one where it interacts favorably with neighboring particles. The van der Waals radius of a nitrogen molecule is larger than the Ru-Ru distance in the (100) surface, so nearest neighbor interactions are unfavorable. However the next-nearest neighbor interaction between adsorbed nitrogen molecules is attractive, and the adsorbed molecules tend to associate into islands with the $\sqrt{3}$ structure, $\theta = 1/3$. This structure is well known from LEED studies of N_2 on Ru(001) surfaces [77(c)], and it provides clear evidence for both the repulsive nature of nearest neighbor (nn) interactions and for attractive next-nearest neighbor (nnn) interactions.

In addition to the $\sqrt{3}$ structure, two other surface phases for N_2 on Ru(001) must be recognized to interpret the experimental data and the calculations reported in this thesis. At low coverages there will be some isolated N_2 admolecules, i. e., a surface-gas state. For low temperatures and a wide range of low surface coverages, the surface will consist of surface gas in equilibrium with island regions of the $\sqrt{3}$ structure as shown in the surface phase diagram [87~89] in Figure 29.

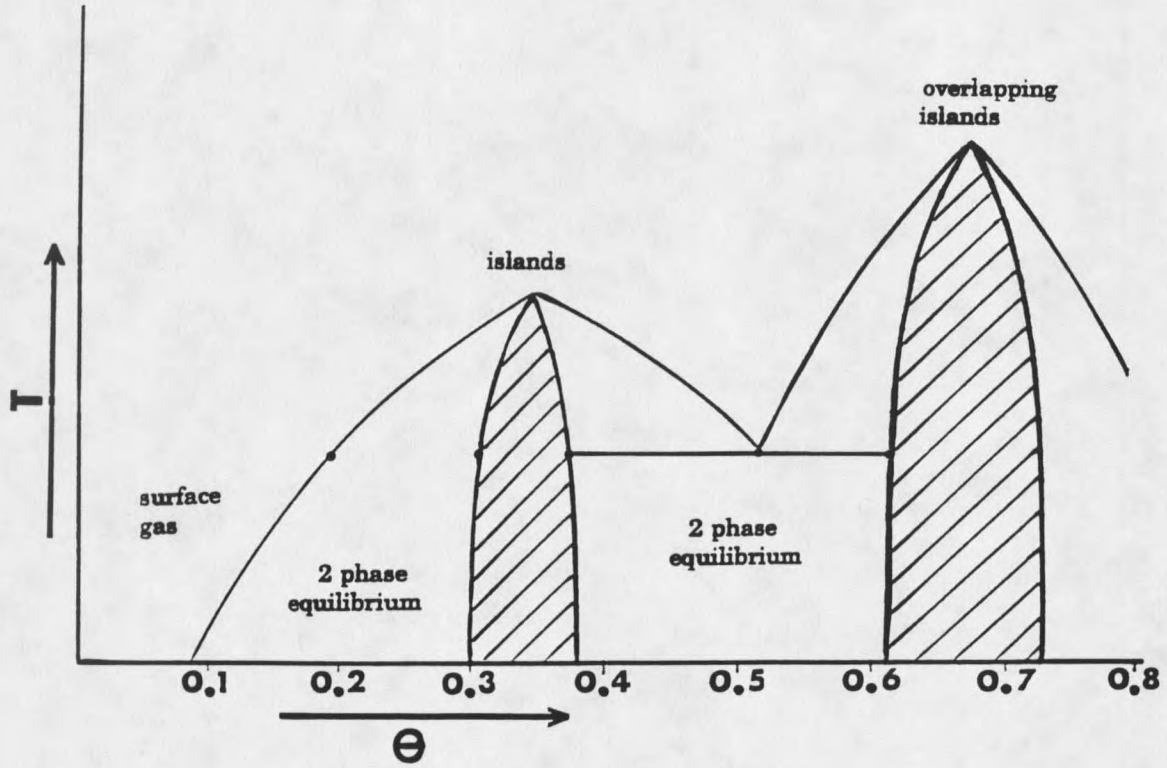

Figure 29. Surface phase diagram of a two-dimensional chemisorbed system of N_2 on Ru(001).

The third phase occurs at higher coverages as the $2\sqrt{3}$ structure and can be described as overlapping islands. The N_2 molecules in this phase or region are less strongly bound since replusive nearest neighbor interactions are present.

A particle adsorbed on the solid surface will desorb if it is supplied with enough energy to break its surface bond and to overcome an activation barrier. The net binding energy of chemisorption can be considered as the binding energy to the surface minus the number of unfavorable interactions of the next nearest neighbor plus the number of favorable

interactions of the next nearest neighbors [69, 71], as implied by eq. 3-(29).

Those three important surface phases (the surface-gas, $\sqrt{3}$ structure and $2\sqrt{3}$ structure) have three different binding energies. For the $\sqrt{3}$ structure, the binding energy is $\varepsilon_g + 3\varepsilon_a$ = 40 kj/mol [77(b)], where ε_g is the binding energy for the surface-gas. We propose that ε_a (which is a measure of the attractive next nearest neighbor interaction) would be 2.5 kj/mol from the information about time-dependent Monte-Carlo calculations for the N_2/Ru(001) system [71]. Then ε_g = 32.5 kj/mol. For the $2\sqrt{3}$ structure, the binding energy is $\varepsilon_g + 3\varepsilon_a - 2\varepsilon_r$ = 24 kj/mol [77(b)]. Here ε_r is a measure of the repulsive nearest-neighbor interaction and ε_r = 8kj/mol. This gives us data on the magnitude of the lateral interaction energy. As the adsorption process continues, different islands are formed and we pass to the different phase equilibria shown in Figure 29.

When the islands begin to overlap, the binding energy will decrease rapidly because of the unfavorable interactions of the nearest neighbors. The single desorption peaks which is shown for low N_2 coverages ($\theta < 0.30$) in Figure 27 is closely related with desorption from the boundaries of isolated islands. The presence of disorder in the low N_2 coverage on Ru is evident from the maps for the chemisorbed adlayer, made by a Monte Carlo method [71]. A large number of small island-domains grow at low coverages ($\theta < 0.33$). The island-domains

are densely populated and tend to merge to form large islands between neighboring domains of similar phase. A few domain boundaries between out-of-phase domains are found at a N_2 sub-monolayer near $\theta \cong 0.33$. For the fractional coverage for $\theta >$ 0.30, another peak appears near 85K in the thermal desorption(TD) studies and this low temperature TD peak is due to repulsive interactions among the N_2 admolecules. Note that our system is ruled by strong repulsive interactions for nearest neighbor sites and weak attractive interactions for next nearest neighbor sites. These features explain the two major desorption peaks found at higher coverages.

From the statistical mechanics model [83], the entropy in the adsorbed layer is given by

$$S_{ad}(\theta) = S_{conf}(\theta) + \sum S_{vib} \qquad \text{eq. 3-(58)}$$

where $S_{conf}(\theta)$ is the configurational entropy caused by the distribution of the molecules on the adsorption sites and Σ S_{vib} is the entropy contribution from the vibrational modes of the adsorbate complex.

The differential molar entropy of the adsorbed layer for n sites occupied is given [84]

$$S_{diff}(\theta) = R\,(\ln n - \ln(n\theta / (1-n\theta))) \qquad \text{eq. 3-(59)}$$

We can define the integral molar entropy, $S_{integ}(\theta)$ as

$$S_{integ}(\theta) = (1/\theta) \int S_{diff}(\theta)\, d(\theta) \qquad \text{eq. 3-(60)}$$

or

$$S_{integ}(\theta) = (1/\theta) \int R\,(\ln n - \ln(n\theta/(1-n\theta)))d(\theta) \qquad \text{eq. 3-(61)}$$

Using integration by parts gives

$$S_{integ}(\theta) = 1/\theta \int R\,(\ln n - \ln(n\theta) - ([1-n\theta] / n)\ln(1-n\theta))\,d(\theta) \qquad \text{eq. 3-(62)}$$

Therefore when a nitrogen occupies two surface sites in the coverage $\theta < 0.6$, $S_{integ}(\theta)$ will be as

$$S_{conf} = R\left[\ln 2 - \ln 2\theta - \left(\frac{(1-2\theta)}{2}\right)\ln(1-2\theta)\right] \qquad \text{eq. 3-(63)}$$

The vibrational entropy ΣS_{vib} is given [73(b), (c)] by

$$S_{vib} = R\left[\frac{h\frac{\nu_i}{kT}}{\exp(h\frac{\nu_i}{kT})-1} - \ln\left(1 - \exp(-h\frac{\nu_i}{kT})\right)\right] \qquad \text{eq. 3-(64)}$$

Eq. 3-(64) can be applied for each vibrational degree of freedom. The two vibrational modes normal to the surface have been determined experimentally for N_2 on Ru(001) at 75K and found to be independent of the coverage: $\nu(Ru - N_2) = 289\ cm^{-1}$ and $\nu(N{\equiv}N) = 2,230\ cm^{-1}$ [74].

For the Langmuir limit, which assumes that the admolecules do not interact with each other, the chemical potential of the adlayer is derived [83(b)] as

$$\mu_{ad}(\theta) = RT \ln(\theta) / [(\theta / (1-\theta)q_s)] \qquad \text{eq. 3-(65)}$$

where q_s is the inner entropy arising from the vibrations of particles on adsorption sites. Assuming that $q_s = \Sigma S_{vib}$, the heat of adsorption as a function of surface coverage can be described as the following equation and is shown in Figure 30.

$$H_{ad}(\theta) = \mu_{ad}(\theta) + S_{ad}(\theta)\, T \qquad \text{eq. 3-(66)}$$

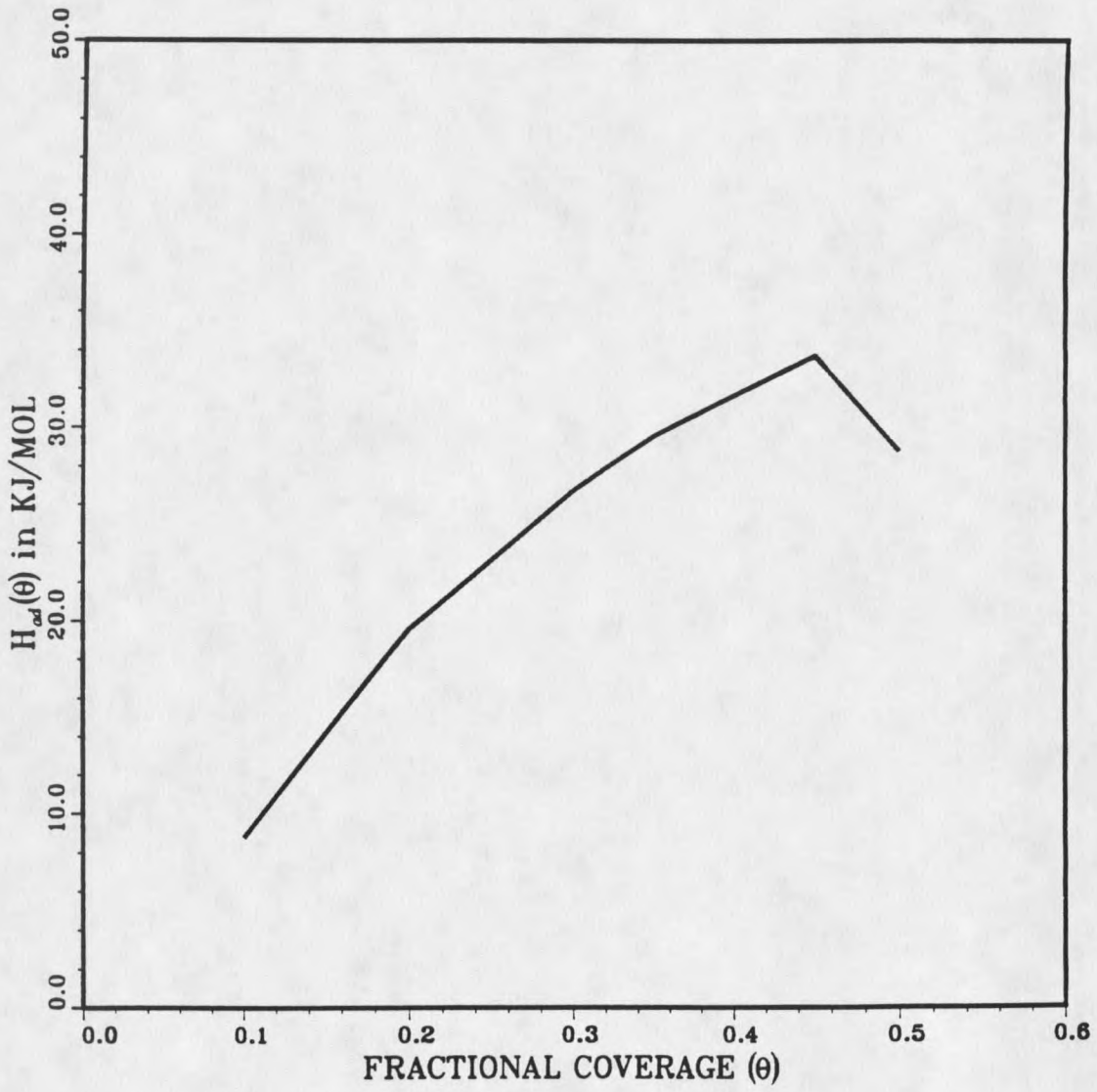

Figure 30. The heat of adsorption as a function of surface coverage.

We propose the total entropy in the adsorbed layer as

$$S_{(ad,tot)}(\theta) = S_{conf}(\theta) + \Sigma\, S_{vib} + S_{lateral}(\theta) \qquad \text{eq. 3-(67)}$$

where $S_{lateral}(\theta)$ is the contribution to the entropy from the lateral interactions. Now we have to consider the entropy due

to lateral interactions in the adsorbed species to modify our over-simplified model toward reality. Including the attractive (nnn) lateral interaction among the admolecules as 3 ε_a for the $\sqrt{3}$ structure and the repulsive (nn) interaction for the $2\sqrt{3}$ structure at $3\varepsilon_a - 2\varepsilon_r$, and representing the two different structures of the N_2 adlayer, we may propose equation for $S_{lateral}(\theta)$ in the two region for the surface coverage parameter:

$$S_{lateral}(\theta) = (3\epsilon_a/T)\ [3\theta/(1 + 3\theta)] \quad for \quad \theta<0.33 \qquad \text{eq. 3-(68)}$$

and

$$S_{lateral}(\theta) = [(3\epsilon_a - 2\epsilon_r)/T]\ ((2/3)\theta / (1 + (2/3)\theta)) \quad for \quad \theta>0.33 \qquad \text{eq. 3-(69)}$$

where T is the surface temperature. The lateral forces which increase their role as the coverages increase lead to a sequence of phase transitions which are reflected in the thermodynamic parameters. The total entropy in the N_2 adlayer as a function of surface coverage is shown in Figure 31. The feature in Figure 31 suggests that the transition state of the N_2 admolecules in the range of 0.2~0.3 coverage is more mobile than the normal one. Note that the influence of "vertical" interactions (by influences of the chemisorption layer on the properties of transient species important in adsorption and desorption) is not included in equations 3-(68) and (69), and is a part of our future work.

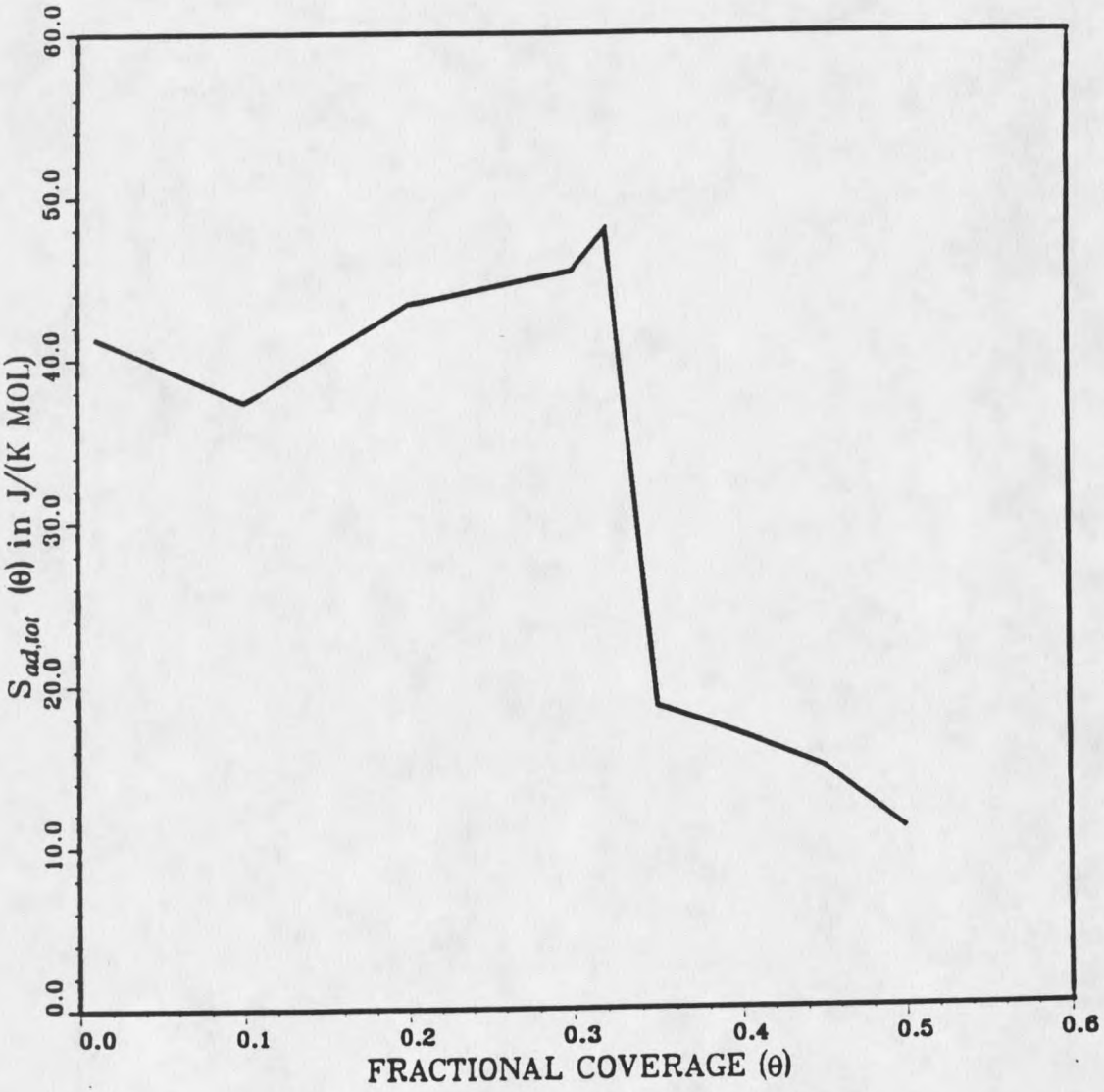

Figure 31. Total entropy in the N_2 adlayer as a function of coverage at 100K.

Interpretation of the Prefactors of the N_2/Ru(001) System

It has been known that eq. 3-(44) can be used to express the rates under equilibrium and non-equilibrium conditions and the prefactor A_d is normally in the range of 10^{13} sec^{-1}. However from the study of the experimental coverage dependence of the pre-exponential [77], larger pre-exponential factors in the range 10^{14} to 10^{16} sec were observed at the low coverages ($\theta < 0.33$) in this system. It is known from the transition state theory that the prefactor is related to the entropy of the system [59(b), 60]. As the particle departs the surface, the vibrational degrees of freedom are converted into translational and rotational degrees of freedom which comprise a continuum. This could be a contributor to the increase in entropy. However we should consider that the major contribution to the prefactor may be the change in the configurational entropy and in the entropy change from the lateral interaction which is best described with the order/disorder term on the surface. The prefactor can be expressed [64, 82] as

$$A_0 = (kT/h)(q^* / q_{ad}) \qquad \text{eq. 3-(70)}$$

By taking the natural logarithm on the both sides of eq. 3-(70), we get

$$\ln A_0 = \ln(kT/h) + \ln q^* - \ln q_{ad} \qquad \text{eq. 3-(71)}$$

where q^* is the partition function for the transition state and $q_{ad}(\theta)$ is the partition function for the adsorbed state.

To calculate ln A_0 we should determine $S_{ad}(\theta)$ and S^*. Thus the application of the result of desorption kinetics leads to a clue for decoding the entropies of adsorbed molecules and the transition state.

From a derivation of the relationship between the thermodynamic state function and the partition function for corrected Boltzons [63, 66(b)], the partition function can be expressed in terms of entropy as

$$S = k\ln(\Omega) = k\ln\left(\prod_i \frac{g^{n_i}}{n_i!}\right) \qquad \text{eq. 3-(72)}$$

where g_i is a number of microcells and n_i, a number of particles. Using Stirling' s approximation, eq. 3-(72) can be rewritten as

$$S = k \sum_i n_i (\ln(q_i/n_i) + 1) \qquad \text{eq. 3-(73)}$$

Using the definition of the partition function, we describe q as

$$q = \sum_i g_i \exp(-\beta\epsilon_i) \qquad \text{eq. 3-(74)}$$

where

$$\beta = (\partial\ln\Omega / \partial U)_{n,v} \qquad \text{eq. 3-(75)}$$

Also, using an equation for the fraction of the particles in the i-th interval, we derive the following equation.

$$n_i/N = (g_i \exp(-\beta\epsilon_i))/q \qquad \text{eq. 3-(76)}$$

We can rearrange eq. 3-(76) as

$$S = k\Sigma_i \left(\ln\left(\frac{q}{n}\right) + \beta\epsilon_i + 1\right) \qquad \text{eq. 3-(77)}$$

Defining $U = \Sigma_i n_i \varepsilon_i$ and $\beta = 1/kT$, we can further rearrange eq. 3-(77) as

$$S = k \ln q^N - k(N \ln N - N) + U/T \qquad \text{eq. 3-(78)}$$

Applying Stirling's approximation ($\ln p! = p\ln p - p$) once again, we get

$$S = Nk\ln\left(\frac{q}{N}\right) + Nk + \frac{U}{T} \qquad \text{eq. 3-(79)}$$

where U will be the average energy existing between the states at a specific temperature T and $N=\sum_i n_i$. Solving for the partition function, we obtain

$$q = N\exp\left(-\frac{\frac{U}{kT} + N + \ln(\Omega)}{N}\right) \qquad \text{eq. 3-(80)}$$

Introducing eq. 3-(80) to eq. 3-(79) and solving for S, we obtain an interim expression for the entropy of the transition state S′ as

$$S' = N\,lu\frac{q^N}{N!} + \frac{U}{T} \qquad \text{eq. 3-(81)}$$

Then, for the entropy of the transition state s^*, we derive

$$S^* = N'lu\frac{q^{N'}}{N!} + \frac{U}{T} \qquad \text{eq. 3-(82)}$$

where $N' = N \exp(-E_{ac}/RT)$ and $S^* = k \ln(\Omega)^*$. Note that the data of E_{ac} as a function of surface coverage were obtained

from the experimental data analysis.

To complete the final expression for a partition function of the transition state, we need to permute all particles over the total lattice sites available as

$$S_{re}^{*} = S^{*}[P(N',M)] \qquad \text{eq. 3-(83)}$$

where S_{θ}^{*} and N' are the functions of the surface coverage and $P(N', M)$ is a permutation function.

To utilize eq. 3-(80), we should determine an expression containing the term, Ω which is to be used for S^{*}. The number of ways that a given number of atoms N, can be distributed among the M sites [85, 86] can be described as

$$\Omega(M,N) = (M - 1 + N)! \,/\, (M - 1)!N! \qquad \text{eq. 3-(84)}$$

The number of times that a nucleation site is occupied by an island containing L adatoms for all $\Omega(M, N)$ configuration is:

$$\Omega'(M,N,L) = M\frac{(M-2+N-L)!}{(M-2)!\ (N-L)!}$$

Thus the frequency of observing an island of size L is:

$$F(L) = M\frac{\Omega'(M,N,L)}{\Omega(M,N)}$$

The most probable island size for given adatoms turns out to be $L = N/M$ for $N \gg M$. Note that a model for island growth should accommodate the formation of new islands with a decreasing frequency as coverage increases.

Here we can choose N as a larger number than M. Using the following equations, $\ln \Omega^{*} = S^{*}/k$ and $\ln \Omega_{ad} = S_{ad}/k$, and

substituting eqs. 3-(79), (80), (81), (82) and (84) into eq. 3-(71), an equation for the entropy change of the N_2 adlayer on the Ru(001) surface is derived as

$$\ln A_0 = \ln\left(\frac{kT}{h}\right) + \frac{(S^* - S_{ad})}{Nk} = \ln\,(kT/h) + 1/R(S^* - S_{ad}) \qquad \text{eq. 3-(85)}$$

where S^* is the entropy of the transition state, S_{ad} is the molar entropy in the adsorbed layer. Note that the term U/T in eq. 3-(82) was canceled out during the calculation. The prefactors as a function of surface coverage at 100K were calculated by using eqs. 3-(79), (80), (82), (83), (84), and (85). The outcome of the computation is featured in Figure 32. The result of our calculation shows a reasonable agreement with the coverage-dependent pre-exponential observed in an experiment [77(b)]. With explicit information about "vertical" interaction and more elaborate surface phase diagram, which will be our near future work, we should have a complete understanding the adlayers as a function of coverage on a substrate. The increase of the pre-exponential in desorption in the range of 0.2~0.3 N_2 surface coverage corresponds to the entropy change in the adlayer. It can be understood in terms of surface phase transitions which correspondto changes in the available surface space for the N_2 admolecule in the layers. The three phases show markedly different coverages with differences in the strong nearest neighbor repulsions and in the important next-nearest neighbor attractions.

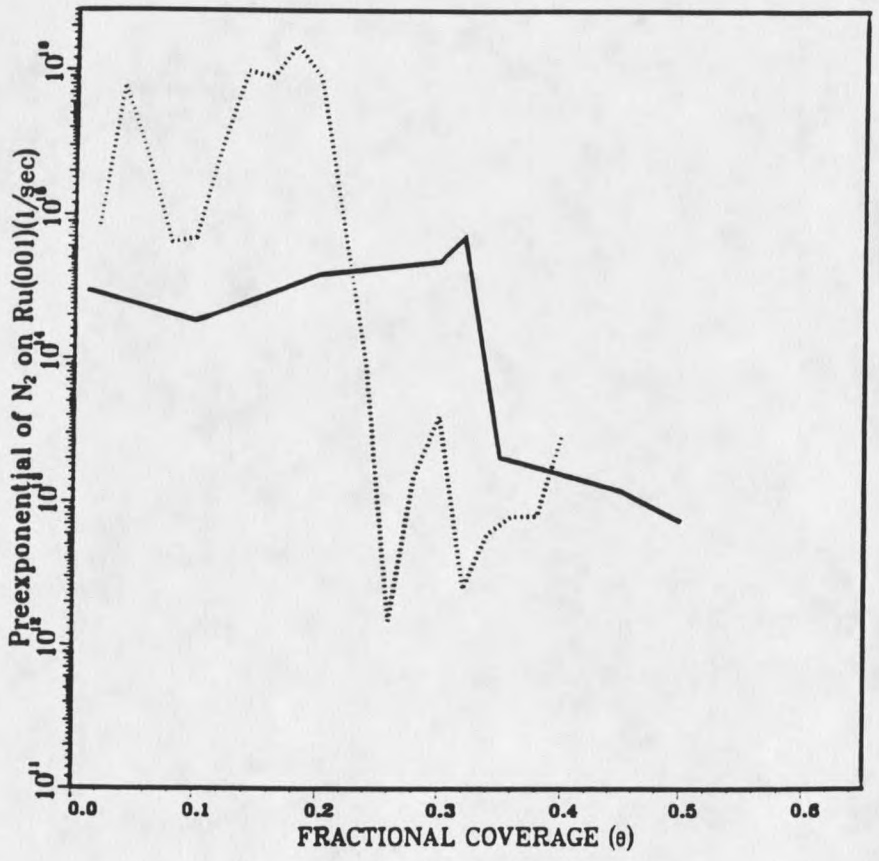

Figure 32. Pre-exponential as a function of N_2 coverage on Ru(001) at 100K. The experimental data is represented as dotted line.

Conclusions

1. Using the precursor-mediated adsorption and desorption kinetic schemes and the microscopic rate parameters such as coverage dependent pre-exponential terms, activation energies and sticking probabilities, we presented a semi-quantitative calculational method to provide the chemisorption and thermal desorption spectrum which is in good agreement with the experimental data.

2. Using the transition state theory and the statistical mechanics models, we developed a calculational method to probe the thermodynamical properties, including the energetics and entropics of an adlayer. This is particularly prepared to explain the larger pre-exponential factor than normal factor experimentally found at low surface coverages.

3. We found that the coverage dependence of the pre-exponential factor in desorption is determined by the properties of the adsorbed phase, including the lateral interactions associated with surface phase transitions in the N_2 adlayer.

REFERENCES

1(a) H.D. Hagstrom, Phys. Rev. 6 336 (1954); ibid, 122 83 (1961); ibid, 123 758 (1961); ibid 150 495 (1966); ibid, 4 4187 (1971).

1(b) H.D. Hagstrom and G.E. Becker, Phys. Rev. B4 4187 (1971).

2. H.D. Hagstrom, Electrons and ion spectroscopy of solids, edited by L. Fiermans, J. Vennik and W. Dekeyser, Plenum, pp 273~323 New York (1977).

3(a) H. Conrad, G. Ertl, J. Kuppers, S.W. Wang, K. Gerard and H. Haberland, Phys. Rev. Lett., 42 1082 (1979).

3(b) F. Bozso, J.T. Yates. Jr., H. Metiu and R.M. Martin, J. Chem. Phys. 78 4256 (1983).

3(c) F.V. Trentini and G. Doyen, Surf. Sci., 162 971 (1985).

3(d) H. Conrad, G. Ertl, J. Kuppers, W. Sesselman and H. Haberland, Surf. Sci., 100 L461 (1980).

3(e) B. Woratschek, W. Sesselman, J. Kuppers, G. Ertl and H. Haberland, Phys. Rev. Lett., 55 611 (1985); ibid, Phys. Rev. Lett., 55 1231 (1985).

4(a) M. Onellion, M.W. Hart, F.B. Dunning and G.K. Walters, Phys. Rev. Lett., 52, 380 (1984).

4(b) T.W. Riddle, M. Onellion, F.B. Dunning and G.K. Walters, Rev. Sci. Instrum., 52 797 (1980).

5. H.D. Hagstrom, Phys. Rev. 96 336 (1984).

6. E. Hood, F. Bozso and H. Metiu, Surf. Sci., 161 491 (1985).

7(a) A. R. West, Solid State Chemistry and its Application, Chap. 16, John Wiley and Sons, New York (1984).

7(b) A. Earnshaw, Introduction to magnetochemistry, Academic Press (1968).

8. S. Ohnishi, C.L. Fu and A.J. Freeman, J. Mag. and Mag. Mat., 50 161 (1985).

9. S. F. Alvarado, M. Campana, F. Ciccacci and N. Hopster, J. Appl. Phys., 53 7920 (1982).

10. F.J. Pinski, J. Staunton, B.L. Gyorffy, D.D. Johnson and G.M. Stocks, Phys. Rev. Lett., 56 2096 (1986).

11. D.W. Gidley, A.R. Koymen and T.W. Capehart, Phys. Rev. Lett., 49 1179 (1982).

12(a) R.J. Celotta, D.T. Pierce, G.C. Wang, S.D. Bader and G.P. Felcher, Phys. Rev. Lett., 43 728 (1979).

12(b) W. Eberhardt and E.W. Plummer, Phys. Rev. B21 3245 (1980).

12(c) D.R. Penn, S.P. Apell, and S.M. Girdin, Phys. Rev. Lett., 55 518 (1984).

13. D. Riegel, K.D. Gross and M. Luszik-Bhadra, Phys. Rev. Lett 59 1244 (1987).

14(a) S. Blugel, M. Weinhart, and P.H. Dederichs, Phys. Rev. Lett., 60 1077 (1988).

14(b) J. Kirschner, K. Koike and H.P. Oepen, Phys. Rev. Lett., 59 2099 (1987).

14(c) H. Akazawa and Y. Muruta, Phys. Rev. Lett., 61 1218 (1988).

15. C.S. Wang and A.J. Freeman, Phys. Rev. B 19 793 (1979).

16. M. Delaunnay, M. Fehringer, R. Geller, D. Hitz, P. Varger and H. Winter, Phys. Rev. B 35 4232 (1987).

17. C.L. Fu, A.J. Freeman and T. Oguchi, Phys. Rev. Lett., 54 2700 (1985).

18. C.S. Wang and J. Callaway, Phys. Rev. B15 298 (1976).

19. C.S. Feigerle, A. Seiler, J.L. Pena, R.J. Celotta and D.T. Pierce, Phys. Rev. Lett., 56 2207 (1985).

20. J.G. Gay and R. Richter, Phys. Rev. Lett., 56 2728 (1981).

21. P. Fulde, Physica 91B 251 (1977).

22. C. S. Wang and A. J. Freeman, J. Mag. and Mag. Mat., 15~18 869 (1980).

23. X. Zhu, J. Hermanson, F.J. Arlinghaus, J.G. Gay, R. Richter and J.R. Smith, Phys. Rev. B 29 4426 (1984).

24. G. Allen, Magnetic properties of low-dimensional systems. Proceedings of an international work shop 2-9 (1986), edited by L.M. Falicov and J.L. Moran-Lopez, Springer-Verlag, Berlin Germany (1986); A.J. Freeman and C.L. Fu, Ibid; R.H. Victora, ibid; K.H. Bennemann, ibid.

25. T.W. Riddle, M. Onellion, F.B. Dunning and G.K. Walters, Rev. Sci. Instrum. 52(6) 797 (1981).

26(a) M. Taborelli, R. Allenspach and M. Landolt, Phys. Rev. B(34) 6112 (1986).

26(b) M. Landolt, R. Allenspach and D. Mauri, J. Appl. Phys. 57 3626 (1985).

27. P. Lorrain and D. Corson, Electromagnetic fields and waves, Chap. 4, W.H. Freeman and Company, S. F. (1070).

28(a) L.I. Schiff, Quantum Chemistry, McGraw-Hill, New York (1968)

28(b) W. Harrison, Electronic Structure and The Properties of Solids, W.H. Freeman and Company, S. F. (1980).

29. C.A. Wert and R.M. Thomson, Physics of solids MaGraw-Hill, New York, (1970).

30(a) M. L. Boas, Mathematical methods in the physical sciences, John Wiley and sons, New York (1983)

30(b) G. Arfken, Mathematical methods for physics, Academic Press, New York (1985).

31. W.A. Goddard, Nature of the chemical bond, Vol. II, Caltech Press, Pasadena, Ca (1980)

32. G. Allan, Surf. Sci. Rep., 1 121 (1981).

33. J. Mathon, Rep. Prog. Phys., 51 1 (1988).

34. D.T. Pierce, R.J. Celotta and J. Unguris, J. Mag. and Mag. Mat., 31-34 869 (1983); T. Shinjo, N. Hosoito and T. Taketa, ibid; 879, ibid; Y. Endoh, H. Ono, N. Hosoito and T. Shinjo, ibid, 881, ibid; U. Gradmann, G. Waller, R. Feder and E. Tamura, ibid, 883, ibid; S. Ohnishi, A.J. Freeman and M. Weinert, ibid, 889, ibid.

35. J.H. Sinfelt, Bimetallic catalysts discoveries, concepts and applications", John Wiley and sons, New York (1983).

36. H. Tochihara, G. Rocker, R.M. Martin, H. Metiu, and J.T. Yates, Jr., preprint.

37(a) K. Christman, G. Ertl and H. Shimizu, J. Catalysis 61 397 (1980).

37(b) H. Shimizu, K. Christmann and G. Ertl, J. Catalysis 61 412 (1980).

37(c) J.C. Vickerman and K. Christmann, Surf. Sci., 120 1 (1982).

38. F. Bozso, J.T. Yates, Jr., J. Aries, H. Metiu and R.M. Martin, J. Chem. Phys., 78 4256 (1983).

39. L. Richter, S.D. Bader and M.B. Brodsky, J. Vacuum Sci. Technol., 18 578 (1981).

40(a) F.J. Himpsel, K. Christman, P. Feibelman and D.E. Eastman, Phy. Rev. B2584 (1981).

40(b) N. Ashcroft and N.D. Mermin, Solid State Physics, Saunders College, Philadelphia, PA (1976).

41. J.E. Houston, C.H.F. Pedan, D.S. Blair and D.W. Goodman, Surface Sci. 154 371 (1985).

42. C. Park, E. Bauerand H. Poppa, Surface Sci. 154 371 (1985).

43. C.I. Hong, E. Hood and R.A. Howald, to be published.

44(a) J.M. Ziman, Principles of the theory of solids, Cambridge Univ. Press, New York (1972).

45. N.F. Mott and H. Jones, Theories of the properties of metals and alloys, Oxford Univ. Press, London (1936).

46(a) J.H. Sinfelt, J.L. Carter and D.J.C. Yates, Jr., Catalysis, 24 283 (1972).

46(b) J.H. Sinfelt, Catal. Rev., 9(1) 147 (1974).

46(c) D.A. Cadenhead and N.J. Wagner, J. Phys. Chem, 72 2775 (1968).

46(d) A.A. Balandin, Advan. Catalysis, 10 96 (1958).

47. A. Roberti, V. Ponec and W.H. Sachtler, J. Catalysis, 28 381 (1973).

48. J.A. Cusumano, G.W. Dennbinski and J.H. Sinfelt, Jr., Catalysis 5 471 (1966).

49. H. Conrad, G. Ertl, J. Kuppers, S.W. Wang, K. Gered and H. Haberland, Phys. Rev. Lett., 42 1082 (1979).

50. F. Bozso, J. Aries, C. Haurahan, R.M. Martin, J.T. Yates, Jr., and H. Metiu, Surface Sci. 136 257 (1984).

51. E. Hood, F. Bozso, and H. Metiu, Surface Sci, 161 491 (1985).

52. Homer Hagstrum, Phys. Rev. 150 495 (1966).

53(a) S.K. Shi, H.I. Lee and J.M. White, Surf. Sci., 102 56 (1981).

53(b) J.T. Yates, Jr., C.H.F. Peden and D.W. Goodman, J. of catalysis, 94 576 (1985).

53(c) C. Park, Surf. Sci., 203 395 (1988).

54. G. Rocker, C.L. Cobb, C.S. Jun, H. Metiu, and R.M. Martin, Surface Sci. 208 205 (1989).

55. P.J. Berlowitz, J.E. Houston, J.M. White and D.W. Goodman, Surface Sci., 205 1 (1988).

56. J.H. Sinfelt and G. H. Via, J. catalysis, 56 1 (1979).

57. J.H. Sinfelt, G.H. Via and F.W. Lytle, J. Chem, Phys., 76 2779 (1982).

58. V.L. Moruzzi, J.F. Janak, and A.R. Williams, Calculated electronic properties of metals, Pergamon Press, New York (1987).

59(a) R. Vanselow, editor, Chemistry and physics of solid surfaces, p73-125, Vol. II, CRC Press (1979).

59(b) K. J. Laidler, Chemical Kinetics, Chaps 3 and 6, McGraw-Hill, New York (1965).

59(c) R.H. Fowler and E.A. Guggenheim, Statistical Thermodynamics, p426, Cambridge University Press, New York (1939).

60(a) K.J. Laidler, S. Glasstone, and H. Eyring, J. Chem. Phys., 8 667 (1940).

60(b) K.J. Laidler, Absolute Rates of Surface Reactions, in P. H. Emmett (editor), Catalysis, chap 5, Reinhold Publishing Corp., New York (1954).

61. G.G. Hammes, Principles of Chemical Kinetics, chap2, Academic Press, New York (1978).

62. H.J. Kreuzer and Z.W. Gortel, Physisorption Kinetics, chap.1, Springer-Verlag, Berlin (1986).

63. P.A. Rock, Chemical Thermodynamics, Chap. 14, University Science Books, Mill Valleg, Ca (1983).

64. S. Glasstone, K.J. Laidler, and H. Eyring, The Theory of Rate Processes, Chap. 7, McGraw-Hill, New York (1941).

65. J. Frenkel, Z. Physik, 26 117 (1924).

66(a) R. Vanselow and R. Howe, Eds, Chemistry and Physics of Solid Surface VI, Chap. 9, Springer-Verlag, Berlin (1986).

66(b) T.L. Hill, Introduction to Statistical Thermodynamics, Addison-Wesley, Reading, Ma (1960).

67(a) R. Gomer, Ed, Interaction on Metal Surfaces in Topics in Applied Physics, Vol. 4, Chap. 4, Springer-Verlag, Berlin (1975).

67(b) R. Vanselow and R. Howe, Eds, Chemistry and Physics of solid Surfaces IV in Chemical Physics 20, Chap. 16, Springer-Verlag, Berlin (1982).

68. G.W. Castellan, Physical Chemistry, Chap. 33, Addison-Wesley, Reading, Ma (1983).

69. M. Grunze and H.J. Kreuzer, Eds, Kinetics of Interface Reactions, Part II, Springer-Verlag, Berlin (1987).

70. C.T. Rettner, L.A. DeLouise and D.J. Auerbach, J. Chem. Phys, 85 1131 (1986).

71. E.S. Hood, B.H. Toby, and W.H. Weinberg, Phys. Rev. Lett., 55 2437 (1985).

72. R. Gorte and L.D. Schmidt, Surf. Sci. 76 559 (1978).

73(a) P. Kisliuk, J. Phys. Chem. Solids 5 78 (1958).

73(b) D.A. King, Surf. Sci. 64 43 (1977).

74. A. Cassuto and D.A. King, Surf. Sci., 102 388 (1981).

75. H. Pfnur and D. Menzel, J. Chem. Phys., 79 2400 (1983).

76(a) P. Redhead, Vacuum, 12 203 (1962).

76(b) D. Adams, Surf. Sci., 42 12 (1974).

77(a) P. Feulner and D. Menzel, Phys. Rev. B25 4295 (1982).

77(b) D. Menzel, H. Pfnur. and P. Feulner, Surf. Sci., 126 374 (1083).

77(c) The references in 66(b).

78. H. Pfnur, P. Feulner, and D. Menzel, J. Chem. Phys., 79 4613 (1983).

79. M. Boudart and G. Djega-Mariadassou, Kinetics of Heterogeneous Catalytic Reactions, Chap. 2, Princeton University Press, Princeton, N. J. (1984).

80. G.W. Barrow, Physical Chemistry, P141, McGraw-Hill, New York (1973).

81(a) H.P. Bonzel and R. Ku, Surf. Sci., 30 299 (1972).

81(b) D.A. King and A.M. Horgan, Surf. Sci 23 259 (1970).

82. H. Pfnur, P. Feulner, H.A. Engelhardt and D. Menzel, Chem. Phys. Letter, 59 481 (1978).

83(a) M. Grunze and P.A. Dowben, Surf. Sci., 141 455 (1984).

83(b) D.A. King and D.P. Woodruff, eds, The chemical physics of solid surfaces and heterogeneous catalysis. Vol. 2, chap. 1, Elsevier, Amsterdam (1983).

84(a) A. Clark, The Theory of adsorption and catalysis, Academic Press, New York (1970).

84(b) R. Vanselow and R. Howe, Eds, Chemistry and Physics of Solid Surfaces VI, Chap. 9, Springer Verlag, Berlin (1986).

85. E.D. Williams, W.H. Weinberg, and A.C. Sobrero, J. Chem. Phys.,76 1150 (1982).

86. E.D. Williams and W.H. Weinberg, Surf. Sci., 109 574 (1981).

87(a) M. Grunze, P.H. Kleben and W.N. Unertl, Phys. Rev. Lett., 51 582 (1983).

87(b) R. Imbihl, R.J. Behm, K. Christmann, G. Ertl and T. Matsushima, Surf. Sci., 117 257 (1982).

88. K.P. Lawley, Ed, Molecule Surface interactions in advances in Chemical Physics, Chap. 3, John Wiley and Sons, New York (1989).

89. D.A. King and D.P. Woodruff, Eds, Adsorption at Solid Surfaces Vol. 2, in the Chemical Physics of Solid Surfaces and Heterogeneous Catalysis, Elsevier, Amsterdam (1983).